ICE VELOCITY AND MASS BALANCE STUDY OF THE SKELTON GLACIER, ANTARCTICA, USING REMOTE SENSING AND GIS TECHNIQUES

A thesis submitted in partial fulfilment of the requirements for the Degree

of Masters in Geographic Information Science (MGIS)

in the University of Canterbury

by Nick R. McLay

University of Canterbury

2013

Abstract

The Skelton Glacier is one of the many smaller outlet glaciers located in the Transantarctic Mountains, where it drains ice into the Ross Ice Shelf. These outlet glaciers are important when determining the past, present, and future state of the mass balance of the East Antarctic Ice Sheet. This research uses satellite imagery acquired over a period of 15 years to obtain a high resolution velocity field for the Skelton Glacier which is then used to calculate the mass flux and mass balance at ten flux gates along the glacier using the input-output method. The high resolution velocity field is combined with ice thickness data and accumulation data from other sources to obtain the total mass balance.

The high resolution velocity field of the Skelton Glacier was created using European Remote-Sensing Satellite 1 and 2 (ERS-1/2) Synthetic Aperture Radar (SAR) data acquired in 1996 with the processing technique of SAR interferometry (InSAR). Because of the lack of differential InSAR pairs, new auxiliary data from the ICESat and TanDEM-X mission were included into the analysis. A velocity field was created at a spatial resolution of 50m which was validated with *in situ* GPS measurements from 2011/12, and compared to lower resolution velocity fields of the Skelton Glacier. The ice velocity field is at improved accuracy for this area compared to previous studies and is thought to be representative for the mean ice velocity. The analysis of ice flux at several flux gates allowed an improved error estimation of the applied technique to estimate the overall mass balance.

Mass flux estimates along the glacier were calculated using the new velocity field and additional thickness data, which was then compared to two accumulation datasets to give mass balance estimates along the glacier at selected flux gates. The mass flux through the grounding line was found to be 1.2165 Gt a^{-1}, which needs to be balanced in a state of mass balance equilibrium by a mean annual snow accumulation of about 185 mm a^{-1} water equivalent over the total catchment area determined with 6569 km^2. The mass balance at the grounding line is slightly negative, but the second flux gate is thought to be more representative of the mass balance, which is estimated to be 0.0441 Gt a^{-1}. Error analysis of the mass balance estimates found uncertainties in this data to be approximately 0.110 Gt a^{-1}. It is concluded from the analysis that further improvements in the overall mass balance estimate can be primarily obtained by a better knowledge of ice thickness and snow accumulation.

Contents

List of Figures

List of Tables

List of Equations

List of Acronyms

ADD ..... Antarctic Digital Database

ALOS ..... Advanced Land Observing Satellite

AMSR-E ..... Advanced Microwave Scanning Radiometer – Earth observing system

ASAID ..... Antarctic Surface Accumulation and Ice Discharge

CReSIS ..... Center for Remote Sensing of Ice Sheets

DEM ..... Digital Elevation Model

DLR ..... Deutsches Zentrum fuer Luft und Raumfahrt

DIFF&GEO ..... Differential SAR Processor & Geocoding

DInSAR ..... Differential Interferometric Synthetic Aperture Radar

DISP ..... Display Tools

EAIS ..... East Antarctic Ice Sheet

EEC ..... Enhanced Ellipsoid Corrected

ENVI ..... Environment for Visualising Images

ERS ..... European Remote-Sensing Satellite

ESA ..... European Space Agency

GAC ..... German Aerospace Center

GCP ..... Ground Control Point

GIPSY ..... GNSS-Inferred Positioning System

GPS ..... Global Positioning System

ICESat ..... Ice Cloud and Land Elevation Satellite

IDL ..... Interactive Data Language

IMAU ..... Institute for Marine and Atmospheric research Utrecht

InSAR ..... Interferometric Synthetic Aperture Radar

IPCC..... Intergovernmental Panel on Climate Change

ISP..... Interferometric SAR Processor

JERS-1 ..... Japanese Earth Resources Satellite 1

MEaSUREs..... Making Earth System Data Records for Use in Research Environments

NASA..... National Aeronautics and Space Administration

NSIDC ..... National Snow and Ice Data Center

PS..... Polar Stereographic

RAMPv2 ..... Radarsat Antarctic Mapping Project Version 2

SAR..... Synthetic Aperture Radar

SLC ..... Single Look Complex

TAM..... TransAntarctic Mountains

TanDEM-X ..... TerraSAR-X add-on for Digital Elevation Measurements – X-band

UPS ..... Universal Polar Stereographic

UTM..... Universal Transverse Mercator

WAIS ..... West Antarctica Ice Sheet

1 - Introduction

Antarctica is a vast continent precious to all the earth, but it is coming under threat from increased atmospheric and oceanic temperatures as a result of global warming. Recent estimates from the IPCC 2007 report estimate the 100-year linear trend of atmospheric warming to be 0.74°C (1906-2005). The same report has also predicted the extent of future global warming based on numerous models, and has warned that by 2100 the earth could warm up by another 1.1 to 6.4°C (IPCC, 2007). While the oceans react to this warming slower than the atmosphere, it has been found that the upper level of ocean (top 700m) has increased by 0.1°C from 1961 to 2003 (IPCC, 2007). This warming from the atmosphere above and the ocean below has begun to impact on the major ice sheets in Greenland and Antarctica. The Greenland Ice Sheet and West Antarctica Ice Sheet have both been estimated to have large negative mass balances, with -267 ± 38 Gt a^{-1} (Rignot *et al.*, 2008) and -48 ± 14 Gt a^{-1} (Rignot & Thomas, 2002) respectively. The East Antarctic Ice Sheet is estimated to have a small positive mass balance of 22 ± 23 Gt a^{-1} (Rignot & Thomas, 2002), but with large uncertainties. These three ice sheets hold 3.3×10^7 km^3 of ice which is susceptible to a changing climate. This volume of ice holds the potential to raise sea level by 70m if it all melted, which would put millions of humans at risk of flooding (Rignot & Thomas, 2002). The present rate of sea level rise is estimated to be 1.7 ± 0.5 mm a^{-1} from 1961 to 2003 (IPCC, 2007). With a risk like this, it is very important to know exactly what state these ice sheets are in, and how they might be changing as a response to this global warming.

The EAIS is the largest ice sheet with an estimated ice volume of 2.6×10^7 km^3 (Bart & Anderson, 2000), and holds the most potential for sea level rise, yet it is the ice sheet which has the most uncertainties relating to mass balance estimates. To determine more accurately whether the EAIS is losing or gaining ice, studies of the outlet glaciers and ice streams are important. These glaciers are the passages where ice from the ice sheet flows down into the ocean, and it is analysis of their flow which determines whether more ice is being accumulated on the ice sheet or whether more ice is flowing into the oceans. Even though global temperature is increasing, it is still at a low enough temperature on the EAIS that surface melting will not occur. It is the warming ocean that has the potential to increase the ice discharge from the ice sheets (Holland *et al.*, 2008; Jacobs *et al.*, 2011). The theory is that as the ocean warms up, ocean currents below the ice shelves surrounding Antarctica increase the basal melting of ice shelves. As the mass of the ice shelves decreases, the buttressing effect on the outlet glaciers flowing into the ice shelves decreases too (Rignot *et al.*, 2008). This potentially could result in the acceleration of the glacier with more ice draining out of the ice sheet as a result. Acceleration due to the loss of buttressing ice has been noted numerous times,

but none more so than the Larsen Ice Shelf on the Antarctica Peninsula (De Angelis & Skvarca, 2003; Rack & Rott, 2004). Knowing the state of these outlet glaciers and determining how they change over time then becomes important with the testing of this theory and to see how the ice sheets change in response to a warming climate. As technologies grow and remote sensing techniques become more accurate and easier to implement, analysis of these outlet glaciers become easier and the state of the EAIS becomes clearer.

1.1 – Research Goals

This research aims to take a detailed look at Skelton Glacier; one of the outlet glaciers in the Transantarctic Mountains (TAM) which drains ice from the East Antarctic Ice Sheet. Little research has been done previously on this glacier, especially near the grounding line, so this research builds on the existing knowledge using new satellite remote sensing techniques. The objectives for this research are:

i) Create a high resolution 3D velocity field of the Skelton Glacier from the ERS-1/2 InSAR data from the 1990s and newer auxiliary data sets

ii) Determine the ice discharge through several flux gates along the glacier using ice velocity and ice thickness data

iii) Estimate the overall mass balance and associated errors for the Skelton Glacier using the budget method

Results from this study will support research on outlet glaciers in Antarctica, and will help with the current interpretation of the mass balance of TAM outlet glaciers and consequently of the East Antarctic Ice Sheet.

1.2 – Synthetic Aperture Radar Interferometry

Advanced remote sensing techniques for determining glacier motion have only come about in the past few decades, but have greatly increased the abilities to observe these processes happening on the earth. The first instance of Synthetic Aperture Radar Interferometry (InSAR) being used to measure movement was by Goldstein and Zebker (1987), where surface water currents of San Francisco Bay were measured from an aircraft. By 1991, the European Space Agency (ESA) included a Synthetic Aperture Radar (SAR) on their ERS-1 satellite mission, allowing large amounts of data to be gathered over a large area of the globe, and allowing InSAR to start being used for many more applications. This was then enhanced further when the ESA launched the ERS-2 satellite, which was planned to fly

the same orbit as the ERS-1 satellite but one day later, allowing a tandem mission with the two satellites. Since the ERS-1/2 mission, many more satellites have been launched with SARs on board, including JERS-1 (1992), RADARSAT-1 (1995), Envisat (2002), and ALOS (2006). With the ability to remotely collect data, it became apparent that this technology could be used for analysing many different earth processes, including the monitoring of surface deformation of volcanoes and earthquakes, and ice flow (Kwok & Fahnestock, 1996; Massonnet *et al.*, 1995; Wright, 2002). Goldstein *et al.* (1993) was the first to use this InSAR technology to monitor ice sheet motion, focussing on the Rutford Ice Stream in Antarctica. This was compared with ground data and was found to match relatively well, which helped prove how valuable the new technique of interferometry would become for ice velocity studies. Since then, this technique has become one of the main techniques for acquiring ice velocity, and as the SAR instruments and auxiliary data used for processing improves, so will the accuracy of the velocity fields that are produced.

1.3 – Glaciological Characteristics of TAM outlet glaciers

The TAM are located on the eastern side of the EAIS and stretch from coastal Antarctica near Cape Adare to the inner regions near the South Pole. Within these mountains are numerous outlet glaciers, which drain ice from the EAIS into the ocean or ice shelves. These are important locations to study as they drain a large amount of the ice from the EAIS and changes in this region can be significant. North of McMurdo Sound the outlet glaciers flow directly into the Ross Sea, while south of McMurdo Sound they flow into the Ross Ice Shelf. The outlet glaciers located within the TAM can be categorised by the size of the basin and the velocity of the ice flowing through the glacier. Some of the large glaciers have fast ice velocities and large catchment basins (e.g. Byrd Glacier), while others have lower velocities and small basins (e.g. Skelton Glacier).

Most slow outlet glaciers are thought to be “cold” glaciers, where the basal temperature of the base of the glacier is below zero. This means the ice is frozen to the underlying rock and sliding does not occur (Riger-Kusk, 2011). These glaciers flow primarily by ice deformation internally, which leads to slower velocities. The fast outlet glaciers have been found to be both “cold” and “warm” in terms of the basal temperature. Warm glaciers have basal melting and have a component of sliding to the glacier flow. Small pockets of cold glaciers can have basal conditions of warm glaciers, but these are usually minor and not indicative of the glacier as a whole.

Ice loss from the glaciers in the TAM is different depending on the location. The main ice loss of the glaciers north of McMurdo Sound is calving at the front of the glacier as it flows into the Ross Sea. Further south calving does not occur due to the Ross Ice Shelf connecting to the ends of all these glaciers. Here ice lost due to ablation is also much lower. Instead, ice is mostly lost from flowing

directly into the ice shelf, although there is also some ice lost to sublimation in katabatic wind regions. Katabatic winds are thought to be experienced in most areas of the TAM, with areas around the Byrd, Mulock and Skelton Glaciers having satellite proof of the katabatic winds existence (Breckenridge *et al.*, 1993). Basal melting of the floating part of these glaciers also occurs downstream of the grounding line, though for the Ross Ice Shelf it is usually low due to the large oceanic currents not usually extending this far into shallower waters.

1.3.1 – Mass Balance

To determine whether ice is being lost or gained, the mass balance of the outlet glaciers need to be found. The mass balance is expressed in a negative or positive number, which explains whether the mass of ice is increasing or decreasing (negative is decreasing and positive is increasing). The magnitude of the number is the mass of ice that is either being lost or gained. There are three satellite methods for estimating the mass balance (Shepherd *et al.*, 2012):

- Geodetic Method
- Elevation Change Method
- Input-Output Method (Budget Method)

The Geodetic Method looks at the temporal changes in gravity measurements of the glacier or ice sheet which change as the mass of the glacier or ice sheet changes. Increased gravity measurements implies that the mass of ice has increased, while decreased gravity measurements imply that the mass of ice has decreased (Sasgen *et al.*, 2012). The surface elevation change method looks at the progressive change in elevation of an ice sheet or glacier over time. If the surface elevation is decreasing, then it is assumed that ice is being lost, while if the surface elevation is increasing, it is assumed that ice is being gained. Isostatic rebound can affect this method (Helsen *et al.*, 2008). Finally the Input-Output Method compares ice flowing into the system with the ice leaving this system, with the difference being the mass balance. Accumulation data is used as the input, while mass flux estimates are used as the output. If the difference is negative, this implies that more ice is leaving the system, but if the difference is positive, this implies more ice is being gained in the system (Shepherd *et al.*, 2012). Each of these uses different satellite remote sensing platforms and techniques to estimate whether there is ice loss or gain.

1.3.2 – Grounding line

The point at which the outlet glacier starts to float is known as the grounding zone. This is a transition zone between the grounded ice of the outlet glaciers or ice sheet, and the floating ice of the ice shelf. Figure 1.1 shows a simple diagram of the grounding zone, where G is the grounding line which is the point where the ice decouples and starts to float and the area between F and H is the grounding zone.

This zone is the area of ice which is influenced by the grounding line and is an ice flexure zone. Point H is where the ice is in hydrostatic equilibrium and is completely influenced by the ocean and tides. This transition zone (F to H) is the extent at which the longitudinal stresses of the ice shelf affect the ice stream, which is related to the tidal movement.

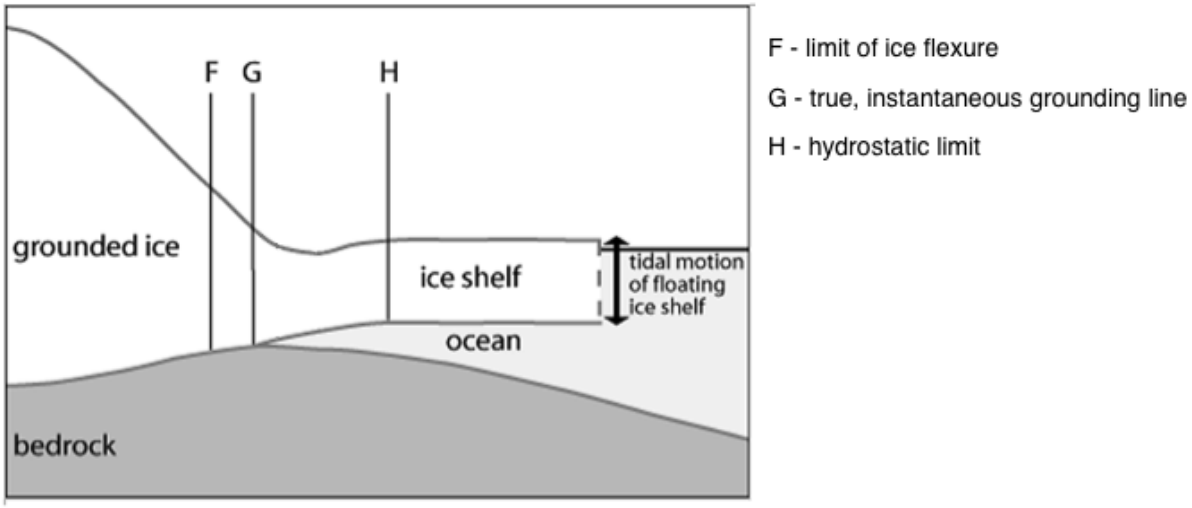

Figure 1.1: Diagram of the Grounding Zone (Modified after Brunt *et al.*, 2010)

The grounded ice above the grounding line is influenced by the valley walls where shear stresses are resisting the ice movement, then as the ice starts to float the mechanisms change to longitudinal stretching and lateral shearing (Schoof, 2007). Downstream of the grounding line, the ocean water circulating under the ice causes basal melting and can significantly decrease the mass of the ice stream. Due to this occurrence, ice flux data for mass balance studies are usually taken at the grounding line. The grounding line position is a good indicator of global warming, as the location can change in response to the sea level rising and glacier acceleration. Un-grounding of ice at the grounding line is known to affect the glaciers force balance, longitudinal stretching and flow speed (Rignot, 2006).

1.4 – Skelton Glacier

The Skelton glacier (78° 41′ 36.6″ S, 161° 38′ 32.64″ E) is located in the middle of the TAM to the south of McMurdo Sound. Directly to the south of the Skelton Glacier is the Mulock Glacier which both drain into the Ross Ice Shelf (Figure 1.2). The Skelton Glacier is classified as a slow moving glacier with low ice velocities. It is characterised by the two grounded glacier branches over the upper half of the glacier, which combine near the grounding line. The lower half of the glacier is floating ice through the small fjord (approximately 10km wide). On the Southern Branch, the grounding line has

been located just above the combining of the two branches, but on the Northern Branch, the grounding line is still unknown.

Detailed glaciological studies of the Skelton are limited with many important characteristics still unknown. The glaciological characteristics of other slow moving glaciers in the TAM have been studied more in-depth, and can be assumed to be reasonable estimates for what the Skelton Glacier would be like. The main characteristics that are unknown are the basal conditions, bedrock topography and how the glacier flows. These would need ice core sampling and airborne surveying to acquire this data. The nearby Ferrar Glacier has had detailed research into these characteristics which might have similarities to the Skelton Glacier. It is estimated that the Ferrar Glacier is a "cold glacier," which means the basal temperature is below zero and the glacier bed is frozen to the underlying topography (i.e. no flow). The ice then mostly flows by internal deformation within the ice stream (Golledge & Levy, 2011). Although conditions are not identical between the Ferrar Glacier and the Skelton Glacier, these characteristics could be similar. More detailed studies of the smaller outlet glaciers need to be done to determine accurate basal and flow conditions.

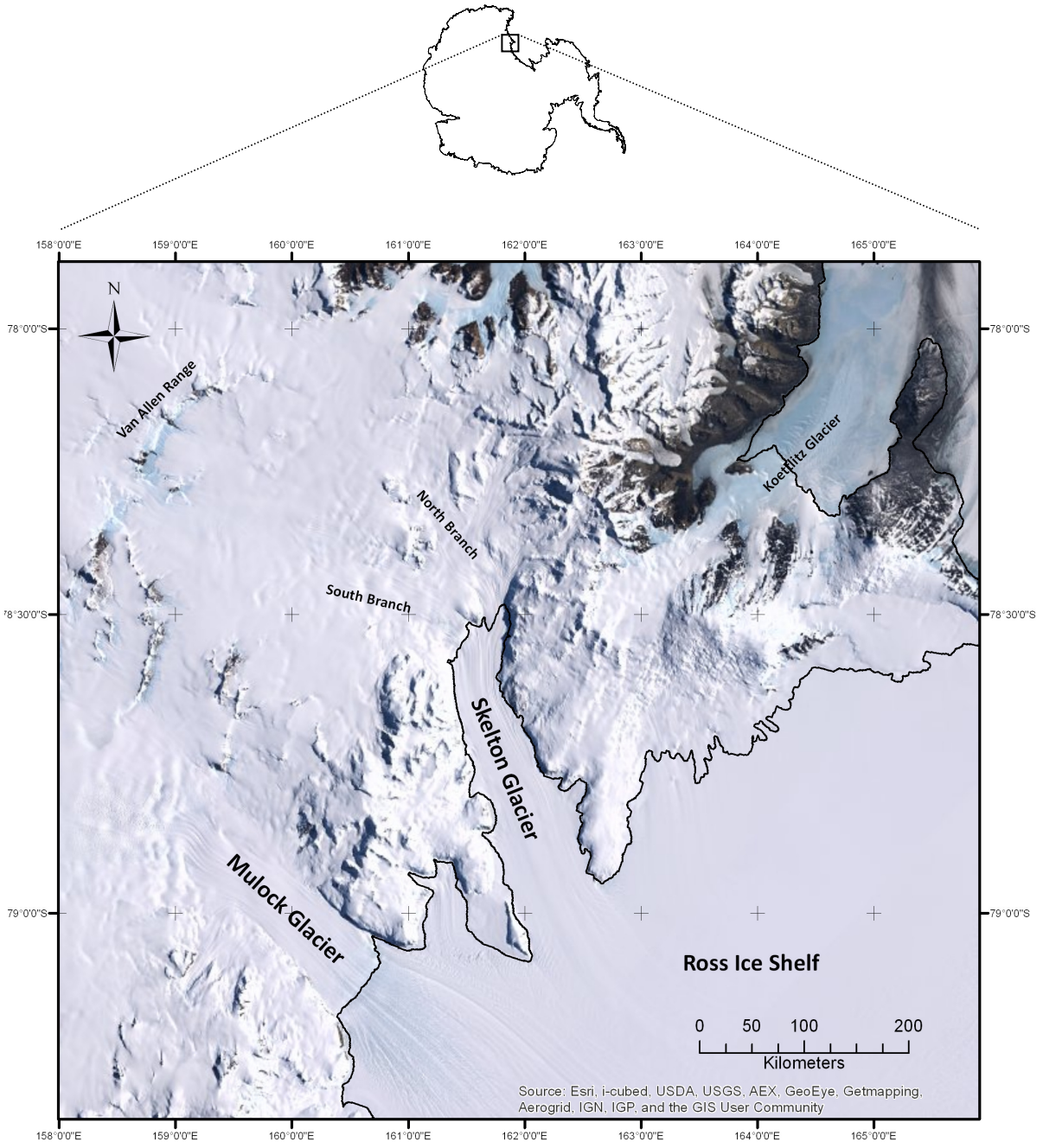

Figure 1.2: Map of the Skelton Glacier showing the North and South Branches, and location within Antarctica. Background imagery acquired from ArcMAP basemap tool.

1.5 – Methods and Approach

This thesis aims to follow Interferometric processing techniques using ERS SAR imagery to achieve an ice velocity field for the Skelton Glacier and determine the mass balance information near the grounding line. The main features of this thesis are separated into separate chapters, including the introduction and background of the research project, the data that is used, the theories behind the processing technique, the methodology of creating an ice velocity field with results, the methodology of mass flux calculations with results and then discussion of the results. The structure of the thesis is as follows:

Chapter 1: Introduction addressing the current situation of the EAIS, and how this thesis aims to contribute to this research. Information about the study area and local setting is also introduced.

Chapter 2: The data used for this thesis is examined in this chapter; including satellite data, digital elevation models, accumulation data and GPS ground measurements.

Chapter 3: The theory behind radar systems and SAR Interferometry are described in this chapter using relevant information that will be required for understanding the method of this research project.

Chapter 4: The methodology of the thesis is outlined in this chapter, which follows processing chain from the starting SLC SAR images to the final displacement maps. The validation of the velocity field and the results are also included.

Chapter 5: The theory and methodology of obtaining the mass flux and mass balance for the Skelton Glacier along with the results are shown in this chapter.

Chapter 6: The implication of the results and how well they fit into the wider context is addressed in this chapter. Error analysis is then looked at so that uncertainties can be estimated for the data that is used.

Chapter 7: This chapter concludes the research and addresses where future research is important for the Skelton Glacier and other Transantarctic Mountain outlet glaciers.

2 – Data

A variety of data from different sources have been used in this research. The main data are radar images for the interferometric processing acquired by the ERS-1 and -2 satellites during the European Space Agency's (ESA) 'tandem mission' in 1996. These data will be processed to extract precise surface velocities of the Skelton Glacier at high spatial resolution as a basis to estimate the ice flux through flux gates. Although the ERS satellite data were acquired more than 15 years ago, new auxiliary data sets are now available enabling improved analysis of the surface velocity field. Precise surface elevation data originate from NASA's ICESat (Ice, Cloud, and Elevation) satellite acquired between 2003 and 2009. The Antarctic-wide Radarsat Antarctic Mapping Project Version 2 (RAMPv2) Digital Elevation Model (DEM) created in 2001 also provides elevation data for the study area. New data products are available from the German Aerospace Agency's (DLR – Deutsches Zentrum fuer Luft und Raumfahrt) TerraSAR-X satellite, launched in 2007 which was later followed by a twin satellite launched in 2010. This second satellite is flown in formation with the first satellite at only a few hundred metres apart forming the TanDEM-X configuration, allowing the simultaneous collection of elevation data from two different viewing angles. The resulting DEM can be processed to a horizontal resolution of 12m and a vertical resolution of 2m (Bartusch *et al.*, 2010). From the same satellite mission, speckle tracking data was acquired which was used for calculating accurate flow vectors used in the interferometric processing and image visualisation. The interferometric processing is complimented by field data including in situ GPS data for ground truthing and airborne radar data for ice thickness estimates acquired in 2011/12. The satellite data used for this research have been received as part of larger research projects. Detailed information relating to the SAR data acquisition, imaging geometry, and the interferometric processing techniques will be explained in Chapter 3. Here an overview of all used data sets is provided.

2.1 – Satellite Remote Sensing Data

A range of satellite data was used, from Synthetic Aperture Radar data from the ESA, Speckle Tracking data from the German Aerospace Agency, and ICESat data from the National Aeronautics and Space Administration (NASA).

2.1.1 – SAR Satellite Data

Synthetic Aperture Radar (SAR) satellite imagery from the European Space Agency (ESA) was used for the interferogram generation. The ESA launched the European Remote-Sensing satellite (ERS), their first earth-observing satellite, in 1991 which carried a payload of multiple earth-observing instruments including a Synthetic Aperture Radar. By 1995, a second ERS satellite, with a near

identical payload, was launched which would fly in tandem with the first satellite (van 't Klooster, 2011). The ERS-1 satellite has a 35 day repeat pass individually, so the ERS-2 satellite was flown in an identical orbit one day behind. Reducing this time interval between image acquisitions improves the coherence of the radar image, though decorrelation between the images will still exist (see Chapter 3.5). These were the first European satellites to acquire SAR data, which had a near-global coverage. The right-looking radar sensor away from the southpole has an angle of incidence of 23° at the scene centre which limits the latitude at which the satellite can acquire data to approximately 79.5°S. Additionally, the limited onboard data storage in the 1990s using tape recorders required regular direct data downloads to earth to allow for further data acquisition. The Skelton Glacier falls within the southern limit of the ERS-1 and -2 data coverage, although the amount of data acquired by the satellites that have been processed, checked and made available for download is minimal. Table 2.1 shows the available ERS-1/2 pairs that were acquired for the study area (note that only two pairs are ascending), and Figure 2.1 shows the location of these image pairs on the Skelton Glacier. The sets of ERS-1/2 images with a small baseline and minimal offset were suitable to be used for interferometry processing. The inaccuracy of the satellite orbits at the time that the ERS satellites data was acquired means that baseline refinement is required using new high resolution auxiliary elevation data. For the combination of the ascending and descending pairs, the ones with the highest angular difference in the radar look direction were the most suitable.

Table 2.1: ERS-1/2 Satellite data pairs acquired in the Skelton Glacier area during the ERS Tandem Mission in 1996.

Frame Number	Sensor	Acquisition Date	Orbit	Satellite Track	Ascending/ Descending	Perpendicular Baseline (m)
1	ERS-1	23-Feb-96	24105	69	Descending	167
	ERS-2	24-Feb-96	4432			
2	ERS-1	28-Feb-96	24177	141	Descending	149
	ERS-2	29-Feb-96	4504			
3	ERS-1	26-Jan-96	24177	170	Descending	136
	ERS-2	27-Jan-96	4504			
4	ERS-1	31-Jan-96	23776	241	Descending	154
	ERS-2	1-Feb-96	4103			
5	ERS-1	8-Feb-96	23890	355	Ascending	184
	ERS-2	9-Feb-96	4217			
6	ERS-1	21-Mar-96	24491	455	Ascending	31
	ERS-2	22-Mar-96	4818			
7	ERS-1	21-Mar-96	24492	456	Descending	57
	ERS-2	22-Mar-96	4819			

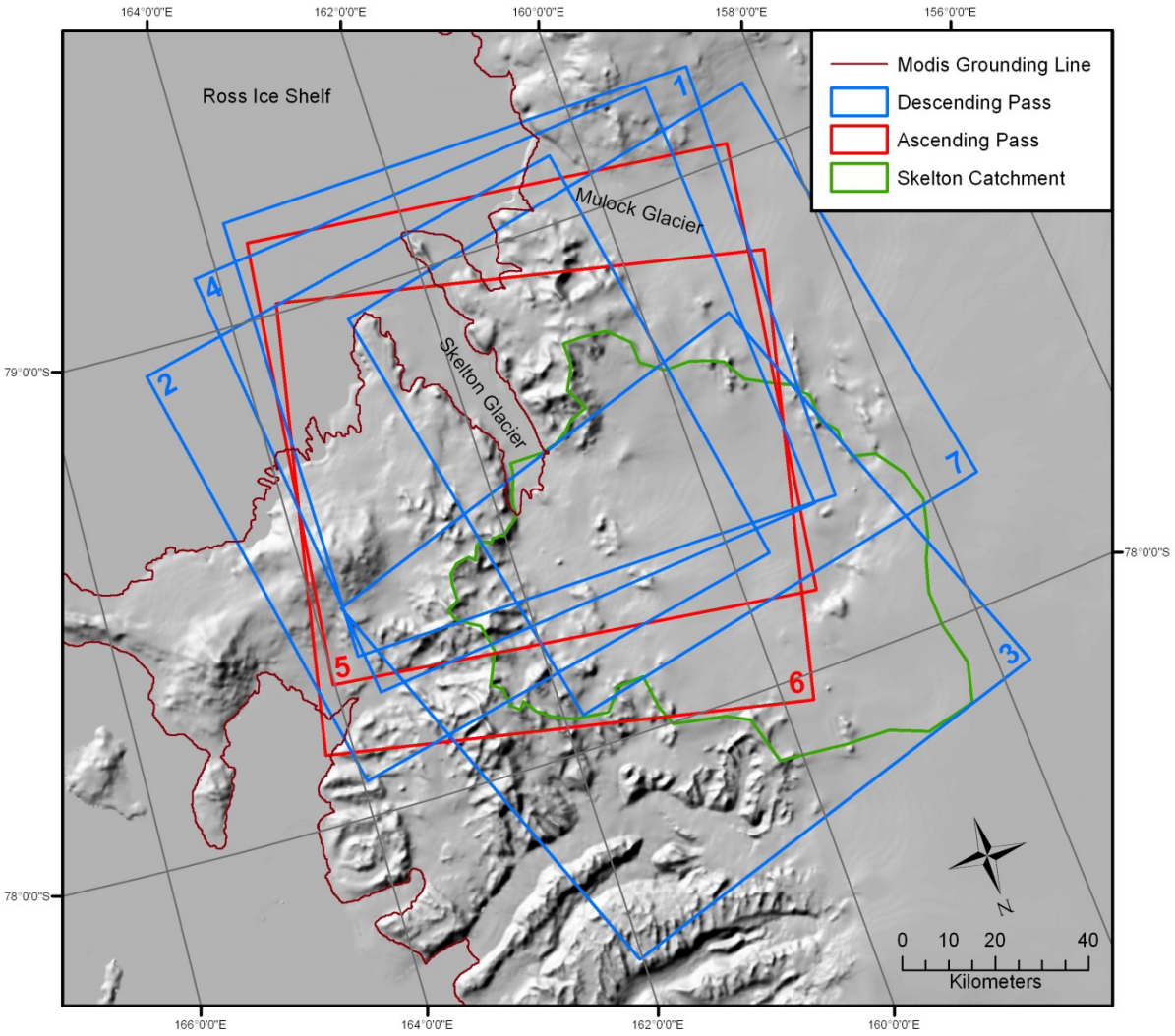

Figure 2.1: Map of the Skelton Glacier area showing the satellite frames that were acquired. Two red frames represent the ascending frames, while the blue frames represent the descending passes. The estimated Skelton Catchment area is shown by the green polygon, and the Modis grounding line is shown by the dark red line. The background is a hillshade image of the RAMPv2 DEM and it is in polar stereographic projection.

2.1.2 – Speckle Tracking Data

Speckle tracking from the TerraSAR-X repeat pass satellite data was also used to determine the glacier flow direction and be used as an alternative ice velocity field for which the InSAR velocity field can be compared. The TerraSAR-X speckle tracking data was acquired in the 'danaf_HYD1421' project in mid-2012 (Table 2.2). Data from the satellite was acquired in the StripMap imaging mode which gives a 3m resolution and a scene size of 30km by 50km. The format that was acquired was Enhanced Ellipsoid Corrected (EEC), which means the distortions in the data are corrected with a DEM, and then projected in either UTM or UPS projection (Roth *et al.*, 2004). The repeat pass for the

satellite is 11 days. The TerraSAR-X data that was acquired covers the Skelton Glacier grounding line, the two branches and the floating ice in the fjord downstream of the grounding line.

Table 2.2: Table of TerraSAR-X speckle tracking data acquired in the 'danaf_HYD1421' project, which was used for an alternative velocity field against which the InSAR velocity field can be compared.

Aquisition Date	Start Time	Stop Time	Orbit	Strip	A/D
12/05/2012	12:22:59	12:23:07	006	010	A
23/05/2012	12:23:00	12:23:08			
12/05/2012	12:23:07	12:23:15	006	010	A
23/05/2012	12:23:07	12:23:16			
12/05/2012	12:23:15	12:23:23	006	010	A
23/05/2012	12:23:15	12:23:24			
13/05/2012	12:06:01	12:06:09	021	012	A
24/05/2012	12:06:01	12:06:09			
15/05/2012	11:31:59	11:32:07	051	010	A
26/05/2012	11:32:00	11:32:08			
20/05/2012	11:40:29	11:40:37	127	009	A
31/05/2012	11:40:30	11:40:38			
20/05/2012	11:40:37	11:40:45	127	009	A
31/05/2012	11:40:38	11:40:46			

2.1.3 – ICESat Data

The baseline refinement step in the processing chain requires a DEM for precise elevation data. The TanDEM-X covers a small area, so is not ideal for this process. High precision elevation data is available for the Skelton Glacier from NASA's ICESat data, which is what is used for the baseline refinement. The ICESat data is recorded as elevations every 170m along orbit tracks. The coverage across a scene is poor and requires interpolation to create a raster DEM, but for the baseline refinement which requires GPSs, the recorded points are sufficient (Figure 2.2). The baseline refinement using this ICESat data is explained further in Chapter 4.4.

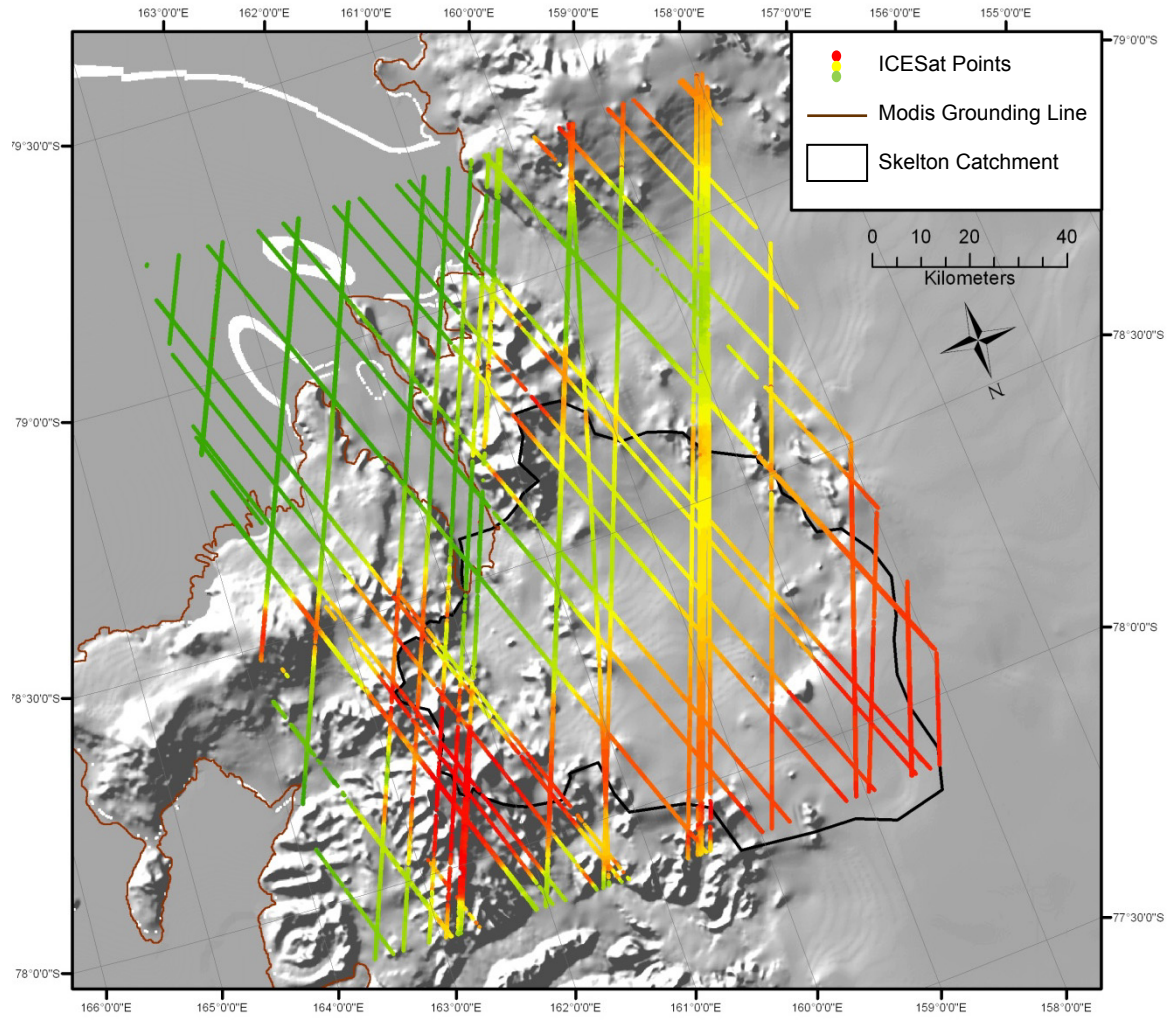

Figure 2.2: Image showing the ICESat points that were acquired over the Skelton Glacier. The colour of the points represents elevation, where green is low and red is high. The background image is a hillshade image of the RAMPv2 DEM. Displayed in Polar Stereographic.

2.2 – Digital Elevation Models

Creating a DEM of Antarctica including the Transantarctic Mountains is challenging due to the continent's isolation and the partly rugged terrain. Using satellites to acquire elevation data is also a challenge due to the polar orbits not directly crossing the poles and imaging geometries not always being ideal, leaving gaps in the data coverage. Attempts at creating high quality DEM's using different platforms and instruments have had mixed results, with errors still high in some datasets (Bamber & Gomez-Dans, 2005). A mixture of medium and high resolution elevation data described below have been used in this study.

2.2.1 – Radarsat Antarctic Mapping Project version 2 (RAMPv2)

In 2001, a project was undertaken which involved taking the best DEM's available, and combining them to create an Antarctic-wide elevation model. This has been labelled RAMPv2 as it is based upon the original version of the RAMP DEM, but with new data, error corrections and a larger coverage. The RAMPv2 DEM was used as the main elevation model for the interferometric processing. RAMPv2 combines elevation data from a range of methods including satellite radar altimetry, airborne radar surveys, topographic maps, ground GPS measurements and data from the Antarctic Digital Database (ADD) (Liu *et al.*, 2001). From the combination of different elevation data, a complete coverage of Antarctica has been achieved and available free from the National Snow and Ice Data Centre (NSIDC). The spatial resolution of the DEM differs depending on the location and acquisition technique, ranging from a 200m horizontal resolution on the Antarctic Peninsula and Transantarctic Mountains, to a 10km horizontal resolution at latitudes south of 81.5°. (Liu *et al.*, 2001). Currently there are high precision DEM's for Antarctica, though these usually are for flat regions and not mountainous areas. The Skelton Glacier is within this mountainous region which can be difficult to get high precision DEM's. The RAMPv2 DEM has a resolution of 200m in the Skelton Glacier location in the TAM, which is much coarser than the interferometric data being analysed. For differential SAR interferometry (DInSAR), differential InSAR pairs are needed, which are not available for this area from the ERS satellite. Instead, a precise DEM is needed to create a synthetic interferogram and allow the SAR data to be processed by separating the topographic phase information from the motion phase (see section 3 for details). The RAMPv2 DEM is not precise enough due to its coarse resolution compared with the interferometric data, so the higher resolution TanDEM-X is required.

2.2.2 – TanDEM-X

In mid-2012, new high quality satellite data became available from the TanDEM-X mission in Antarctica, which enable the interferometric generation of precise digital elevation models. As no operational product is yet available, TanDEM-X data have been processed to a DEM for the study area at Gateway Antarctica. The TanDEM-X mission is run by the German Aerospace Center (GAC) with an aim of creating a very high resolution global DEM. The satellite system consists of two TerraSAR-X satellites flying in formation since 2010. The first TerraSAR-X satellite was launched in 2007, three years before a second almost identical satellite was launched (Lopez-Dekker *et al.*, 2011). This new satellite (TanDEM-X) is flown a few hundred meters from the TerraSAR-X satellite so that data can be recorded synchronously, resulting in a higher resolution, better quality DEM. Data from TanDEM-X was acquired on 12-Sep-2011 under the DLR project *XTI_GLA0559*, in Single Look Complex (SLC) format which has been processed to DEMs with 20m resolution using the GAMMA software package. A SLC image has the phase and amplitude information retained from the radar

signal, and has the data stored in slant range (Jackson & Apel, 2004). The data received covered a small section of the study area surrounding the grounding zone where the two glacier branches join. This higher resolution DEM was embedded within the coarser resolution RAMPv2 DEM using ENVI (see Figure 2.3).

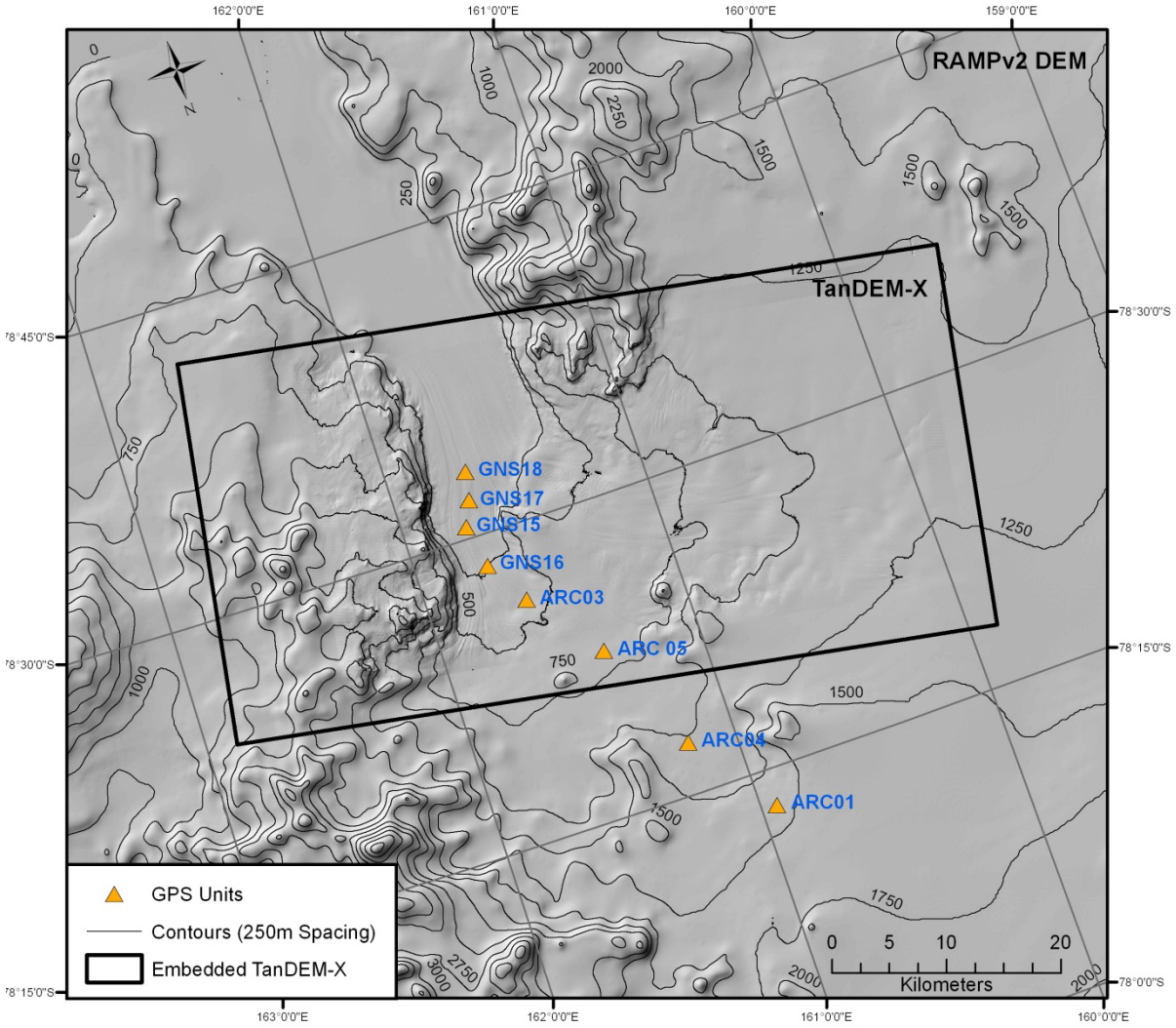

Figure 2.3: The higher resolution TanDEM-X embedded within the lower resolution RAMPv2 DEM. The TanDEM-X covers the grounding zone and converging of the two arms of the Skelton Glacier. Displayed in Polar Stereographic projection.

2.3 – GPS

GPS units were deployed on the North Branch of the Skelton Glacier within Antarctica NZ project K001B-I for ground truth measurements to which the InSAR velocities can be compared (Figure 2.3). The line of GPS units stretched from near the convergence of the glacier branches, to the higher reaches of the Skelton catchment. By locating GPS units on either side of the assumed grounding

zone, measurements of grounded and ungrounded glacier ice could be obtained. The GPS were deployed on the surface of the ice during the summer of 2011/2012 and recorded data every fifteen seconds for 38 days. The data the GPS units recorded was the latitude, longitude and elevation data (relative to the WGS-84 reference ellipsoid) for each location. To find the velocity and bearing measurements, the GPS data was processed using the GIPSY Precise Positioning Software (Zumberge *et al.*, 1997) within a PhD project at Gateway Antarctica (pers. comm. O. Marsh, 2012). The processed velocity was scaled to metres per year, and the processed bearings are calculated in geographic coordinates where a bearing of 000° relates to true north. Processing using the GIPSY program gives the GPS point velocities at an accuracy of ±0.2cm which equates to approximately $\pm 0.2 ma^{-1}$ uncertainty per GPS unit, after the data has been averaged over the 38 days. The bearing error is estimated with atan(0.2/v) in degrees, relating to the magnitude of the velocity (v) of that GPS unit. Lower errors are expected with large velocities, and higher errors for small displacements. Table 2.3 shows both the position, velocity and bearing of the 8 GPS stations. The velocity and bearing was transformed to the Polar Stereographic projection when used to compare with the interferometrically processed satellite data.

Table 2.3: GPS units deployed on Skelton Glacier with the recorded and processed information. The elevation is in relation to the WGS-84 reference ellipsoid, and the bearing is the true bearing in degrees from true North. Data supplied by O. Marsh (pers. Comm, 2012)

GPS Unit	Longitude	Latitude	Elevation	Velocity (m/a)	Bearing
ARC01	160.938553	-78.220901	1461.31	12.69	143
ARC03	161.612137	-78.439987	350.88	135.79	134
ARC04	161.188705	-78.291008	1054.32	70.67	152
ARC05	161.385727	-78.381882	656.90	64.20	162
GNS15	161.749954	-78.509827	172.65	115.50	192
GNS16	161.717178	-78.475403	232.89	138.28	165
GNS17	161.706924	-78.529480	122.19	100.88	205
GNS18	161.684357	-78.551903	117.12	106.35	188

2.4 – Accumulation Data

Accumulation data of the Skelton catchment was used to estimate the amount of snow falling within the catchment zone over a period of a year. This estimate can be then compared to the ice flux at various cross-sections along the glacier tributaries. Two accumulation datasets are used to allow for comparison of accumulation in the Skelton catchment and mass balance information at each flux gate. One accumulation dataset was acquired from *in situ* measurements of snow accumulation, interpolated using observations from the AMSR-E satellite radiometer (Arthern *et al.*, 2006). The second accumulation dataset is acquired from an Antarctic climate model which has been developed by the Institute for Marine and Atmospheric research Utrecht (IMAU) (Lenaerts *et al.*, 2012).

Figure 2.4 shows the difference between these two accumulation datasets for the Skelton Glacier. The climate model accumulation data is significantly higher over the TAM near the Ross Ice Shelf where values are up to 400 Gt a^{-1} higher than the AMSR accumulation data. Over the Skelton Glacier catchment the two accumulation datasets have a smaller difference between them, but the AMSR accumulation dataset is higher over this region.

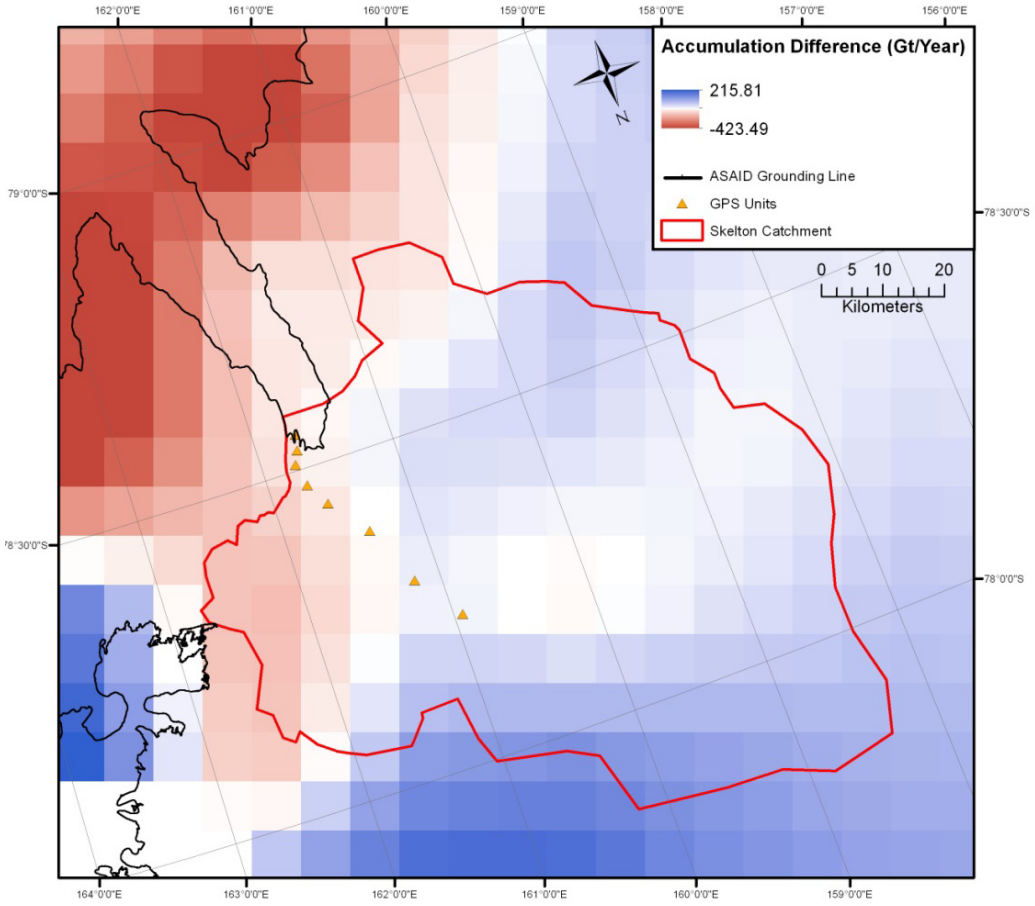

Figure 2.4: Difference map between the AMSR accumulation map and the IMAU accumulation map. Red areas indicate where the IMAU accumulation is highest, and blue areas indicate where AMSR accumulation is highest. Original resolution of the accumulation datasets was approximately 25km, but have been resampled to an 8km resolution for this image.

3 – Principles of Interferometric SAR processing

This chapter will focus on the fundamentals of active microwave remote sensing systems, the more refined technique of synthetic aperture radar (SAR) and the application of interferometry which arises from these remote sensing techniques. Satellite-borne radars have been successfully used in earth science for about 20 years on an operational basis (e.g. Goldstein *et al.*, 1993; Rosen *et al.*, 1996; Wright, 2002). One of their advantages is the ability to record images both day and night and in all weather conditions at varying spatial resolution (Richards, 2005). This is due to the radar being an active system using microwave energy to illuminate the earth's surface at a wavelength in the electromagnetic spectrum with very small atmospheric interference. This is especially true for polar-regions where the atmosphere is normally very dry, while other regions can have more noticeable atmospheric distortions due to humidity related atmospheric path delays.

3.1 – Real Aperture Radar

Monostatic radar systems on satellites transmit electromagnetic waves in the microwave spectrum using a radar antenna and receive the energy backscattered from the earth surface to the same antenna. Neglecting atmospheric loss and taking into account the range spreading loss, the roughness and dielectric properties of the target area determines the level of backscatter received by the radar receiver. This can be mathematically described by the radar equation where the power being received by the antenna (P_r) in watts is:

$$P_r = P_t \cdot \frac{G^2 \lambda^2}{(4\pi)^3 R^4} \cdot \sigma \qquad (3.1)$$

P_t is the power transmitted by the antenna in watts, G is the antenna gain, λ is the wavelength, σ is the radar cross-section (or backstatter coefficient), and R is the distance from the radar to the target (can also be represented as R_t^2 and R_r^2 when the transmitter and the receiver are at different locations and the ranges are different) (Richards, 2009; Rotschky, 2007). The radar can use microwave bands ranging from frequencies of less than 1GHz (P-Band) up to over 26GHz (Ka-Band), but the ERS data used for this research is in the C-Band (frequency of 5.3GHz and wavelength of 5.66cm). The wavelength (or frequency) of the SAR band determines the penetration depth of the transmitted wave into snow and to which extent the atmosphere, surface and snow volume scatters the radar wave (Rignot *et al.*, 2001). Electromagnetic waves can oscillate in a number of ways described by their polarisation (linear, circular or elliptical polarisation) (Radzevicius & Daniels, 2000). This polarisation of the backscattered signal can help with the distinction of objects on earth (Sanden, 1997).The microwaves used by SAR systems are usually transmitted as linear polarisation in either

horizontal (H) or vertical (V) polarisation. This is determined by the antenna and receiver set up. The product that is produced from a SAR system will therefore have a specific polarisation; either like-polarised (HH or VV), or cross-polarised (HV or VH). The first letter describes the received polarization, and the second letter corresponds to the transmitted polarization. The ERS-1/2 products have a linear vertical polarisation (VV), meaning the microwaves are transmitted and received in vertical polarisation (Table 3.1).

Table 3.1: Parameters of the ERS-1/2 and the TanDEM-X Satellite configurations

Radar Parameters	ERS-1/2[1]	TanDEM-X[2]
Wavelength (λ)	5.66cm	3.1cm
Frequency	5.3GHz (C-Band)	9.65GHz (X-Band)
Polarisation	Single - VV	Single - HH, HV, VH, VV Dual - HHHV, HHVH, VVHV, HHVV
Bandwidth (B)	15.55MHz	Up to 150 MHz
Transmitted Pulsewidth (τ)	64ns	Up to 6.7ns
Antenna Length (L)	10m	4.8m
Orbit Height (H)	782km	514km
Slant Range (R)	850km	547km to 896km
Incidence Angle	23°	20° to 55°

[1] (Oliver & Quegan, 1997)
[2] (Krieger *et al.*, 2005), (Zink *et al.*, 2008)

The minimum range distance between two points on the surface which can be separated by a pulsed radar system is given by the range resolution. The transmitted pulse width (τ) is the main factor which determines the resolution in slant range (R_s), which is defined by:

$$R_s = \frac{c\tau}{2} = \frac{c}{2B} \tag{3.2}$$

where τ is the duration of the compressed pulse in seconds with bandwidth B (the pulse width is equal to the reciprocal of the bandwidth: $\tau = \frac{1}{B}$), and c is the speed of light (approximately $3x10^8$m/s) (McCandless & Jackson, 2004). For the ERS satellite, the slant range resolution is calculated to be 9.6m (Ketelaar, 2009). The corresponding ground range resolution (R_g) is given by:

$$R_g = \frac{c\tau}{2sin\theta} \tag{3.3}$$

which is 24.6m for ERS at the scene centre. Figure 3.1 displays the geometry of the ERS satellite radar system radar, where A is the satellite position along the flight path (orbit); H is the height above the earth, R is the slant range between the radar sensor and the point on the ground that is being illuminated and θ is the incidence angle that the radar transmitter looks away from the nadir. This incidence angle for the ERS satellite is 23° in the scene centre, although the near-range and far-range have incidence angles of 18° and 24° respectively.

For real aperture radar the resolution in the range direction is higher than the azimuth direction, which is reliant on the beam width and the radar footprint. The azimuth resolution (R_a) is defined by:

$$R_a = \frac{H\lambda}{L} \tag{3.4}$$

where H is the height of the radar system above the earth, λ is the wavelength of the transmitted waves and L is the length of the antenna (Chan and Koo, 2008). All parameters are in metres. Depending on the radar sensor, the incidence angle, the wavelength and the height of the platform (when using a satellite as the radar platform) are all constants, as is the speed of light. Therefore the main factor that affects the resolution (mainly in the azimuth direction) is the length of the antenna. With a real aperture radar system, the azimuth resolution will never be high. The ERS satellite has an antenna that is 10m in length, which gives an azimuth resolution of 4.4km. One way to overcome this problem and improve the azimuth resolution is to use the technique known as Synthetic Aperture Radar.

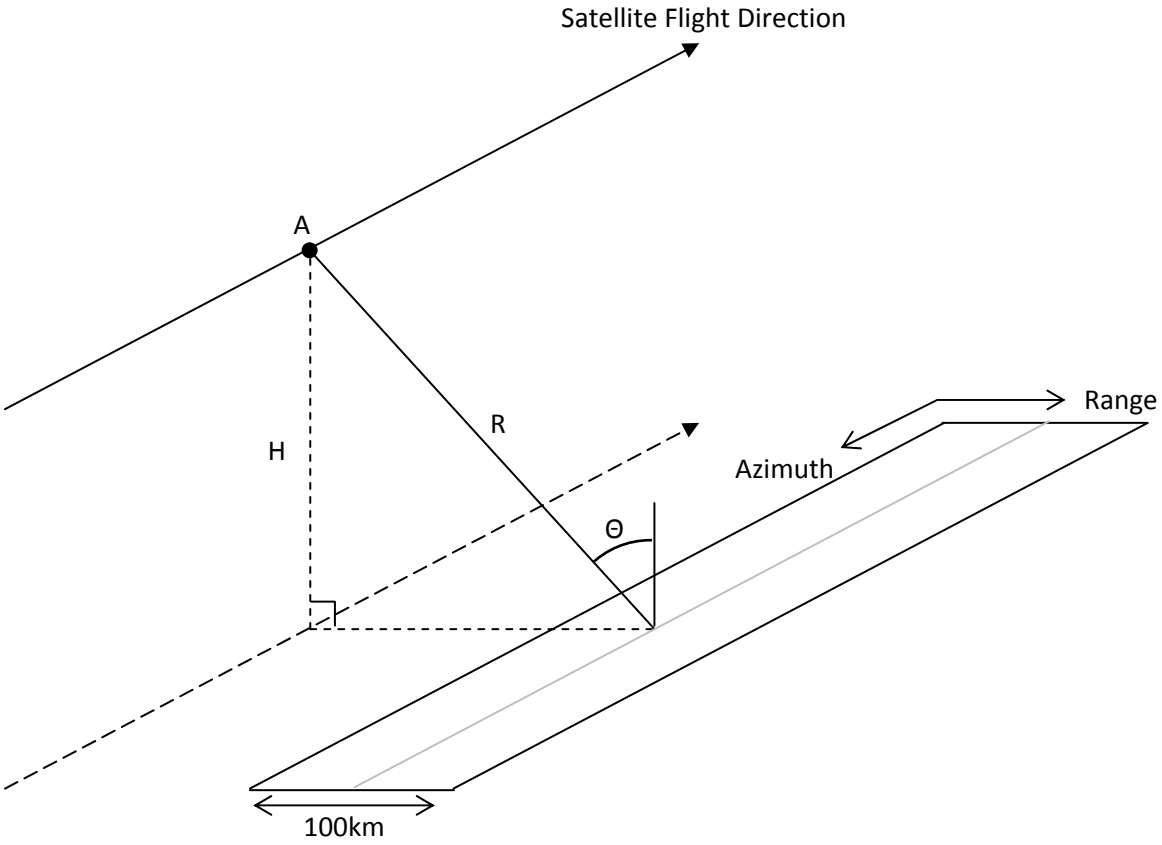

Figure 3.1: Geometry of the ERS Satellite. A is the satellite location along the flight path; H is the height above the earth (approximately 780km); R is the slant range and θ is the incidence angle (23° in the centre of the swath)

3.2 - Synthetic Aperture Radar (SAR)

The length of the synthetic antenna (Wilson & Crary, 1961) is approximately corresponds to the radar footprint of the real antenna (Figure 3.2). Point A is the target that is being illuminated by the radar antenna during the overflight. As the plane or spacecraft moves along the flight path, the target continues to be within the illumination swath, with information being recorded for all positions. Using doppler beam processing the individual targets are identified in every reflected radar pulse during the overflight allowing coherent integration and beam sharpening. The resulting product is a SLC image.

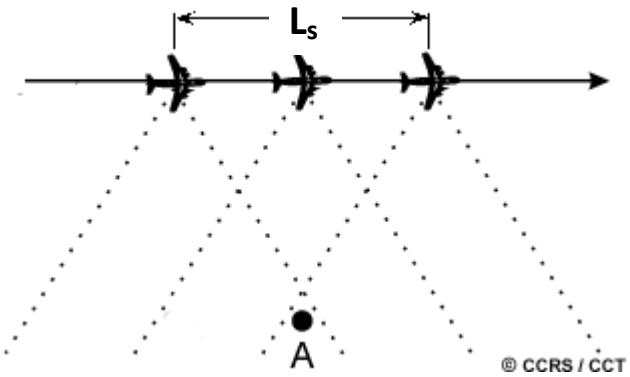

Figure 3.2: Diagram showing the illumination of a target (A) by a SAR system during the overflight. L_s is the synthetic length of the SAR (obtained from the National Resources Canada website http://www.nrcan.gc.ca).

This product can then be used for interferometric SAR processing. For SAR, the ground resolution in the azimuth direction (R_a) is:

$$R_a = \frac{L_a}{2} \tag{3.5}$$

where L_a is the length of the antenna (Oliver & Quegan, 1997). This implies that the azimuth resolution is half the length of the antenna and is independent of radar range or the wave frequency. Using the same ERS satellite in previous examples, the azimuth resolution using a synthetic aperture radar is approximately 5m (half the length of the antenna). If the antenna is short, the resolution in the azimuth direction is higher, which is opposite to a real aperture radar where a longer antenna gives higher resolution.

As with any side looking radar, data measurements of steep topography can result in foreshortening and layovers which become very noticeable using high resolution SAR imagery (Figure 3.3). Foreshortening occurs when the higher topography is closer to the sensor than the surrounding land resulting in the returned pulse arriving early. Point A and B in Figure 3.3 are the base and summit of a mountain respectively at a given distance apart; however, point B is closer to the sensor than it would

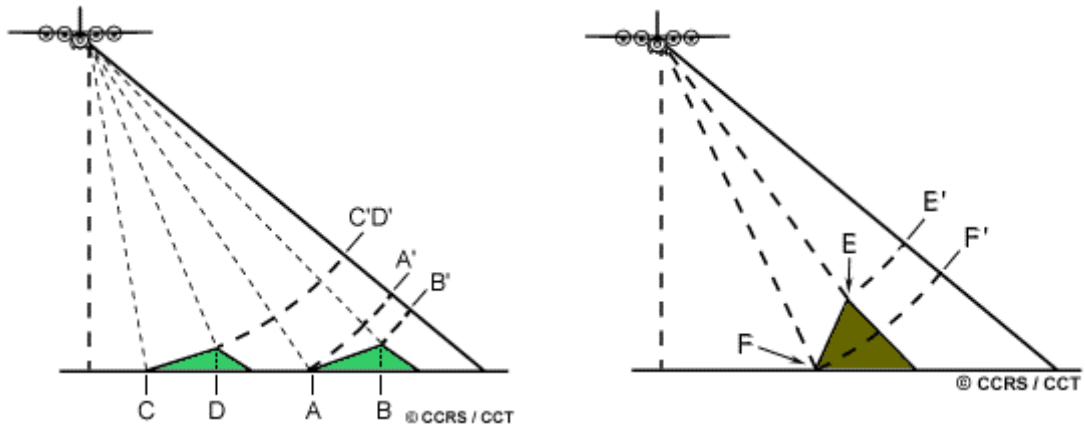

Figure 3.3: Diagram showing foreshortening and layover geometries. A' and B' show the foreshortening resulting from topography, while E' and F' show an instance of layover, where the high topography is closer to the sensor than the low topography (F) (obtained and modified from the National Resources Canada website http://www.nrcan.gc.ca).

be if it was at the same elevation as A, so on the SAR image (acquired in slant range) these two points will be occurring closer together than in reality (point A' and point B'). Layover occurs when the higher topography (point E) is closer to the sensor than the lower topography (point F) meaning the pulse arrives back from point E before point F. In both these cases the topography will look distorted on the radar images, with slopes being shortened nearer to the satellite sensor, and elongated away from the sensor (for an example of this, see Figure 3.4). Shadowing occurs when the slope behind point B (away from the sensor) is not seen by the sensor at all. These geometric distortions can be corrected using the slant to ground method, the polynomial method, or the radargrammetric method. The slant to ground method was used for the geometric corrections of this research, which was implemented within the GAMMA geocoding program (See Chapter 4). This method projects the acquired slant range values to the ground range by using the imaging geometries and a terrain model (Mansourpour *et al.*, 2008).

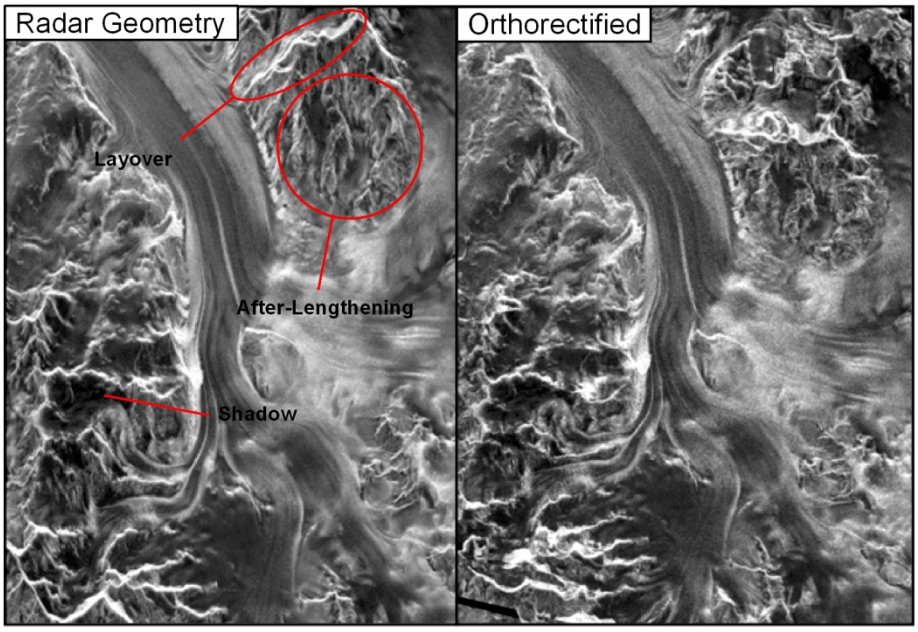

Figure 3.4: Image showing the layover and shadow effects in the amplitude image (in radar geometry), compared with an orthorectified image where these effects are not present.

3.3 – Interferometric Synthetic Aperture Radar (InSAR)

If two of the SAR images taken are from a very similar location at different times, the difference in phase information between the two can be used to determine displacement on the earth's surface. This technique is known as Interferometic Synthetic Aperture Radar (InSAR) (Massonnet & Feigl, 1998). There are two different techniques which can be used for InSAR: single-pass SAR Interferometry and repeat-pass SAR Interferometry (also called DInSAR). The single-pass method (Figure 3.5a) involves having an additional receiver on board to detect the backscatter along with the main antenna/receiver sensor. The distance between these is the baseline (B). The repeat-pass method (figure 3.5b) involves

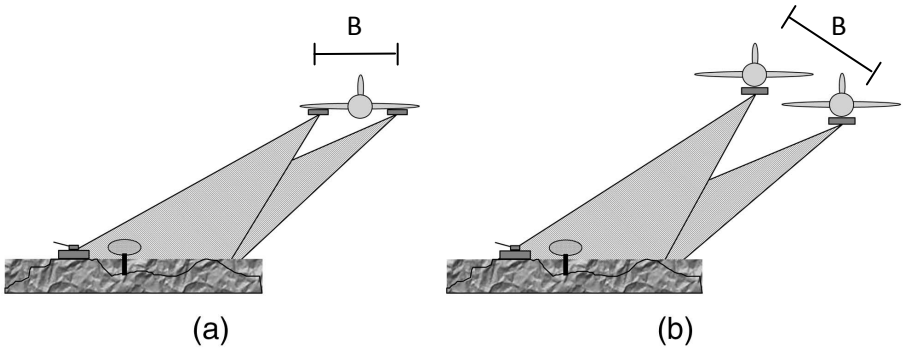

Figure 3.5: Single-pass (a) and repeat-pass (b) interferometric methods (M. A. Richards, 2007). B represents the baseline for each method.

an image being acquired by a single antenna and receiver but at two different times. The former technique focuses on the different angles the data is received from and is mainly used in creating high quality digital elevation models of the earth's surface due to fewer errors than the repeat-pass (Zhong *et al.*, 2003). The latter technique focuses on the earth's surface at two different acquisition times, and displays the displacement that may have occurred between them (in addition to topographic measurements). Figure 3.6 shows the geometry of the repeat pass InSAR method where B, B_{II} and $B_{\perp}$ are the baseline, parallel baseline and perpendicular baseline respectively; θ is the incidence angle, and R_1 and R_2 are the slant ranges for each of the acquisitions. This second technique will be utilised in this research.

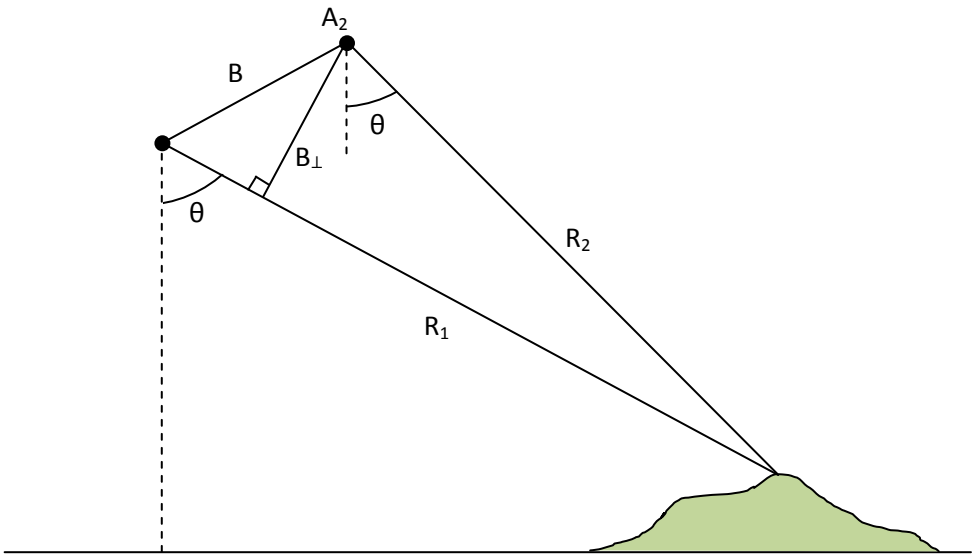

Figure 3.6: Geometry of the repeat pass InSAR system. A_1 and A_2 are the ERS-1/2 satellite positions on consecutive days with B being the baseline between the acquisition positions; B_{II} being the parallel baseline and $B_{\perp}$ being the perpendicular baseline. θ is the incidence angle and R_1 and R_2 are the slant ranges for each acquisition.

3.4 – Phase Information

The signal that the radar transmits contains the amplitude and phase information of the backscattered image. The amplitude is a measure of how much of the backscattered signal is received (i.e. the strength of the return signal), and the phase that is recorded is the fraction of the last wavelength being received at the receiver (the number of wavelengths is not recorded). InSAR makes use of the phase difference that is measured between two different acquisitions (see Figure 3.7), by displaying this difference on an image as coloured fringes (Fletcher *et al.*, 2007a). These coloured fringes are formed due to the 2π sinusoidal waves, where each fringe displays the phase difference between the images as –π to +π. This phase information is known as the interferometric phase, and is displayed as an interferogram.

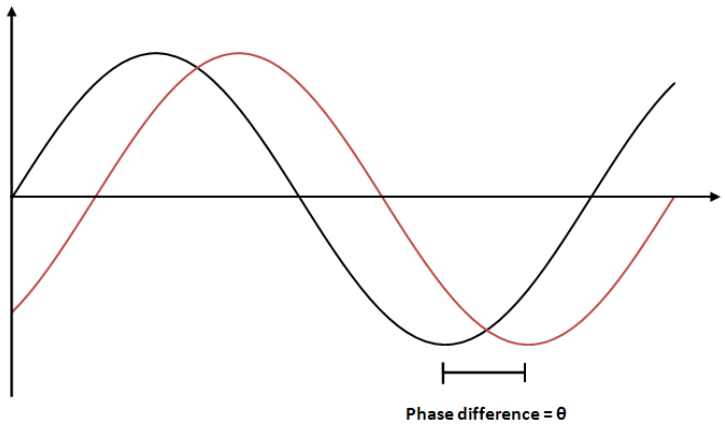

Figure 3.7: The phase difference (or phase shift) of the return wave at two different acquisition times. This phase difference is used to generate an interferogram.

Within this interferometric phase are multiple contributions which need to be removed, leaving only the phase contribution from displacement. The sum of these phase contributions make up the overall interferometric phase:

$$\Delta\phi = \Delta\phi_{atmosphere} + \Delta\phi_{displacement} + \Delta\phi_{noise} + \Delta\phi_{topography} \quad (3.6)$$

(Bombrun *et al.*, 2009). The $\Delta\varphi_{atmosphere}$ is related to the different atmospheric conditions between the two acquisitions times and can include differences in humidity, temperature and pressure. For this research, it is assumed that the polar atmosphere is dry and does not greatly affect the transmitted waves during the data acquisition. It is also assumed that the atmosphere is unchanged between the two acquisition dates. $\Delta\varphi_{noise}$ relates to the poor quality data relating to decorrelation between the two SAR images. If there is poor coherence between the images, there will be high amounts of noise which can result in lower quality results in these areas (see Chapter 3.5). $\Delta\varphi_{motion}$ is the phase contribution arising from movement observed between the acquisition dates. $\Delta\varphi_{topography}$ is the phase contribution arising from topography around the image location. The phase contribution from the atmosphere is assumed to be low and is ignored for this research, which will leave a small uncertainty in the final data. The phase contribution from noise lowers the quality of the images and can lead to higher uncertainties in the processing, but can be minimised by filtering the images or multilooking (average results from multiple images).

Eliminating or minimising the effect of the phase contributions from the atmosphere and noise leaves the motion and topography phases. These two are intermingled in the data and need to be separated for specific velocity analysis to take place. These remaining phase contributions are displayed in

colour fringes and represent a change in elevation (known as the altitude of ambiguity, h_a) and the change in horizontal or vertical motion. The altitude of ambiguity is defined by:

$$h_a = \frac{\lambda R sin\theta}{2B_\perp} \tag{3.7}$$

where λ is the wavelength of the transmitted signal, R is the range distance from the sensor to the target, θ is the incidence angle and $B_\perp$ is the perpendicular baseline (Rott, 2009). This equation shows that the altitude of ambiguity is inversely proportional to the perpendicular baseline. The phase shift which relates to motion is defined by:

$$\Delta\phi_{motion} = \frac{4\pi}{\lambda}\left(\delta_y\, sin\theta - \delta_z\, cos\theta\right) \tag{3.8}$$

where $\Delta\varphi_{motion}$ is the phase contribution from motion, λ is the wavelength of the transmitted wave, θ is the incidence angle, and $\delta_{y/z}$ is the displacement in the horizontal or vertical directions (Henry *et al.*, 2004). To determine the phase shift of a single fringe in the horizontal or vertical direction, Equation 1.8 can be rearranged, and separated into each element. The unwrapped motion phase ($\Delta\varphi_{motion}$) represents the motion fringes which are still wrapped and within the 2π ambiguity, so can be replaced with 2π in the equation. The resulting equations for the horizontal motion ($\delta_{y2\pi}$) and vertical motion ($\delta_{z2\pi}$) that is displayed in one fringe, is:

$$\delta_{y2\pi} = \frac{\lambda}{2\sin\theta} \tag{3.9}$$

$$\delta_{z2\pi} = \frac{\lambda}{2\cos\theta} \tag{3.10}$$

where λ is the wavelength, θ is the incidence angle, and $\delta_{y/z2\pi}$ is the phase shift of one fringe (2π) due to horizontal (y) or vertical (z) movement. This gives the horizontal and vertical displacement of one fringe in the interferogram. The ERS-1/2 satellite configuration has a C-Band sensor which transmits a wavelength of λ=5.66cm, and an incidence angle of approximately θ=23° in the scene centre. Using these constants, it can be worked out that one motion fringe in an interferogram is equivalent to a horizontal displacement of 7.24cm and a vertical displacement of 3.07cm. This shows that it is more sensitive to vertical motion than horizontal motion.

3.5 – Unwrapping

The information at this point is still wrapped in this 2π ambiguous phase, which only displays data as radians between –π and +π. To change this 2π ambiguity to information relating to real topography or

displacement values, the interferogram must be unwrapped. The unwrapping process takes the wrapped phase value at a pixel and determines the number of 2π cycles which need to be added at that point to give the unwrapped value, which is represented by:

$$\psi = \phi + 2\pi \cdot n \tag{3.11}$$

where n is the number of 2π cycles, φ is the wrapped phase and ψ is the resulting unwrapped phase (Fletcher *et al.*, 2007b). Figure 3.8 shows how unwrapping the interferogram changes the wrapped 2π cycles into unwrapped values representing topography or displacement.

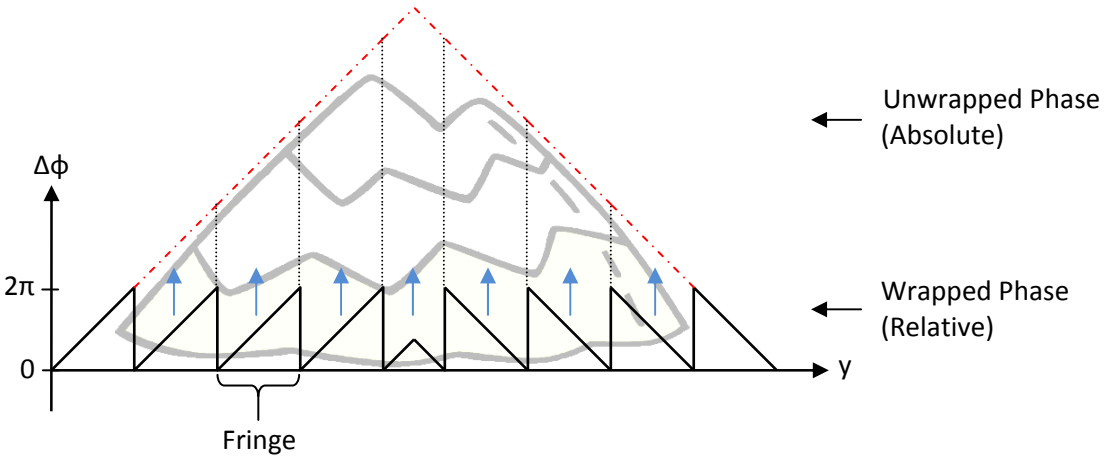

Figure 3.8: Image showing how the unwrapping procedure works. The Wrapped Phase consists of unambiguous fringes which cycle between 0 and 2π. Unwrapping changes this to absolute data with real number values which represent the actual topographic or displacement values (see Chapter 3.4 for motion and topographic values per fringe for ERS)

3.6 – Phase Coherence

When the scattered signal is not identical between two complex SAR images at a pixel level, there is decorrelation between the corresponding pixels between the two images. This decorrelation between the two images is called the coherence (γ), and is defined by:

$$\gamma = \frac{E[v_1 v_2^*]}{\sqrt{E[v_1 v_2^*]E[v_1 v_2^*]}} \tag{3.12}$$

where v_1 and v_2 is a pair of corresponding complex values, and E[ ] is the ensemble (statistical) averaging of the complex pair (Zebker *et al.*, 1994). This equation gives the estimate of the coherence, which is achieved by spatial averaging. The coherence of the pixels can be made into a

coherence map, where each pixel has a value between 0 and 1, with 0 being essentially zero coherence between the images (dark colour), and 1 being full coherence between the images (light colour). Figure 3.9 shows an example of a coherence image used in processing. Areas of an image which have high coherence will be useful for processing and will produce good quality data, while areas of low coherence will not process the data well and usually will produce errors or artefacts. This phase decorrelation is caused from numerous sources. Temporal decorrelation arises from large movements of the earth's surface between acquisition times (e.g. vegetation or water). Topographic decorrelation is due to large slope angles or distortions due to the side-looking aspect of the radars. These two are the dominant reasons, but decorrelation can also occur from thermal noise, baseline, misregistration or atmospheric effects (Hoonyol and Guo, 2001). These areas of decorrelation can lead to phase discontinuities in the created interferogram. These phase discontinuities can then propagate through the image during the unwrapping process, which can lead to global errors across the whole image (Goldstein *et al.*, 1988).

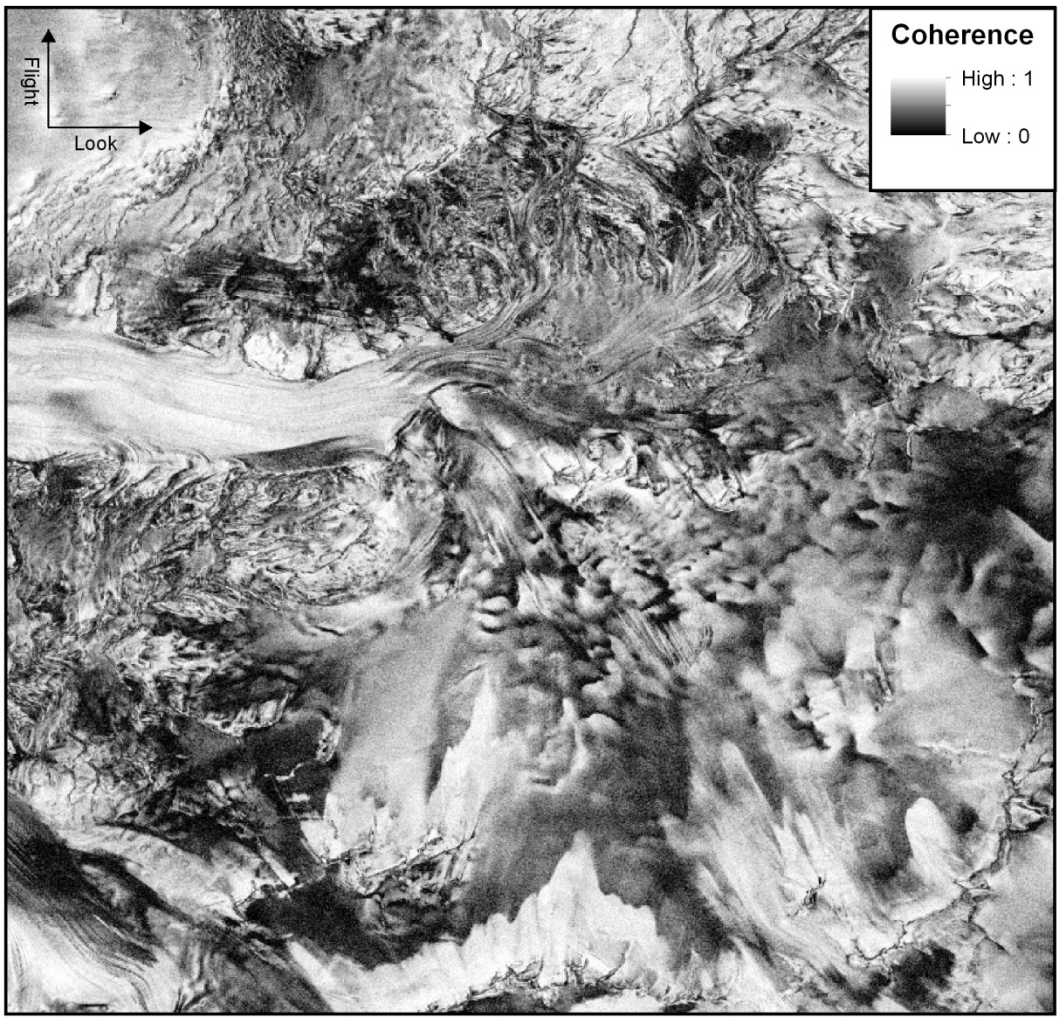

Figure 3.9: Coherence image of the Skelton Glacier (Track 456). Dark colours represent low coherence and light colours represent high coherence. Displayed in Radar Coordinates.

4 - Generation of a Surface Velocity Map

Through a range of different processing steps, the SAR data received from the processing and archiving facility in SLC format will be used to create ice velocity maps of the Skelton Glacier. The steps involved are: generation of a raw interferogram in radar geometry, the phase unwrapping, separation of the topographic and motion phase, refinement of the baseline, creation of a displacement map in radar range (line of sight of the radar), conversion of displacement in ground range (see Figure 4.1 for a flowchart of these steps). By completing these steps for multiple pairs of images, the combining of the individual displacement maps will be done to create a final 3D displacement map. With this final displacement map, flux gates can be created on the glacier, and velocity information can be interpreted with the aim of discovering discharge rates and mass balance measurements at locations along the glacier.

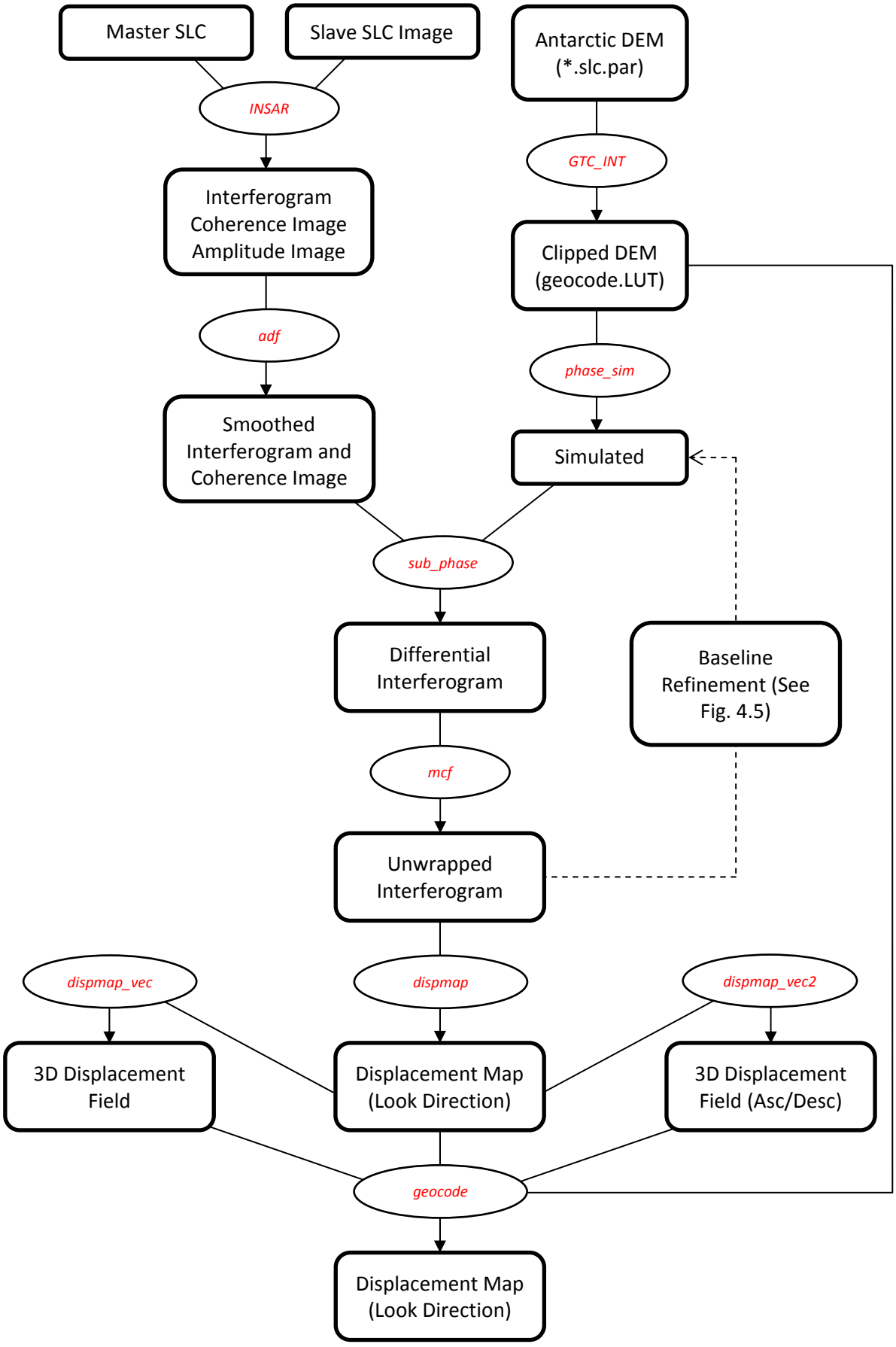

Figure 4.1: Interferometric Synthetic Aperture Radar processing flow chart showing each of the steps involved in processing the satellite data to an ice velocity field of the Skelton Glacier. The square boxes represent the files created at each step of the processing chain, while the oval boxes are the GAMMA programs or scripts used to create the resulting files.

4.1 – Interferogram Generation using the GAMMA software package

To produce an interferogram and a final ice velocity field, a number of programs were used to process the acquired satellite data. The main program used for SAR processing is the GAMMA Remote Sensing software suite. For this project, three of the software packages within the program will be used, including ISP (Interferometric SAR Processor), DISP (Display Tools), and DIFF&GEO (Differential SAR Processor & Geocoding). ISP includes algorithms for the main processing stages of the SAR data, including interferogram generation, coherence map generation and unwrapping. DISP allows the different types of generated images to be displayed and changed into universal formats (e.g. raster images). DIFF&GEO includes programs which aid with geocoding the images between radar coordinates and the desired map coordinate system specified by the user. It also has a range of programs which cover differential interferometry and displacement map creation. Most of the GAMMA processing is applied to images in radar coordinates, which have the top left corner of the image set with coordinates (0,0) and both azimuth and range directions increasing across and down the image. Within the DIFF&GEO software package are algorithms to change between the radar coordinates and the desired map projection. The projection that is used in this thesis is the Polar Stereographic projection with the true latitude at 71 °S. This projection offers no distortion in scale at 71°S with a six percent distortion present at the South Pole. The location of the Skelton Glacier falls at a location of only a few percent distortion and so will be best represented by this projection. Alongside the GAMMA programs, a range of other software was used to prepare, refine or display data. ENVI is an image processing and analysis program which was used to analyse and refine the processed images from the GAMMA software. From within the ENVI software, IDL was used to create and run scripts that were used for minor image processing involved in baseline refinement and image adjusting. The ArcMAP 10.1 module of the ArcGIS 10.1 software suite was used for further image analysis and final image preparation.

The radar data that was acquired was in a raw format from the supplier and had to be processed into a SLC format before interferometric processing could be done. To create an interferogram using the repeat-pass method, two SLC images must be acquired from similar locations with a small temporal difference. For the ERS-1/2 data, the temporal difference is one day and the distance between the satellite locations during acquisition is small, with a spatial baseline less than two hundred metres. The image acquired first (ERS-1) is the master image, with the second image (ERS-2) being the slave image throughout the processing. An automated script (*INSAR*) was used in this research to produce the interferogram in one step. The inputs were two SLC SAR images and their corresponding parameter files which include information about the SAR sensor, imaging geometry, and orbit state vectors [see Appendix for an example of a parameter file]. The two images are precisely co-registered and the baseline between the satellites is estimated. Also generated is a viewable amplitude image (Figure 4.2A), the coherence image describing the phase correlation (Figure 4.2B), and the

interferogram (Figure 4.2C). The interferogram includes the phase information from both the topography and displacement. The two phase components must be separated in order to produce a DEM or a displacement map. Examples of these different phase contributions in a raw interferogram are shown in Figure 4.2C, along with an example of a phase ramp created from orbital errors.

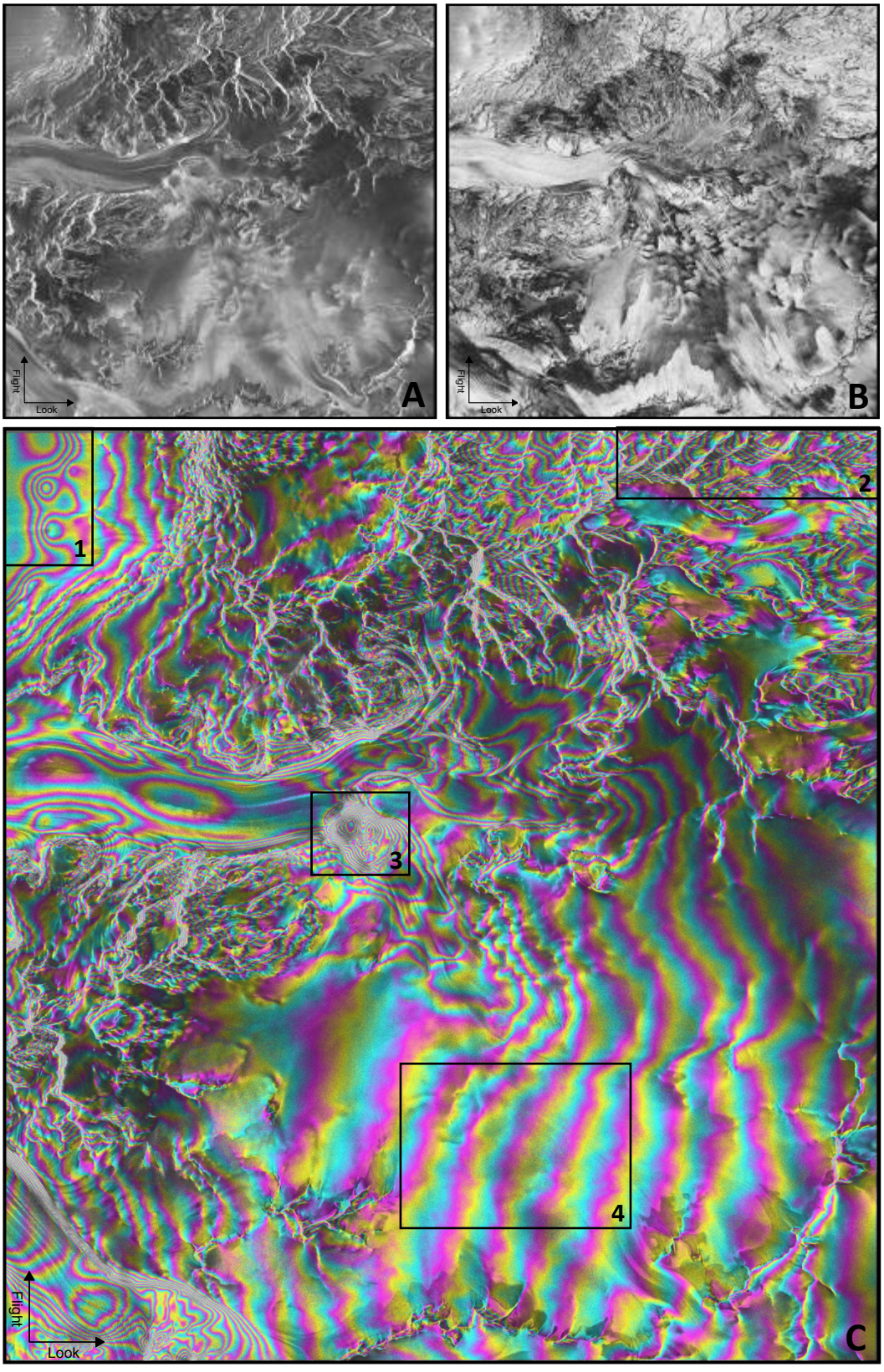

Figure 4.2: Output images from the *INSAR* scripts in radar coordinates. (A) is an Amplitude image, (B) is a Coherence image and (C) is a raw Interferogram. Within the interferogram, areas with a clear phase contribution are highlighted, with fringes primarily relating to vertical tidal movement (1), steep topography (2) and horizontal displacement (3) are shown. The unrealistic phase ramp in range direction is obvious at (4).

4.2 – Separation of Topography and Displacement Phases

In order to obtain velocity from interferograms with baselines larger than zero the topographic phase information needs to be subtracted to obtain the motion phase. There are three methods to do this: the two-pass method, the three-pass method, and the four-pass method (Massonnet & Feigl, 1998). The two-pass method uses a single interferogram and an external DEM. This DEM is used to simulate an interferogram containing only topographic fringes, which is then subtracted from the interferogram. As a result, only the displacement fringes are left. This method is heavily reliant on a good quality DEM, as incorrect elevation data will lead to artefacts in the velocity field. In the three-pass and four-pass method two independent interferograms with the same imaging geometry are subtracted from each other cancelling the motion phase and leaving a differential topographic phase. The latter can be used to construct a high resolution DEM in radar geometry. This differential InSAR (DInSAR) approach can be used if there was no change in ice velocity (an assumption which is not necessarily met in the grounding zone due to tides) (Gudmundsson, 2006). Three-pass InSAR uses three images with one SAR image used in both interferograms, while four-pass InSAR uses two independent interferograms. In our area, there is no DInSAR pair available from the ERS-1/2 mission, so the two-pass method was the only method that could be used. The RAMPv2 DEM with the embedded TanDEM-X frame was used as the external DEM for which the topography only interferogram would be simulated from.

The RAMPv2 DEM first must be clipped to the same dimensions as the interferogram. Another automated script was used to simplify this step. The script *GTC_INT* requires the parameter file of the master SLC image and the offset file (information regarding the interferogram geometry and properties; see Appendix) produced previously. The script creates a look-up table of points which is used to transform an image from a chosen projection into radar coordinates, and vice versa. The power images, coherence image and the interferogram are all projected into map coordinates (polar stereographic), and a subsection of the RAMPv2 DEM is extracted to fit to the geometry of these processed images. Once the external DEM was obtained in the geometry of the interferogram, the higher resolution TerraSAR-X DEM was embedded within the image by putting them into ENVI and using the georeferenced mosaicking tool. This DEM is required to be transformed into radar coordinates for further processing in GAMMA.

The GAMMA tool *phase_sim* takes this external DEM and simulates a ‘topography only’ interferogram from the elevation data. By subtracting this simulated interferogram from the original raw interferogram using the GAMMA tool *sub_phase*, only the displacement fringes remain. Figure 4.3 shows the interferogram before and after this step has been done.

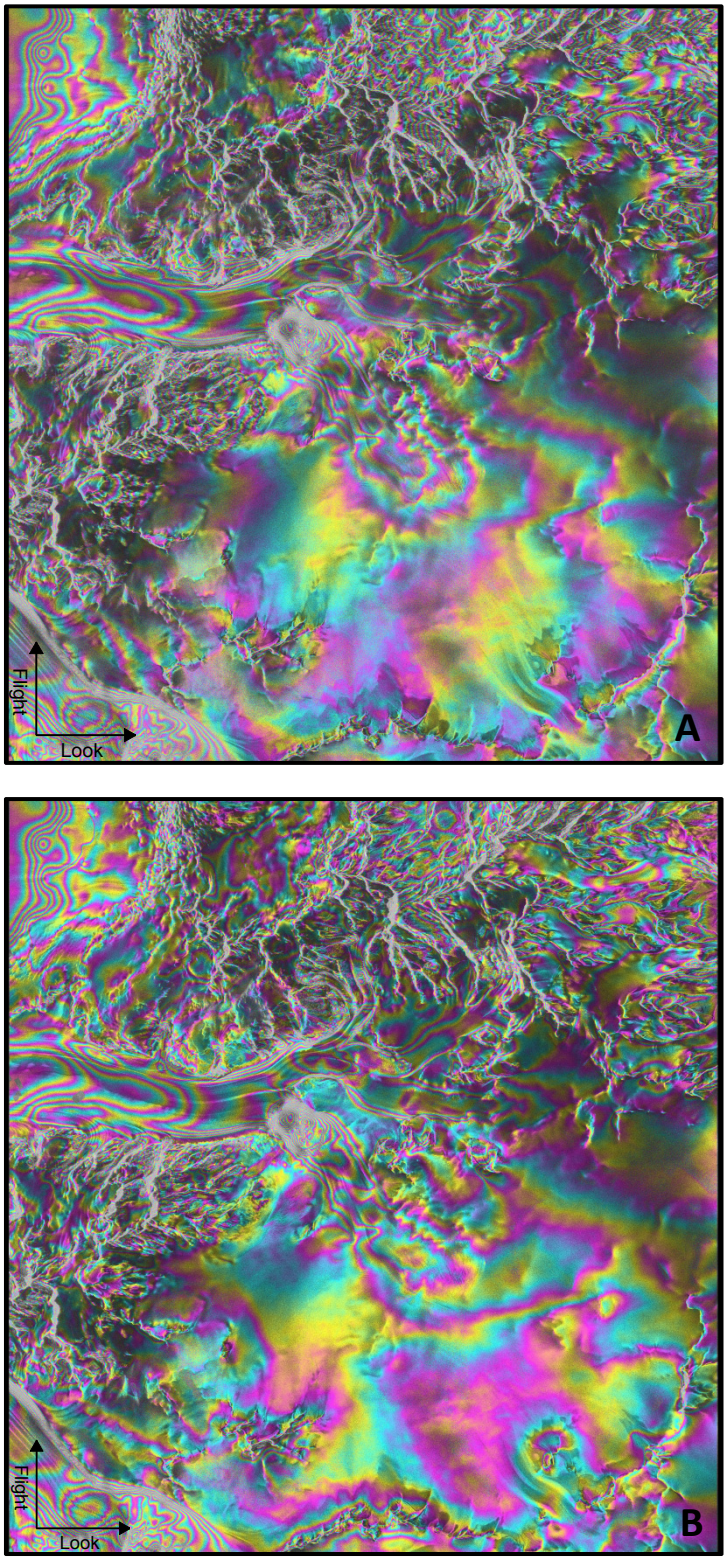

Figure 4.3: Comparison of an interferogram before and after the topographic fringes have been removed. The fringes in (A) include both displacement and topography fringes, while (B) displays only displacement fringes (known as a Differential Interferogram). Images are displayed in radar coordinates.

4.3 – Unwrapping

The information that remains in the differential interferogram must still be unwrapped to transform the relative phase data to absolute phase information. The GAMMA program has multiple tools which can unwrap interferograms using different methods. The one used for this thesis is the *mcf* tool, which stand for 'minimum cost flow' (For more information on the *mcf* tool, and other available unwrapping algorithms, see the GAMMA Documentation or Wegmüller *et al.* (2002). The *mcf* algorithm only requires the interferogram as an input, but can include a mask which removes poor quality or unneeded areas, or a weight file which specifies how discontinuities are managed (usually the coherence image is used as the weight file). Figure 4.4 shows the unwrapped differential interferogram. Colour fringes do still appear in the unwrapped interferogram, but do not represent a 2π cycle. Instead, they represent a given range of values per cycle, which can be altered when displaying the image.

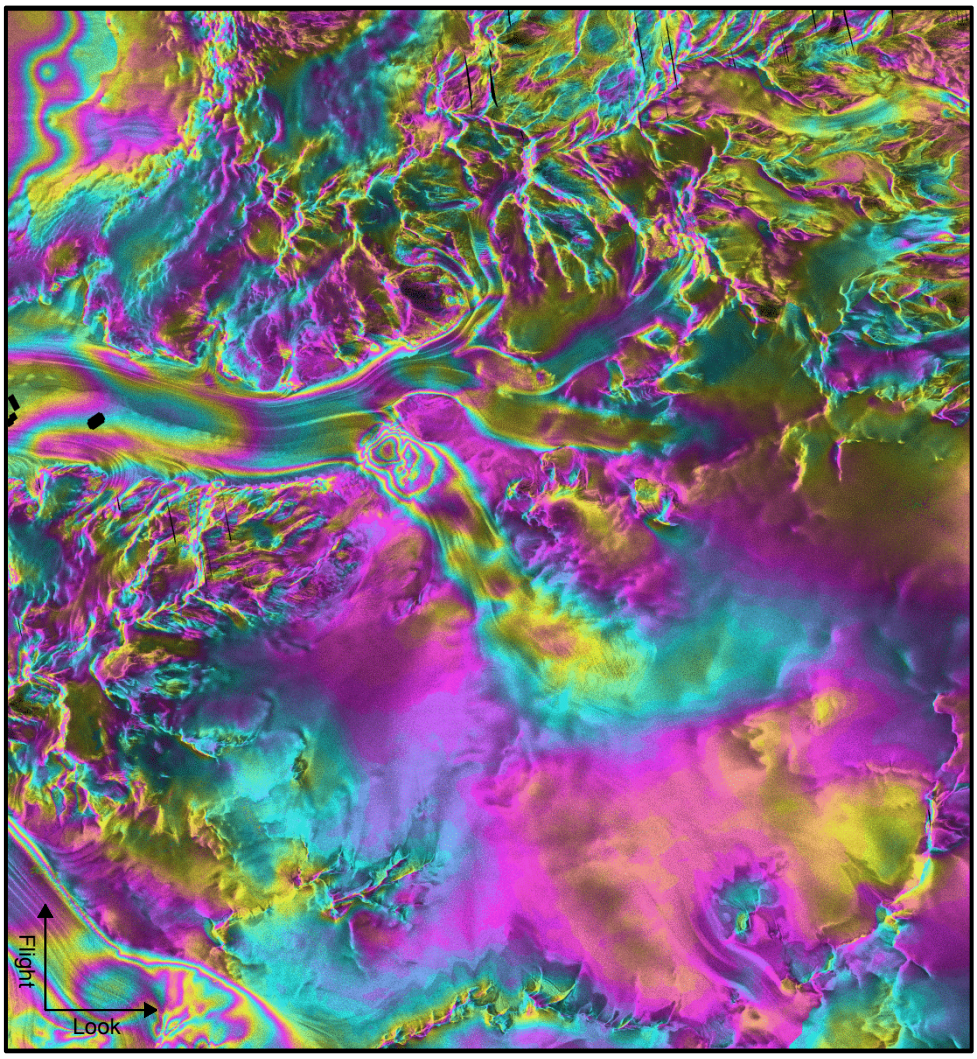

Figure 4.4: Unwrapped differential interferograms of the Skelton Glacier. Image displayed in radar coordinates.

4.4 – Baseline Refinement

The baseline that is estimated from the orbit data of the two satellites is known as the 'initial baseline.' The initial baseline was used throughout the processing up to this point, but the inaccuracies of the orbital data meant that this preliminary baseline estimate was not accurate enough. Inaccuracies primarily in the perpendicular baseline led to a phase ramp becoming visible across the interferogram, which causes the fringes to linearly align in radar range, where it is mixed with the displacement and topographic fringes (see the example in Figure 4.2C). To remove this phase ramp from the interferogram, a linear spatial trend can be estimated and subtracted from the interferogram (Bähr & Hanssen, 2009). Figure 4.5 shows an overview of the steps taken to refine the baseline and remove the phase ramp from the interferograms.

The first step requires the baseline to be refined to the 'precision baseline,' which is more accurate than the estimated initial baseline. The basis of this is to use ground control points (GCP) with elevation and unwrapped phase data to estimate a precision baseline. The location of the GCPs require that there is a large connected area across the map in range direction with no movement, or with movement only in the azimuth direction. The elevation and unwrapped data must all be in radar coordinates and all correspond to the selected GCP. ICESat data was used for the elevation information as it has a higher quality to the current RAMPv2 elevation data (the TanDEM-X does not cover a large area so cannot be used). The ICESat data is only acquired as a limited number of lines across the study area (Figure 2.2) so the GCPs can only be used at locations where this elevation is found. The GCPs must be distributed across range to correct the error in the perpendicular baseline, and must be found in connected areas of little or no movement so that the corresponding unwrapped phase has minimal displacement phase information included. Exposed rock has no movement and would be ideal, but the Skelton Glacier does not have exposed rock fitting the requirements, so areas with minimal movement along the ice divide between catchment basins was used.

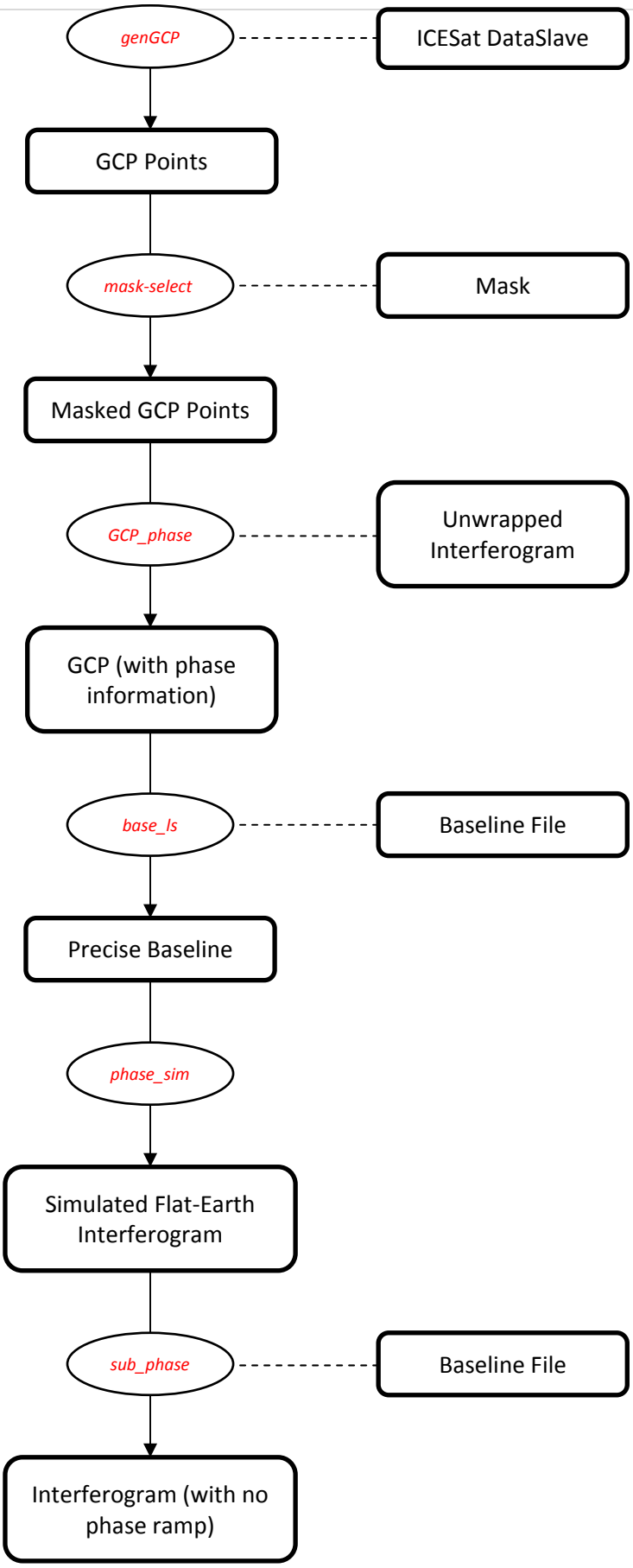

Figure 4.5: Flow chart showing the steps involved in refining the baseline and removing the observed phase ramp. The round boxes are the scripts and GAMMA programs that were used for processing.

An automated script (*genGCP*) *was* used to select GCPs over all of the ICESat data at spacings of 50 pixels apart. Another script (*mask-select*) was then used which took a mask (the area of little or no movement), and selected only the GCPs within that mask. Figure 4.6 shows an image of the study region in radar coordinates, with the created mask and GCP points that were used for one of the InSAR pairs. The output file is a text file with radar coordinates and elevation data for each GCP. The GAMMA tool *GCP_phase* takes this file and adds the corresponding unwrapped phase information to each GCP point. This file is put

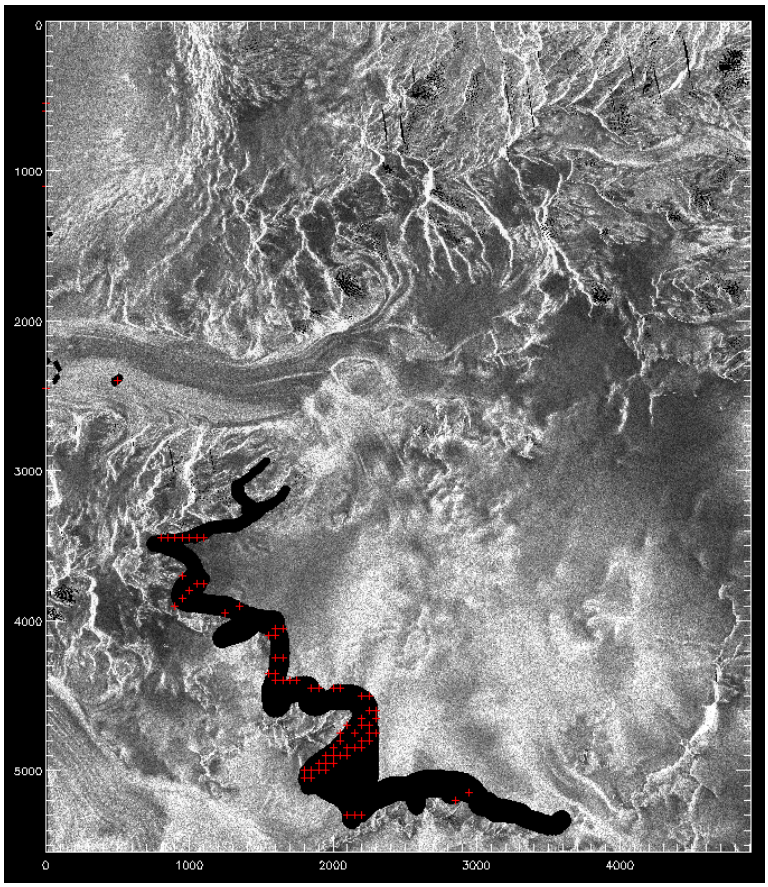

Figure 4.6: Location of the masked area along the assumed ice divide where there is little ice movement. The GCP points used for the baseline refinement are shown as red pluses.

through another GAMMA tool, *base_ls* which uses this information and the satellite geometry information to calculate the precision baseline.

This precision baseline is then used for further processing, but is also used to remove the phase ramp that is in the raw interferogram. This is done by using *phase_sim* to simulate a new unflattened interferogram using the new precision baseline. By flattening the original interferogram with this new

unflattened interferogram, a flattened interferogram with no observable phase ramp should be created (Figure 4.7).

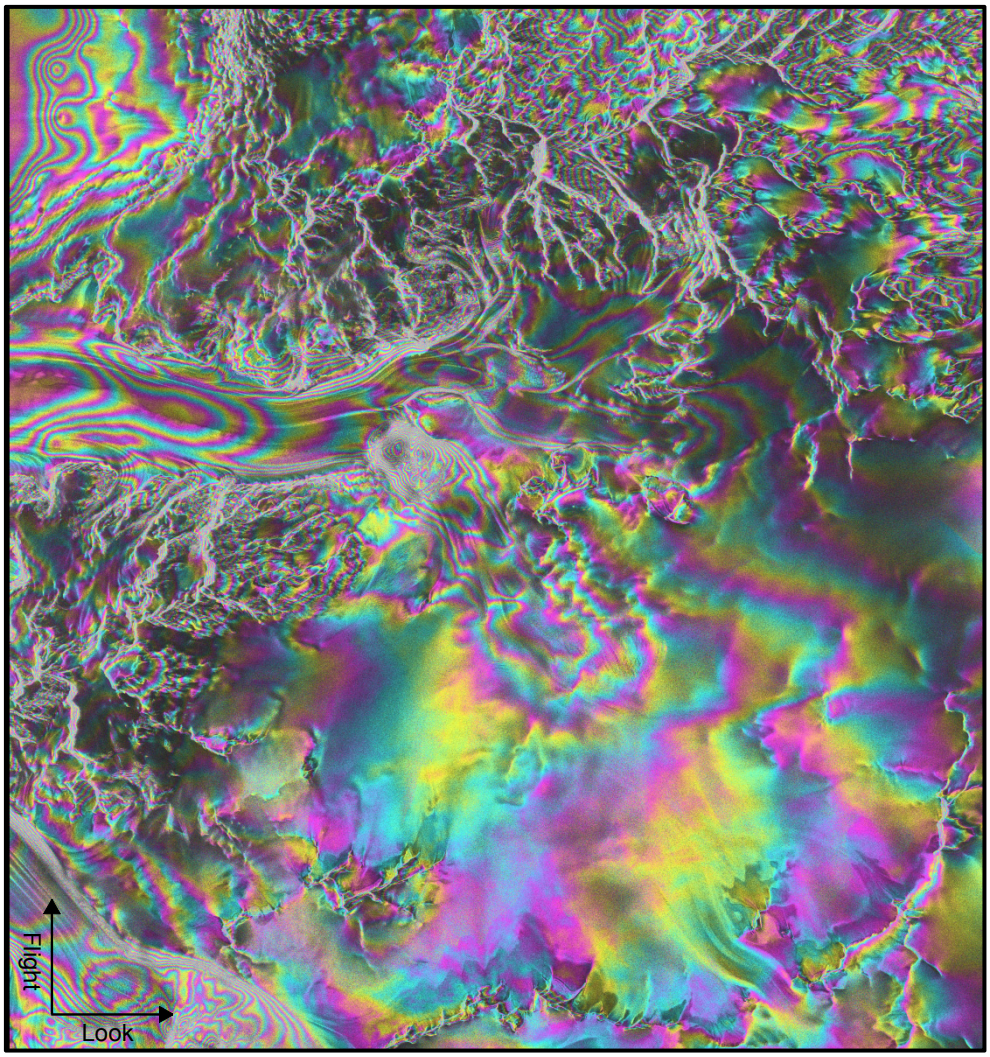

Figure 4.7: An image of the differential interferogram after the orbital phase ramp was removed. Figure 4.2 shows the interferogram with the phase ramp still present. Images are in radar coordinates.

Throughout processing, there is noise within the images which is seen as speckle. To remove this impact on the processing, filtering is done to smooth out the interferograms and remove much of this speckle. The GAMMA tool *adf* was used as a non-linear spectral filter to produces a smoothed interferogram and coherence image. These smoothed images reduced noise for further processing and help eliminate some of the possible future discontinuities.

Once the phase ramp has been removed from the raw interferogram, the processing steps from the raw interferogram to the unwrapped differential interferogram can be repeated, using the precision baseline when appropriate. The resulting unwrapped interferogram contains absolute phase data with no phase ramp and no topographic fringes.

4.5 – Displacement Map Generation

The unwrapped image still does not show displacement information, and must go through one more conversion. The GAMMA tool *dispmap* converts the unwrapped differential phase to a displacement map with real movement values (in metres per day). The displacement displayed in this map is only based on the displacement along the SAR look vector (see Figure 3.1 where the displacement is only in the slant range (R) direction). For glacier flow and further analysis, displacement along the look vector must be chosen instead of using the horizontal or vertical displacement components.

Another GAMMA tool (*dispmap_vec*) takes this a step further by using the previously produced displacement map, and using terrain information to produce a 3D displacement vector field. By assuming that glacier flow follows topography, flow direction and gradient can be acquired from a DEM. With the addition of the look direction and look elevation of the radar, a displacement vector field can be produced with displacement vector components in the easting, northing and vertical directions. Lower areas of the Skelton Glacier have very little gradient, which can result in inaccurate flow direction results with this process. To improve these areas ice flow data from an external source can be used as the flow direction instead of the implied gradient from the DEM. Inputting these directions offers more reliable flow information for the flatter regions of the glacier.

If two measured displacement fields are available and one is ascending and one is descending, then combining these can create a 3D displacement vector field giving real ground displacement (Joughin *et al.*, 1998). Having one ascending and one descending image is mandatory as the look direction of the two images preferably needs to be far apart (with 90° being ideal). This difference in look directions of the two images helps resolve the displacement into correct directions of flow. The GAMMA tool which does this is *dispmap_vec2*, and requires two displacement maps with corresponding information of each satellite, and a DEM with parameter file as inputs. This program

uses the assumption that motion is in the surface terrain plain. This technique is sensitive to motion in the SAR look direction only which means that in the perpendicular direction, errors will be much higher.

4.6 – Displacement Map Adjustment

The ice velocity field that is produced from the ascending and descending passes displays the ground movement of the ice, but may need to be adjusted to known ground data (Bürgmann *et. al.*, 2000). In the case of this research, the displacement map appeared to be overestimated when comparing to all the acquired GPS ground truth measurements. Adjustment needed to be done to alter the velocity values to the ground data, by choosing one GPS unit along the glacier as a tie point. The processing of the two different passes to create the vector field restricts the ability to simply add or subtract the image to fit to the GPS data. Instead, adjusting each pass individually before they are combined must be done. An IDL script (*3d-vel_v2*) was used to determine the amount each pass should be adjusted before being processed in *dispmap_vec2* (based on the equations found in Joughin (1998)). This script requires the satellite look information, and the velocity and bearing of the GPS unit which it is being adjusted to. The output is the value that the corresponding pixel of each image must be adjusted to produce the required value in the combined velocity map. This is done using the bandmath function in ENVI where a simple equation can adjust each pixel in the map by a specified amount.

4.7 – Surface Velocity of the Skelton Glacier

Once the displacement maps have been adjusted and put through the *dispmap_vec2* program again, an adjusted ice velocity map of the Skelton Glacier is produced which has been moved to fit the ground data. Figure 4.8 is a velocity map created from the combination of Tracks 455/456, where Track 455 is the ascending track, and Track 456 is the descending track.

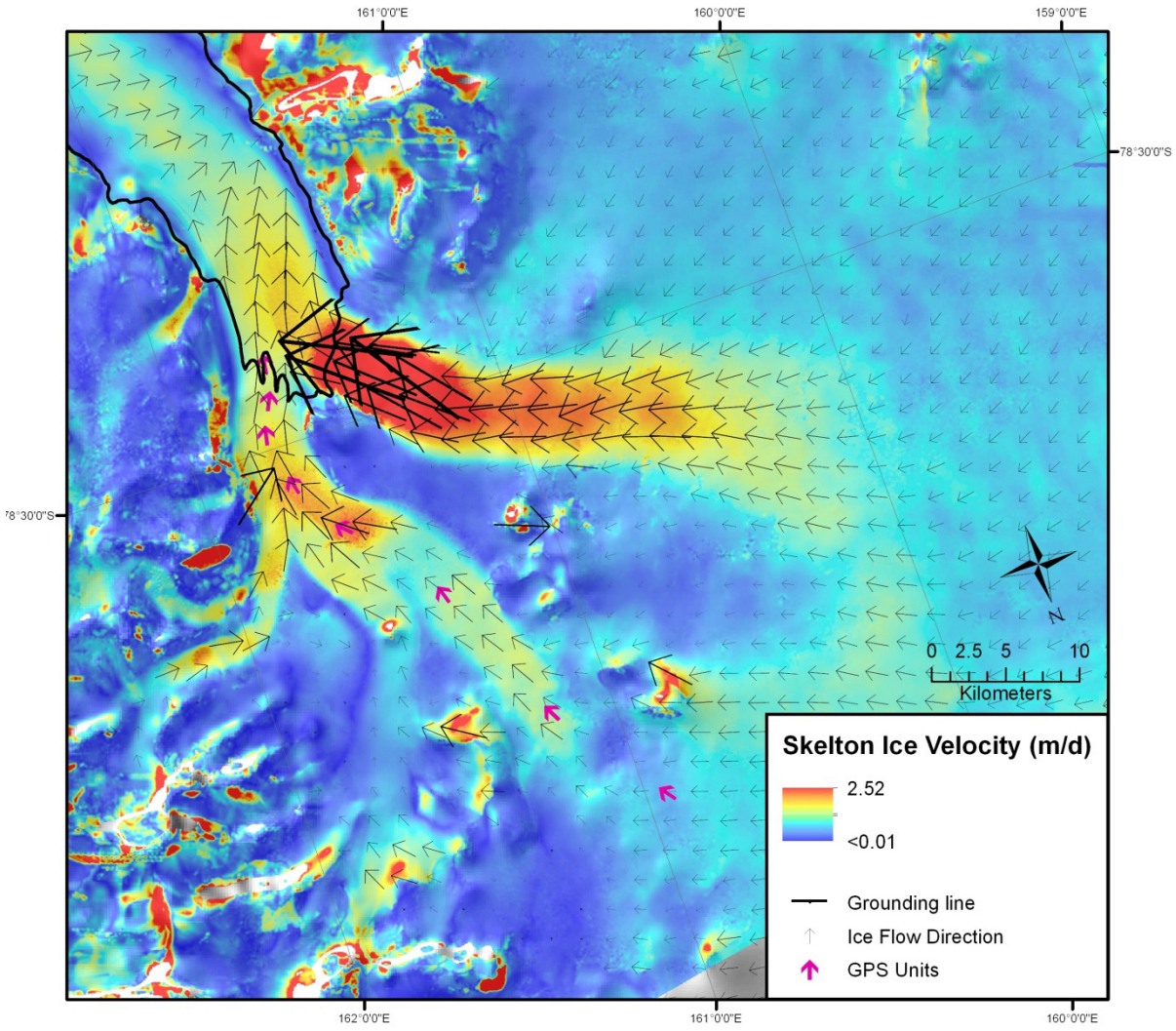

Figure 4.8: Ice Velocity Map of the Skelton Glacier in polar stereographic projection From track combination 455/456. Arrows show the ice flow direction at point spacing of 2km.

From the ice velocity map of the Skelton Glacier (Figure 4.8), the two glacier branches are visible by the higher ice velocity than the surrounding ice. The South Branch flows from the large area of flat ice in the upper catchment, while the North Branch flows from the numerous valleys and smaller glaciers which flow through the higher topography. The interferometric processing in these higher topography areas does not work well and can produce velocity magnitudes much larger than the surrounding glacier (i.e. up to 2.5m of movement per day). Flatter areas along the glacier and in the higher catchment zone show a more consistent velocity field. The ice velocity and flow directions below the grounding line on floating ice are unreliable and should be disregarded. This is because the floating ice in the fjord downstream of the grounding line has tidal influences which have affected the

processing in this area. Also, the generation of the velocity field assumes flow follows topography, which is heavily reliant on the quality of the DEM. The DEM in this location is mostly the lower quality RAMPv2 DEM, and is too flat for the flow direction to be accurately resolved. On the South Branch above the convergence of the two branches is the area of highest ice movement on the glacier. This is thought to be related to the changes in surface slope in this area due to the ice flow over a topographic barrier. At this point the stresses within the ice as it flows over this barrier have caused the ice stream to crevasse and break up. On the North Branch, the ice velocity is greatest in the lower part of the glacier above the convergence of the branches; however, it is less than half the velocity of the fast moving ice of the South Branch.

The difference between the processed ice velocity fields gives an indication of the level of uncertainties across the produced images, and identifies where the images match or do not match. Figure 4.9 shows the difference map between the two processed ice velocity fields (Track combination 141/455 and Track combination 455/456). The majority of the map is red which suggests that Track combination 455/456 has lower displacements than Track combination 141/455. Areas which had errors through processing produced higher differences between the velocity fields, which can be seen in areas of high topography, or the crevassed region of the South Branch. Where the higher resolution TanDEM-X was embedded in the RAMPv2 DEM, the difference appears to be minimal with velocities matching well. Locations with the lower resolution RAMPv2 DEM only, have larger differences between the two velocity maps.

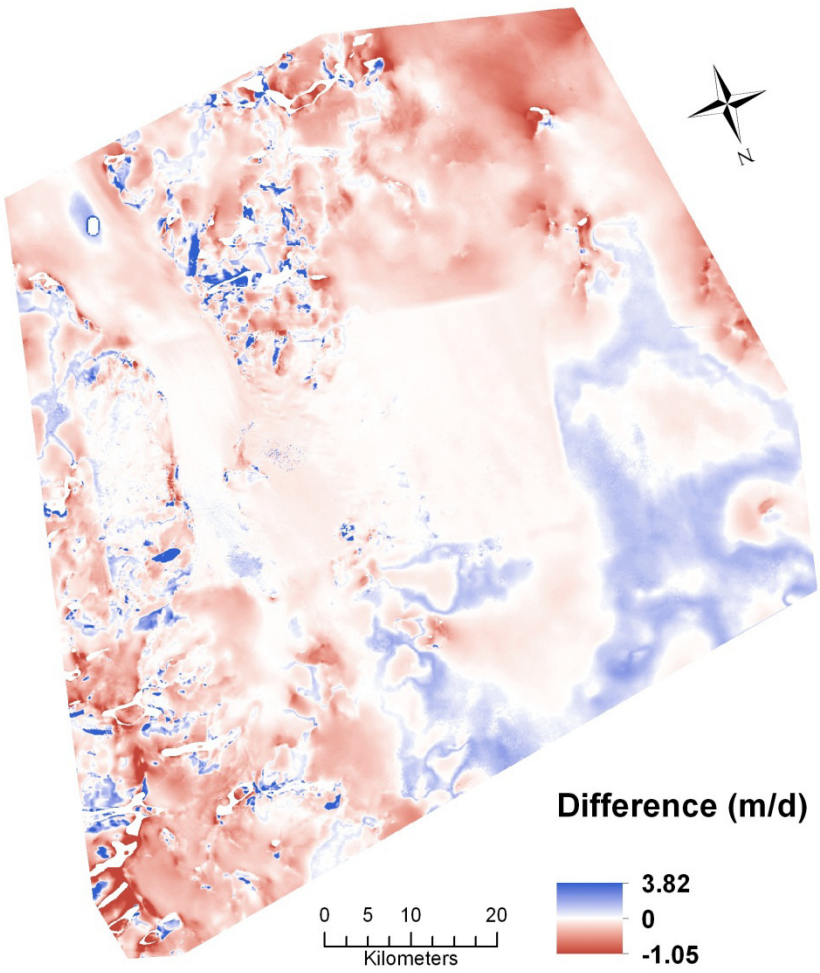

Figure 4.9: Difference map between the process image pairs. Red areas indicate areas where Tracks 455/456 has lower displacement than Tracks 141/455, while Blue areas indicate areas where Tracks 455/456 has higher displacement than Tracks 141/456. Image displayed in polar stereographic projection.

4.8 – Validation

To validate the created ice velocity field for the Skelton Glacier, it is compared to existing datasets and ground truth data. The GPS information that was gathered during the 2012/2013 summer is used as the ground truth data to compare the ice velocity fields. There are no previous high resolution ice velocity field studies for the Skelton Glacier to compare to, but a low resolution Antarctic-wide velocity map has been produced which covers the Skelton Glacier (Rignot *et al.*, 2011). This 'MEaSUREs' velocity map has a coarser resolution of 900m (Figure 4.10A). TerraSAR-X data being analysed in Gateway Antarctica gives another dataset created from a different technique to compare to, which has a resolution of 200m (Figure 4.10B). Table 4.1 shows the velocity data from the InSAR pairs, the average of the INSAR pairs, TerraSAR-X, MEaSUREs and the GPS measurements. It also shows the difference between the InSAR average velocities and each of these other datasets. The MEaSUREs and TerraSAR-X datasets appear to be underestimating the ice velocity; however, neither of these datasets have been adjusted to GCP's. Direct comparison of these velocities to the processed InSAR velocities cannot be done, but the general shape of the velocity profiles can be compared.

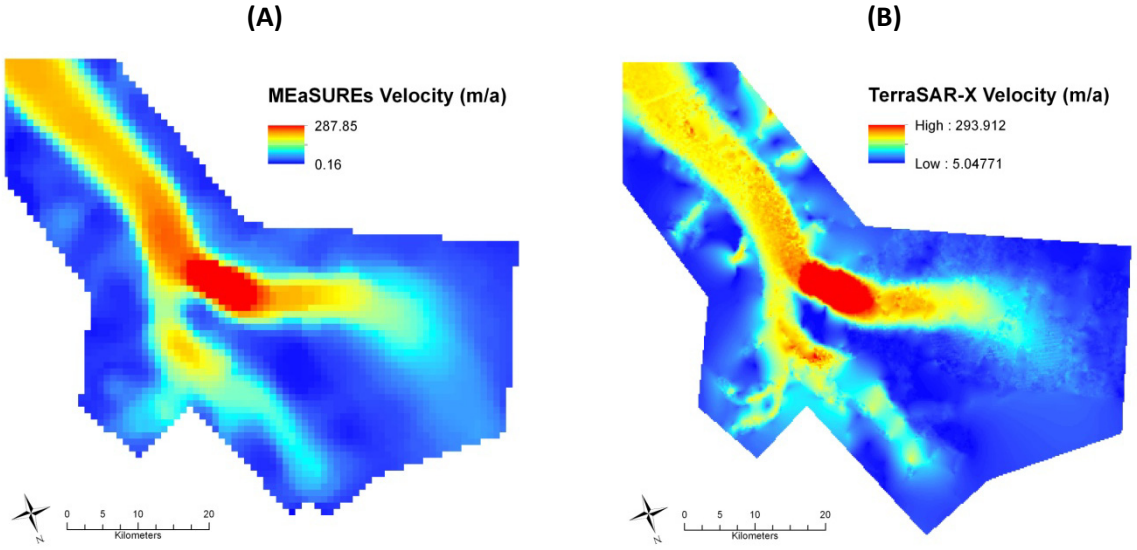

Figure 4.10: Ice velocity maps of the Skelton Glacier created from the (A) MEaSUREs velocity, which has a 900m resolution, and the (B) TerraSAR-X velocity which has a 200m resolution.

Table 4.1: Table comparing the processed InSAR velocities with the GPS measurements, the MEaSUREs velocities and TerraSAR-X velocities. The difference is the InSAR average velocities minus the GPS velocities, or other dataset velocities.

GPS Unit	Velocity (m/year)						Difference (m/year)		
	GPS	MEaSUREs	TerraSAR-X	InSAR (T141/T455)	InSAR (T455/T456)	InSAR (Average)	GPS	MEaSUREs	TerraSAR-X
GNS18	105.55	94.25	81.35	98.51	91.23	94.87	-10.68	0.62	13.52
GNS17	99.12	82.46	86.01	98.24	93.16	95.70	-3.42	13.24	9.69
GNS15	114.27	73.51	87.85	110.54	104.06	107.30	-6.97	33.79	19.45
GNS16	136.53	105.21	102.29	132.7	128.50	130.60	-5.93	25.39	28.31
ARC03	134.16	107.02	110.94	151.31	143.58	147.44	13.28	40.42	36.50
ARC05	63.56	62.92	50.32	105.89	71.93	88.91	25.35	25.99	38.59
ARC04	70.73	50.91	62.98	66.38	73.68	70.03	-0.70	19.12	7.05
ARC01	12.34	11.65	12.90	12.53	35.65	24.09	11.75	12.44	11.19

4.8.1 – Comparison with GPS measurements

The difference between the processed InSAR velocities and the GPS points are shown in Table 4.1. The averaged InSAR velocities of the two InSAR ice velocity maps were used for comparison, so that values are more representative. From the data, the difference of the GPS measurements and the average InSAR velocities varies depending on the location on the glacier. The lower four GPS comparisons (GNS18, GNS17, GNS15 and GNS16) all have greater GPS measurements than InSAR velocities, but are all within $11ma^{-1}$. The upper four GPS comparisons have larger differences and have a higher InSAR velocity than the GPS velocity, except for ARC04, which is the smallest difference of all the comparison points. The velocity difference divided by the original GPS measurement gives the percentage difference of InSAR compared to GPS. The average percentage is 21.2%. This includes ARC05 which gives a higher difference between the InSAR velocity and the GPS measurement, and ARC01 which has low velocity, so small velocity differences show higher percentages. Ignoring these two values brings the percentage difference down to 5.8%. Figure 4.11 shows a profile running along the North Branch of the glacier up the centreline of flow. This compares the InSAR data with the GPS units, the MEaSUREs, and the TerraSAR-X velocities. On this graph, the differences addressed above can be seen at each of the GPS units. GPS unit 'ARC05' is located approximately 28km along the profile, and is the comparison point which gives the greatest difference. The velocity from the InSAR track combination of 455/456 is similar to the GPS measurement, but track combination 141/455 is very high compared to other measurements (30-40m higher displacement per year). The lower four GPS units fit closely to the corresponding InSAR measurements, but the InSAR velocities on the upper glacier fluctuate and give values that are do not fit as well. InSAR velocities are also high at the highest GPS unit where velocities should be minimal.

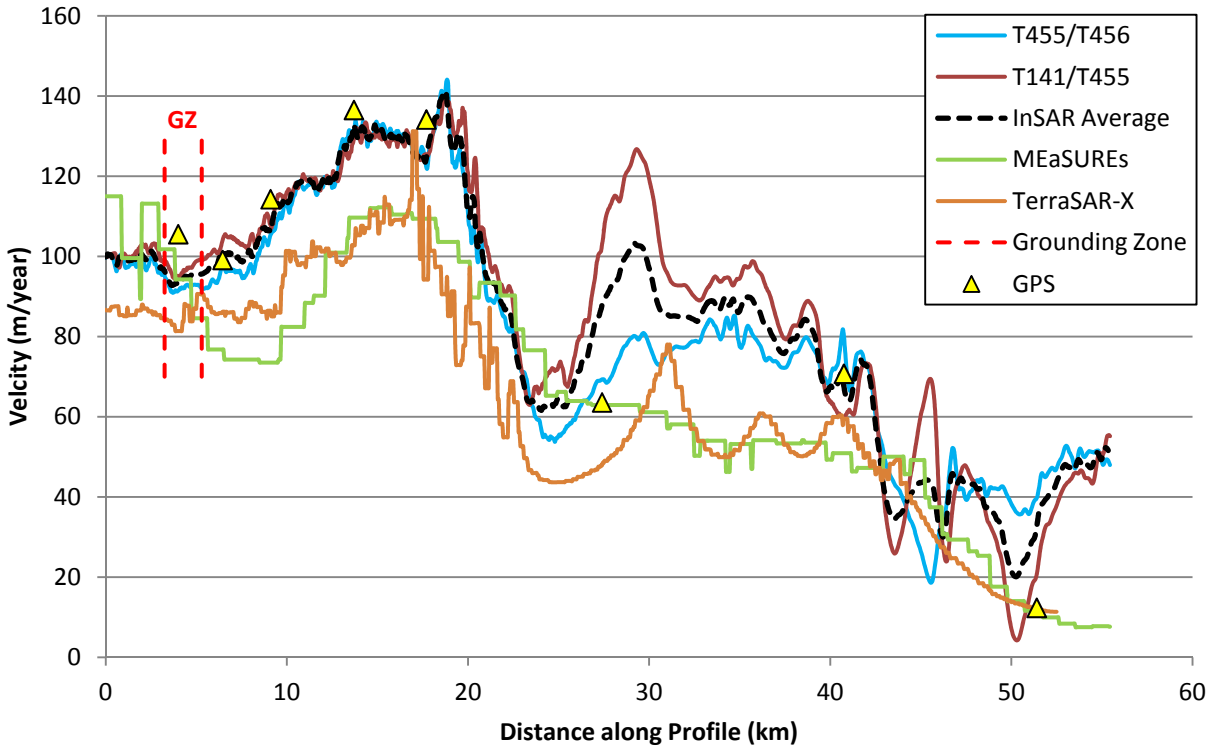

Figure 4.11: Graph showing InSAR, MEaSUREs and TerraSAR-X velocities against the GPS points along a profile up the North Branch of the Skelton Glacier. The precise location of the grounding line is unknown, so the area where the grounding line might be is shown. The profile follows the CReSIS flight path.

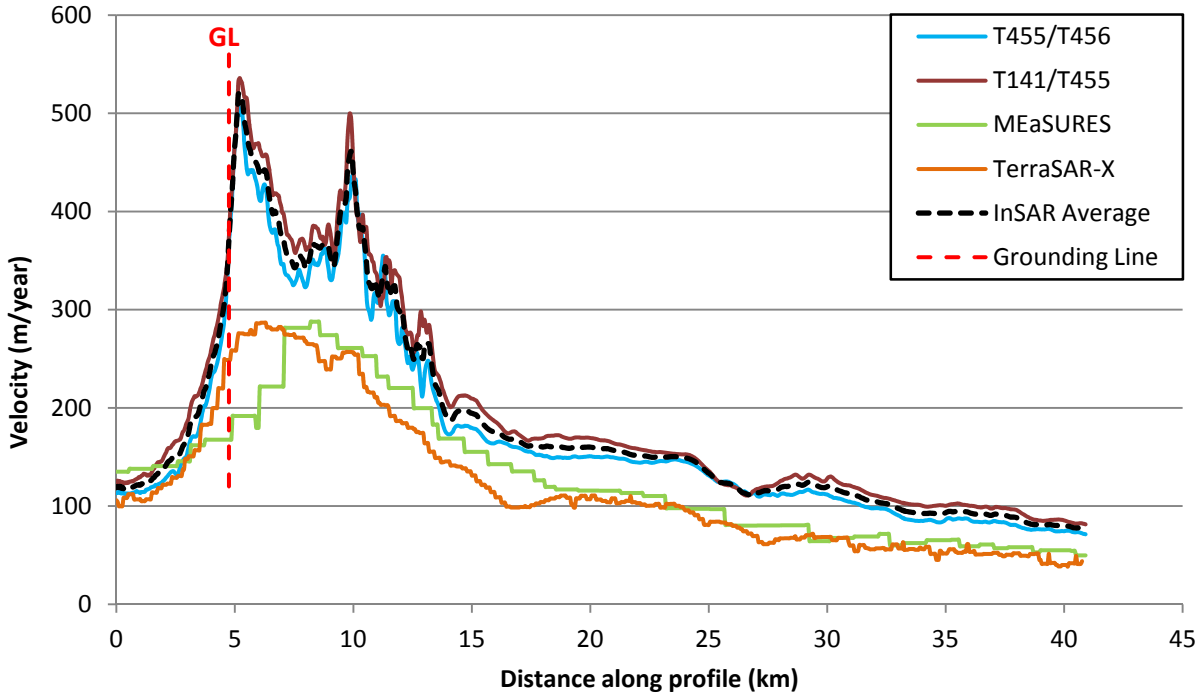

Figure 4.12: Graph showing the InSAR, MEaSUREs and TerraSAR-X velocities against the GPS points along second profile up the South Branch of the Skelton Glacier. The profile follows the CReSIS flight path.

4.8.2 – Comparison with MEaSUREs Velocities

In 2011, Rignot created the first Antarctic-wide velocity map. This was valuable for mass balance studies of Antarctica and provided information for all the ice sheets. The resolution is 900m, which means that results are only estimates and high resolution studies of all outlet glaciers and ice streams is still required for accurate mass balance estimates. However, it is a valuable guide to compare higher resolution data to, as the velocity field is similar to the velocity field created with the SAR data (Figure 4.10A).

The difference between the InSAR velocities and the MEaSUREs Velocities is shown in Figure 4.13. Most of the difference map is blue which indicates that the InSAR velocities are higher than the MEaSUREs velocities. The MEaSUREs velocities have not been adjusted to ground truth data, so this difference is expected (see Table 4.1 to see the differences between the velocities at the GPS unit locations). There is some red displayed on the map on the floating ice stream below the grounding line and on the edges of the grounded ice streams on the glacier branches, which indicates that the InSAR velocities are lower than the MEaSUREs Velocities. This can be seen at the very start of the two velocity profiles up the glacier arms (Figure 4.11 and Figure 4.12). The rest of the profiles give an account of how the measures velocity and InSAR velocities differ along the centre line of each glacier branch. In both figures, the shape of the velocity profile matches what the InSAR velocities display, as well as the GPS units, but lower for most of the profiles. Along the South Branch (Figure 4.12), the MEaSUREs velocities are much lower than the InSAR velocities in the faster moving area above where the glacier branches converge. The two InSAR velocity maps appear to match with each other especially well on this glacier arm, though at the fast moving section of the profile, the velocities are much higher than the MEaSUREs velocity (between 50 and 300m a year difference).

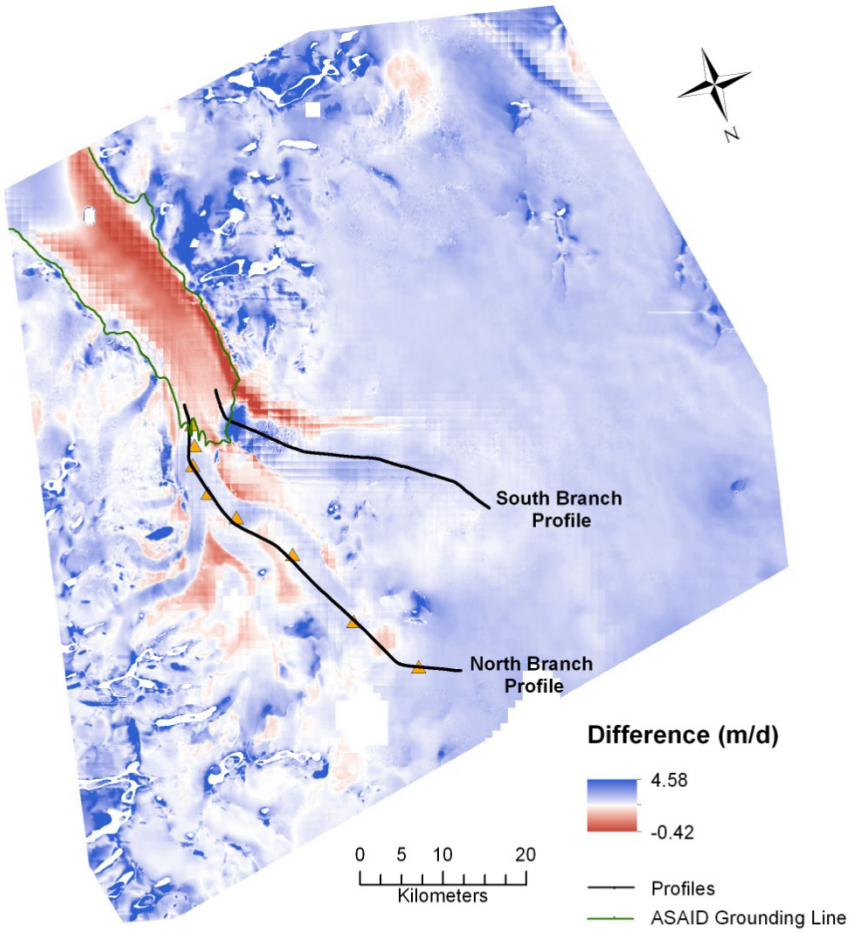

Figure 4.13: Difference map comparing the InSAR velocities of Track 455/456 with the MEaSUREs Velocities. The profile line used for Figure 4.10 is shown on this map as the black line.

4.8.3 – Comparison with TerraSAR-X Velocities

The TerraSAR-X velocity field was acquired from speckle tracking at a resolution of 200m. This dataset gives a different technique for calculating ice velocity on the outlet glaciers, and is valuable to use as a comparison with the InSAR velocities. Like the MEaSUREs velocities, the TerraSAR-X velocities have not been adjusted to ground truth data, so do appear to be underestimating the velocities compared with the InSAR data. This is why most of the map is blue in colour. The areas which appear red are similar to the red areas in the MEaSUREs velocities, which are around the edges of the grounded ice streams, and on the floating ice below the grounding line (except at the end of the floating ice stream away from the glacier). The velocity profiles up the two glacier arms shows the TerraSAR-X velocities to be lower than the InSAR velocities and the GPS measurements.

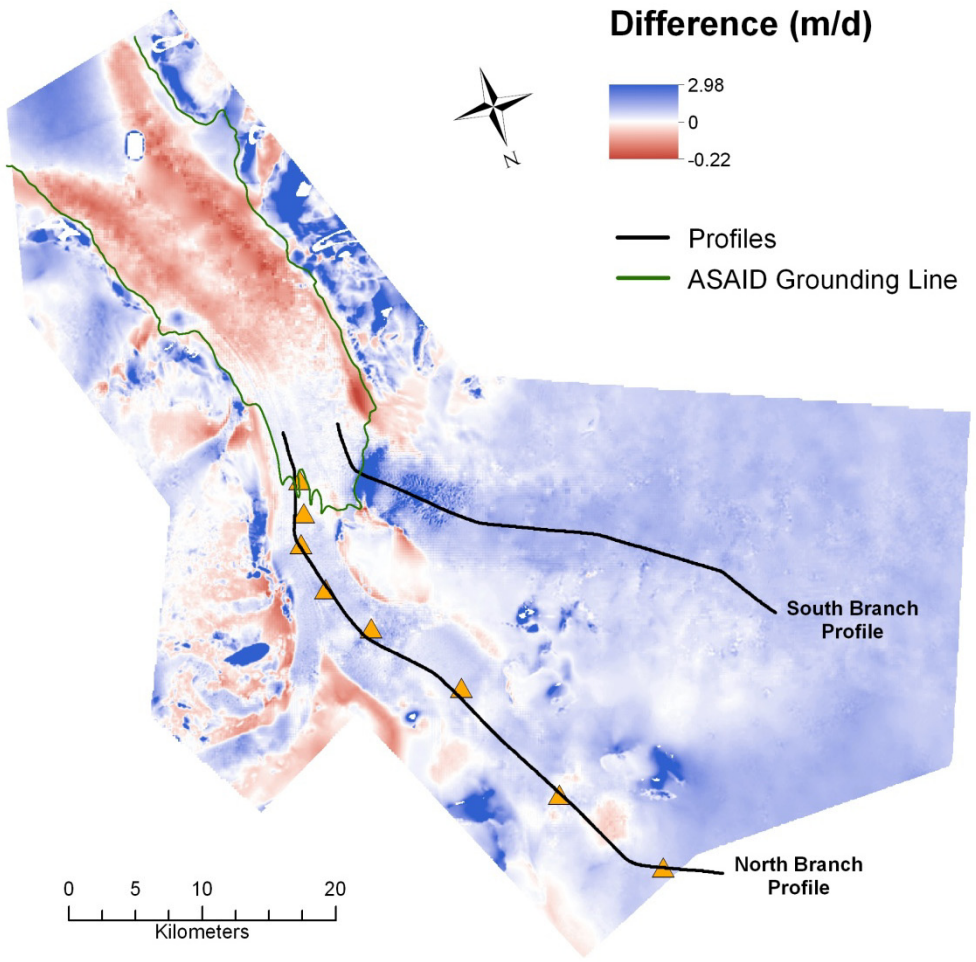

Figure 4.14: Difference map comparing the InSAR velocities of Track 455/456 with the TerraSAR-X Velocities. The profile line used for Figure 4.10 is shown on this map as the black line.

4.7.3 – Flow directions

It is also important to compare the flow direction of the ice as it demonstrates how well the processing resolves the direction from the displacement maps from an ascending and descending pass. The MEaSUREs velocity does not come with bearing directions as an attribute, so cannot be compared, but the TerraSAR-X and GPS units both have flow direction information. Table 4.2 shows the flow direction from the InSAR, GPS and TerraSAR-X data, and their differences. The difference between the InSAR flow directions and the GPS flow directions for the lower six GPS units are all within 10° of each other. The upper two comparisons are higher, at 15.75° and 40.75° difference. For the TerraSAR-X flow directions, the lower four GPS locations have less than 10° difference, with the four upper locations having much higher differences (16.70° - 57.90°). The higher GPS unit locations on the Skelton Glacier have lower velocities (especially ARC01) which tend to result in larger flow direction errors.

Table 4.2: Table comparing the flow directions of the InSAR velocity field with the flow directions of the GPS units and the TerraSAR-X data

GPS Unit	GPS Flow Direction	InSAR Flow Direction	TerraSAR-X Flow Directions	GPS Difference	TerraSAR-X Difference
GNS18	-10.73	-2.00	-3.40	8.73	1.40
GNS17	6.88	8.90	6.50	2.02	2.40
GNS15	-6.83	-7.70	-0.04	-0.87	-7.66
GNS16	-33.04	-31.40	-34.70	1.64	3.30
ARC03	-64.29	-71.60	-54.90	-7.31	-16.70
ARC05	-36.32	-46.00	-26.20	-9.68	-19.80
ARC04	-46.55	-62.30	-20.20	-15.75	-42.10
ARC01	-55.85	-96.60	-38.70	-40.75	-57.90

5 – Ice Flux and Mass Balance of the Skelton Catchment

Using Interferometric SAR Processing, ERS SAR data has been processed into a surface velocity map of the Skelton Glacier. The velocity magnitude and flow directions have been compared with ground truth measurements and other available datasets for validation. This velocity map is now used for the next step of this study, along with ice thickness up the glacier centreline, to determine the ice flux through consecutive flux gates. Comparing these mass flux values with accumulation data for the Skelton Glacier in the catchment zone gives mass balance estimates and allows an estimation of the associated errors.

5.1 – Flux Gate Information

Ice flux can be estimated by multiplying the velocity of ice flowing through a cross-section by the area of the cross section and by the ice density. After integration over the glacier width the total mass flux value can then be compared with the upstream accumulation in the catchment zone to determine a mass balance estimate for that particular flux gate. For the Skelton Glacier, ten flux gates were chosen as cross-sections for mass flux and mass balance estimates. This consists of five flux gates on each branch of the grounded section of the glacier (see Figure 5.1). The locations chosen for the flux gates give a good distribution along the lower extent of the grounded ice on the glacier, especially near the grounding line. Further up the glacier, the faster flowing ice is less constrained by topography and it becomes more difficult to do flux gate calculations.

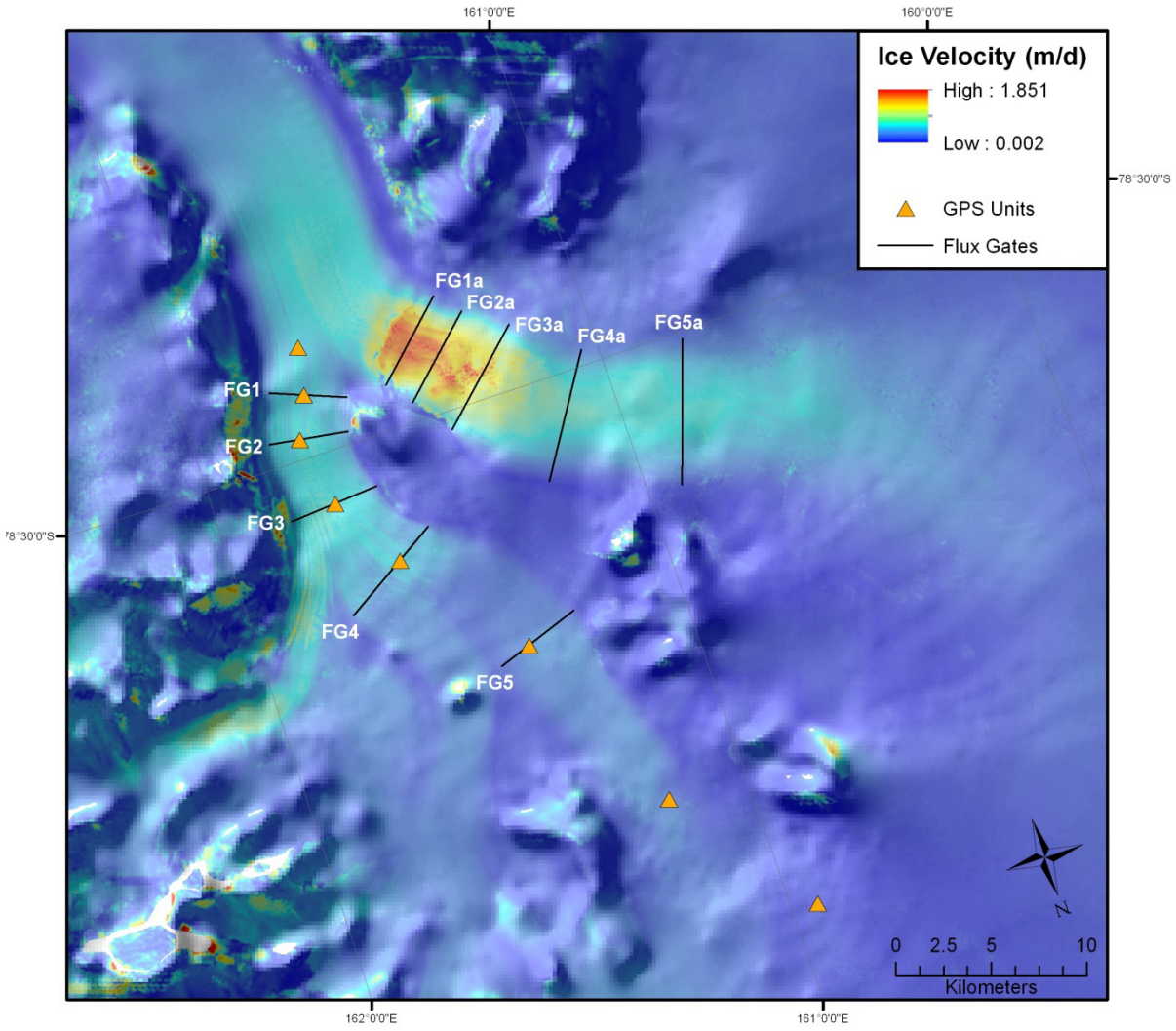

Figure 5.1: Map of the Skelton Glacier showing the location of the flux gates along the two glacier arms. The background image is a hillshade image of the RAMPv2 DEM, with the ice velocity map of Track 455/456 overlaid to show the ice flow boundaries in relation to the flux gates. Image is displayed in polar stereographic.

5.1.1 – Cross-Sectional Area

In order to determine the total mass flux, the flux gate area needs to be known. Because the ice thickness was only measured along the centreline of the glacier, simplistic assumptions were used to reconstruct the shape of the glacier bed. By comparison with other glaciers with similar geomorphological characteristics and examining the shape of the velocity cross-profiles on the glacier (see Chapter 5.1.2 for further explanation) the shape of the glacier is assumed to be parabolic (Paterson & Cuffey, 2010). With this assumption, determining the cross-sectional area (A) of a flux gate is calculated by:

$$A = \frac{2}{3}wt \tag{5.1}$$

where w is the width of the flux gate, and t is the thickness at the centreline of the glacier (Figure 5.2).

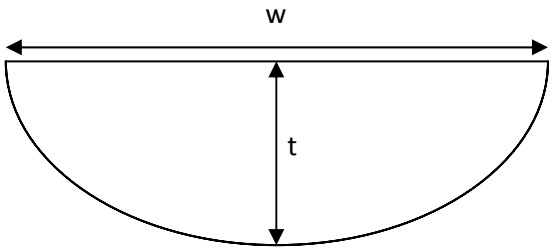

Figure 5.2: Diagram of the parabolic cross-section that is assumed for the glacier shape.

The ice thickness data was obtained from airborne radar surveys done by the Center for Remote Sensing of Ice Sheets (CReSIS) during a flyover of the Skelton Glacier in the Summer 2011/12 season. It is a line of measurements along each arm of the glacier close to the centreline. The surface velocity profiles of the flux gates validate the use of a parabolic shape for the cross-section by their velocity distribution (Figure 5.3). The thickness profile is thought to be of similar parabolic shape to the velocity profile, which suggests that the thickest ice is along the centreline while the ice towards the margins is shallower. The slower moving ice near the margins is more affected by the basal shear stresses or resisting stresses from the side walls.

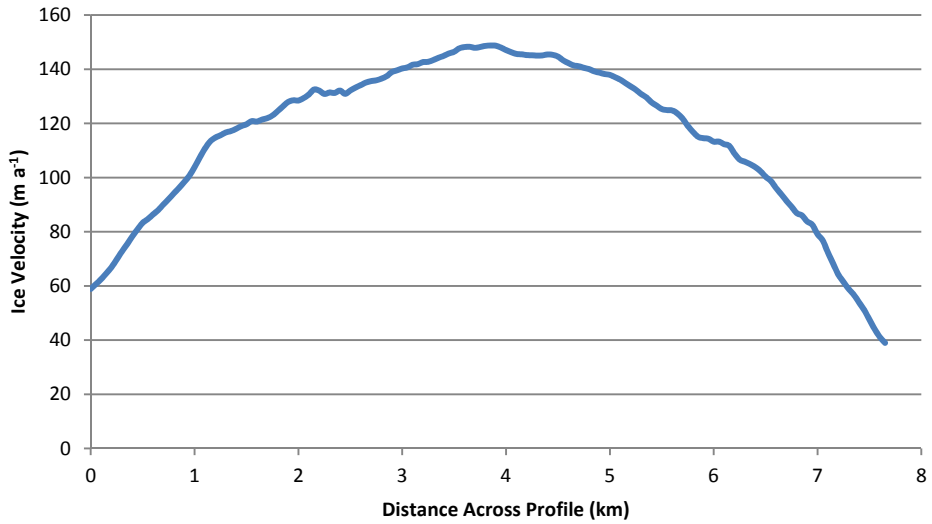

Figure 5.3: Example of one of the cross-section velocity profiles showing lower velocities near the edges of the ice stream, and higher velocities near the centreline. This example is taken from flux gate 5a (cross-section velocity profiles of other flux gates are in Appendix).

5.1.2 – Depth Averaged Ice Velocity at a Flux Gate

The mean ice velocity at a cross-section needs to take into account a vertical ice velocity profile from the fast moving surface down to the slowing moving ice near the bedrock. Assuming the horizontal surface velocity down to the bottom does not take into account the frictional forces acting on the moving ice from the valley bed and sides, the basal shear stress (τ_b) can be calculated from:

$$\tau_b = F\rho g h \sin\alpha \tag{5.2}$$

where F is the shape factor (Paterson & Cuffey, 2010), ρ is the density of the ice (kg/m^3), g is the acceleration due to gravity (9.81ms^{-1}), h is the depth ice thickness (m), and α is the slope of the glacier at the flux gate (degrees from horizontal). The shape factor takes into account the support from valley walls, which in turn reduces the basal shear stresses acting on the ice. The ice deformation velocity (u_{def}) can then be calculated from (Paterson & Cuffey, 2010):

$$u_{def} = \left(\frac{2A}{n+1}\right) \cdot \tau_b^n h \tag{5.3}$$

where 2A is a constant (1.36x10^{-23}), n is also a constant (assumed to be 3; however, other values have been used in research (Chandler *et al.*, 2008)), and h is the depth over which the deformational velocity is being calculated (m). Assuming uniformity of the glacier slope, bed topography and internal deformation, the shear stress distribution and velocity profile can be determined for a glacier

using equations (5.2) and (5.3) where these assumptions hold true. However, these factors are generally not uniform for real world glaciers, and as a result difficult to apply for all situations (Hooke, 2005). For the Skelton Glacier, many of these factors including bed topography are complex and currently unknown. Basal conditions have not been studied closely, but the velocity field that has been created indicates areas of complex bed topography (e.g. a topographic barrier near the grounding line on the Southern Branch, or at locations where two smaller ice streams converge into one). Other studies used a simple ratio between the depth-averaged velocity and the surface velocity in the range of 0.85 to 0.92 (Fricker *et al.*, 2000). For this research, a value of 0.9 has been used as an assumption when determining the mass flux through the flux gates on Skelton Glacier. This decreases the surface velocity values by 10% and in this way taking into account the basal shear stress in this region.

The total mass flux MF is derived in this study by summing up a number of n ice fluxes across glacier by using:

$$MF = \sum_{i=0}^{n} v_i h_i x_i \rho \tag{5.4}$$

where v_i, h_i, and x_i is the depth averaged velocity, thickness, and width of individual segments, respectively. The segment width was chosen with x=100m in this study, and ice density was chosen with ρ=917kgm^{-3}.

5.1.3 – Skelton Catchment Area

To calculate accumulation for input to the flux gates, the catchment area must be estimated. As there is no literature or studies defining the catchment area of the Skelton Glacier, it had to be estimated from visual analysis of local DEM's, hill-shade maps and velocity maps. The Skelton Catchment area is estimated here to be approximately 6,569km^2. This is small compared to some of the other larger catchment areas for TAM outlet glacier, which can be over 50,000km^2 (the neighbouring Mulock Glacier has a catchment area of approximately 123,925km^2 (Stearns, 2011). The overall catchment area of the Skelton Glacier is generally well defined, although errors in the catchment boundaries are possible on the relatively flat ice sheet at high elevations. This will result in only small accumulation errors because the snow accumulation in these areas is relatively small. The upper catchment boundary extends past the Van Allen Range into the flat interior of the EAIS, as it is assumed a small amount of the ice here flows into the lower catchment area and down the Skelton Glacier (Figure 2.1).

5.2 – Mass Balance

The mass flux (or ice discharge) through the flux gate is the volume of ice moving through the cross section within a given time period. When this is compared with the amount of accumulation in the catchment zone above the flux gate, the mass balance can be estimated for that cross-profile. Table 5.1 shows the mass flux through each flux gate, accumulation in the catchment area for each flux gate from the two different accumulation datasets and mass balance calculations for the ten flux gates on the two branches of the Skelton Glacier. The mass balance, as expressed as a percentage was also included for the mass balance from each of the two accumulation datasets.

Table 5.1: Accumulation, mass flux and total absolute mass balance estimates for the ten flux gates on the North and South branches of the Skelton Glacier. The relative mass balance (%) was also included for ease of interpretation. Units are in Gt a^{-1}.

Flux Gates	Accumulation		Mass Flux	Mass Balance		Mean Mass Balance (%)	
	AMSR	IMAU		AMSR	IMAU	AMSR	IMAU
FG1	0.4354	0.4848	0.3243	0.1111	0.1605	34%	50%
FG2	0.4332	0.4825	0.4398	-0.0066	0.0426	-2%	10%
FG3	0.4280	0.4764	0.3787	0.0493	0.0977	13%	26%
FG4	0.3583	0.3896	0.2972	0.0611	0.0924	21%	31%
FG5	0.2331	0.2095	0.1603	0.0728	0.0492	45%	31%
FG1a	0.6975	0.6135	0.8922	-0.1947	-0.2788	-22%	-31%
FG2a	0.6871	0.5990	0.6170	0.0700	-0.0180	11%	-3%
FG3a	0.6301	0.5327	0.4835	0.1466	0.0492	30%	10%
FG4a	0.5956	0.4937	0.6367	-0.0411	-0.1430	-6%	-22%
FG5a	0.5586	0.4569	0.5952	-0.0367	-0.1384	-6%	-23%
FG1+1a	1.1329	1.0982	1.2165	-0.0836	-0.1183	-7%	-10%
FG2+2a	1.1203	1.0815	1.0569	0.0634	0.0247	6%	2%
FG3+3a	1.0581	1.0091	0.8622	0.1959	0.1469	23%	17%

Flux Gates 1 and 1a are located lower down the glaciers than the rest of the flux gates. As a result, these flux gates have higher accumulation values due to the larger catchment area. The further up the glacier the flux gate is located the small the catchment area and accumulation. This is the same as the mass flux estimates which mostly decrease up the glacier. The upper glacier flux gates are located where the ice thickness is smaller, the ice velocity is slower and flowing ice stream is less constrained, which all result in the small mass flux through these flux gates (this is more prominent on the North

Branch). The lower flux gates on the South Branch are in the complex zone around the grounding line which has a much higher velocity than the rest of the glacier. The ice also flows over a topographic barrier which has led to fracturing on the ice sheet. The mass balance estimates for this area fluctuate between

-0.2788 Gt a^{-1} and 0.1466 Gt a^{-1} depending on the accumulation dataset used. The smaller Northern Branch has all but one mass balance estimate positive, with estimates from the two accumulation datasets agreeing on this point. The larger Southern Branch does not have an obvious pattern and has a combination of negative and positive mass balance estimates. The flux gate combination nearest but upstream of the grounding line is the best location to use when determining the mass balance of the whole glacier (Rignot & Thomas, 2002). The flux gate combination of FG1 and FG1a is located in this region, and gives mass balance estimates of -0.0836 Gt a^{-1} and -0.1183 Gt a^{-1} for the two accumulation datasets. This appears to be mostly due to the Southern Branch flux gate having very high velocities, which result in a large mass flux value. These flux gates might be close or above the grounding line, which could give inaccurate results. The next flux gate combination upstream (FG2 and FG2a) is most likely above the grounding line location, and give mass balance estimates of 0.0634 Gt a^{-1} and 0.0247 Gt a^{-1}. These two estimates are both relatively small mass balances, and are closer to a state of mass balance equilibrium than FG1/FG1a. Flux gate combination of FG3 and FG3a gives higher positive mass balance estimates with 0.1959 Gt a^{-1} and 0.1469 Gt a^{-1}.

6 - Interpretation of Results

ERS SAR data from 1996 has been used in conjunction with newer auxiliary data to create a high resolution ice velocity field for the Skelton Glacier. This has then been used to estimate the mass flux of the glacier at specific cross-sections. Comparing discharge with accumulation data allows for mass balance measurements to be estimated, by way of the mass budget method. By using this budget method for a smaller catchment basin such as Skelton Glacier, mass balance measurements can be found to a high precision. There are many of these smaller catchment basins in the TAM which need to be researched with high resolution data so that complete mass balance measurements for the EAIS can be calculated. Investigating older data for these glaciers is still applicable as mass balances can change for these glaciers over this time period, as have been observed by studies in the area (Stearns, 2011).

6.1 - Ice Velocity

The ice velocity map of the Skelton Glacier produced in this study was obtained using the image processing technique of Interferometry. The ERS SAR data is approximately 17 years old, but with new auxiliary data used in the processing, a high resolution velocity field of the Skelton Glacier was produced. Despite the age of the data and the limitations relating to the satellite's configuration and geometry, the velocity field compared well with ground truth data from *in situ* GPS units. The velocity pattern across the glacier also matches a previous lower resolution velocity field that covers the area (Rignot *et al.*, 2011), where the faster flowing ice streams and smaller glaciers that feed into the main glacier can be clearly seen. In these areas, the glacier slope is found to increase, and there are higher amounts of ice discharge. On the Southern Branch of the Skelton Glacier above the grounding line, the ice velocity is much higher than observed across the rest of the glacier. Airborne ice thickness surveys have found that there is a topographic barrier under the ice at this location which affects how the ice stream behaves. With the force of ice pushing behind this region, the glacier stream flows over this topographic barrier at higher speeds than elsewhere. With the thinning of the ice and the stresses caused by this increased flow, crevasses have formed on the top of the ice and are visible in optical imagery (Vaughan, 1993).

Below the grounding line in this Southern Branch, the velocity decreases rapidly. SAR Interferometry is a useful technique to obtain the grounding zone location because it is very sensitive to vertical displacement due to the tidal flexure (Neckel *et al.*, 2012). Due to the high sensitivity to vertical motion in an interferogram (see Chapter 3.4), a close sequence of tidal fringes can be observed within about 5-10 ice thicknesses of the grounding line (Rignot, 2002). In Figure 4.2C, tidal fringes can be observed on the coast of the TAM where the mountains meet the Ross Ice Shelf, but no obvious tidal

fringes can be observed up the fjord where the Skelton Glacier is floating. This is because the ice is stabilised by the side walls of the relatively narrow fjord. The fjord has a small width of approximately 10km (about 10 ice thicknesses), which likely dampens the effect of tides throughout this area. As a result, the tidal fringes that would be expected are mixed in with the velocity fringes up the whole fjord. To backup this claim, Antarctic Surface Accumulation and Ice Discharge (ASAID) have estimated where the grounding line and hydrostatic line for this area are, where the grounding line is the location where ice begins to float, and the hydrostatic line is where the floating ice is not influenced by the grounding of ice anymore (Brunt *et al.*, 2010). Between these lines, there would be tidal flexure. The hydrostatic line near the Skelton Glacier is observed to be near the mouth of the fjord, meaning most of the ice in the fjord is not freely floating.

The position of the grounding line on the Northern Branch is unclear. The ASAID grounding line is assumed to be near the lowest GPS unit (GNS18) while the MODIS grounding line is assumed to be higher up the glacier near GPS units GNS17 and GNS16. Unlike the Southern Branch, the ice velocity on the glacier does not clearly indicate where the grounding line might be located. The ice thickness is deepest near GNS16 and then thins closer to the assumed ASAID grounding line. The ice thickness profile suggests the grounding line is closest to GNS15 (see radar profile in Appendix).

The highest surface velocities are observed in areas of high or steep bed topography around the Skelton Glacier. These areas also show higher variation in velocity magnitudes, with values reaching over 500ma^{-1}. Velocities in flatter areas are in general much lower. Large velocity gradients in fast flowing areas may cause problems in the phase unwrapping during the interferometric processing especially in areas with steep topography. In the SAR image, areas with steep topography are recorded as layovers or even shadows, which result in low coherence. When processed, these areas of low coherence create phase discontinuities and errors which propagate throughout the processing (Bürgmann *et al.*, 2000). Other than areas such as this, the settings chosen for the processing of the Skelton glacier yielded largely reliable results.

While the velocity of the grounded glacier changes significantly across the area, the velocity of the glacier below the grounding line where the two branches converge is more uniform, at about approximately 102ma^{-1}. There are only a few previous studies which estimate the velocity for the Skelton Glacier, but from them, the velocity values match closely with this satellite analysis. In the 1958-1959 Victoria Land Traverse, the Skelton Glacier was investigated to have an average velocity of 0.24 md^{-1} or 88.7 ma^{-1} between Teall Island and Fishtail Point, slightly outside the boundaries of the satellite frames that were used for this study (Wilson & Crary, 1961). At the time these measurements were calculated, the grounding line was assumed to be at the location that was being surveyed. Alternatively, (Cameron & Goldthwait, 1961) estimates the ice velocity of the Skelton Glacier to be 0.28 md^{-1} or 102.2 ma^{-1}, though does not specify where this value is taken from. This

second estimate very closely matches the estimate for the Skelton Glacier from ERS InSAR data. A more recent study (Humbert *et al.*, 2005) has estimated the ice velocity at the grounding line (same location that it is assumed to be at present) to be 350 ma^{-1}. It is not clear the precise location, but judging by the much higher velocity estimates, it is assumed to have estimated for the South Branch where velocities are high. This value matches the velocities at the grounding line on the South Branch relatively well, although there are large variations in the InSAR velocities which go higher than a velocity estimate of 350 ma^{-1}.

6.2 - Mass Balance

Comparing accumulation data with ice flux for various flux gates on a glacier gives mass balance estimates. This can show the state a glacier is in or which areas will change most in the future. For the Skelton Glacier analysed in this study, ten flux gates were chosen (five located on each branch). Two accumulation datasets were used so that a comparison could be done between different methods of accumulation estimation. Table 5.1 shows the mass balance estimates for the flux gates along the Skelton Glacier. The flux gates do not all indicate either a positive mass balance, or negative mass balance, but patterns can be seen when looking at where the flux gates are, or what branch they are on. From both accumulation datasets, the North Branch mostly gives positive mass balance values for the flux gates. The South Branch has a mixture of positive and negative mass balance values, especially for the IMAU accumulation model. The easiest location to provide a mass balance estimate for an outlet glacier is near the grounding line downstream enough so that tidal influence is minimal or non-existent (i.e. near the hydrostatic line) (Rignot & Thomas, 2002). As addressed above, for the Skelton Glacier this is near the end of the glacier stream where the glacier enters the Ross Ice Shelf, and is not covered by the acquired ERS SAR data. Near the grounding line on grounded ice provides a more accurate estimate of peak ice discharge and is what has been focussed upon for this study. A mass balance of Flux Gate 1 and Flux Gate 1a gives an average value of -0.1101 Gt a^{-1} between the two accumulation datasets. The very high velocity of the South Branch flux gate is the biggest factor relating to why this is a negative mass balance. The next two pairs of flux gates up the two branches give increasingly more positive mass balance values with estimations of 0.0159 Gt a^{-1} and 0.1519 Gt a^{-1} respectively. The large velocities of the South Branch decrease from the lowest flux gate up the glacier, which gives rise to lower ice discharge values and hence higher mass balance estimates.

The mass balance estimates are still relatively small in terms of the amount of ice lost or gained over a year, and fit within the estimates for the TAM and the EAIS. Mass balance estimates for the EAIS are wide ranging depending on the techniques and areas observed, and usually have very high uncertainties, sometimes larger than the mass balance estimate itself. The most current Intergovernmental Panel on Climate Change (IPCC) report estimates the mass balance of the EAIS to

be 20 ± 21 Gt a^{-1} (IPCC, 2007), which some other estimates have been put at 22 ± 23 km^3 a^{-1} (Rignot & Thomas, 2002), 26 ± 36 Gt a^{-1} (Shepherd *et al.*, 2012) and 0 ± 56 km^3 a^{-1} (Velicogna & Wahr, 2006). The nearby Mulock Glacier (to the South of the Skelton Glacier) has an estimated mass balance of 0.9 Gt a^{-1} (Rignot & Thomas, 2002). The Skelton Glacier has a much smaller catchment area, and flowing ice streams than the Mulock, and hence the smaller estimate for the mass balance.

The mass flux of the Skelton Glacier has also been found at two flux gates located ~1km and 5km downstream of the grounding line on floating ice. 1km downstream, the mass flux is estimated to be 1.145 Gt a^{-1}, and 5km downstream the mass flux is 0.912 Gt a^{-1} (pers. Comm. O. Marsh, 2013). These values fit well with the estimated mass flux near the grounding line of 1.2165 Gt a^{-1} which should be higher as there is no basal melting occurring at this location. Humbert et. al. (Humbert *et al.*, 2005) also estimated the mass flux at the grounding line in to be 1.2288 Gt a^{-1} which closely matches the value estimated for this research too. This is a difference of 0.0123 Gt a^{-1} (or a 1% difference).

6.3 – Sources of Uncertainty

In order to estimate the overall uncertainty of the mass balance measurement, an error analysis using the estimated uncertainties from the different sources was performed. For this the calculation of the total mass balance (MB) was simplified to:

$$MB = v \cdot A \cdot c - Acc \tag{6.1}$$

where v is the averaged surface velocity, A is the cross section, Acc is the accumulation. The constant factor c = 0.9x0.917 is the sliding factor times the density of ice. Assuming independent and random errors the mean mass balance error ($\bar{m}_{MB}$) calculates by the law of error propagation to (Drosg, 2009):

$$\bar{m}_{MB} = \sqrt{(c \cdot \bar{m}_A \cdot v)^2 + (c \cdot \bar{m}_V \cdot A)^2 + {\bar{m}_{Acc}}^2} \tag{6.2}$$

with $\bar{m}_{A/V/Acc}$ as the mean estimated errors of the flux gate area, the velocity, and the accumulation measurement, respectively. This error analysis assumes that there are no errors in the ice density and the sliding factor. The three propagating errors in the above equation are from the area of the cross section, the ice velocity and the accumulation. Due to limitations of input data, the assumptions that have had to be made, and other small errors in the processing of data, these errors need to be quantified.

The accumulation errors come from two different factors, which are the accumulation datasets and the difference that is observed between them, and the catchment area used to determine the accumulation

value for the Skelton Glacier. The two datasets are obtained from different methods, and both give an accumulation map with a resolution much coarser than the other data that is being used for the mass balance estimates (>25km resolution). Also, the two accumulation datasets have varying estimates at different locations around the TAM, including over the Skelton Glacier (Figure 2.4). The catchment basin area has only been estimated from looking at DEM's, hill shade images and velocity maps of the Skelton Glacier. Some areas of the catchment basin are difficult to delineate and can lead to small errors in the estimated location of the ice divides. The mean accumulation error is estimated to be as high as 20%.

The cross-sectional area of the glacier at the flux gate locations is another source of uncertainty. This includes the assumption that the glacier shape is parabolic which can only be confirmed with detailed ice thickness data, but only one line of thickness measurements up the centreline of the glacier is available. The limited data and assumptions that arose with the cross-section calculation caused an estimated mean cross-section area error of 10%.

Lastly, the velocity is also a source of uncertainty, even though it has been processed to a high relative and absolute accuracy. Throughout processing small errors are present which can propagate through to the final displacement map. The final map is then adjusted to a ground truth point taken from an *in-situ* GPS unit. The velocities do not match the GPS ground truth data exactly, which means there are small uncertainties in the velocities due to the variation of results. The mean velocity error is estimated to be approximately 5%.

By using the estimated error percentages for each of these factors, along with estimated mean values for the velocity, cross-section area and accumulation (0.1 km yr^{-1}, 5 km^2 and 0.5 Gt a^{-1} respectively), the mean mass balance error is calculated to be 0.110 Gt a^{-1}, or a relative error of about 22%. This is comparable to the relative measurement errors in Table 4.1. The biggest single source of uncertainty for the final mass balance estimate is the snow accumulation. Assuming no error in area and velocity results in a relative error of about 20%. Assuming no error in accumulation results in a relative error of about 10%.

7 – Summary and Conclusion

This research has looked into the ice dynamics of the Skelton Glacier, which is one of the smaller outlet glaciers draining ice from the TAM into the Ross Ice Shelf. ERS SAR data from 1996 has been used with newer auxiliary datasets to create a high resolution ice velocity field of the glacier using interferometric processing. This high resolution velocity field has then been used with ice thickness data to determine the mass flux at various flux gates on the glacier. These mass flux estimates and additional accumulation datasets form the inputs and outputs of the budget method, which is one of the satellite remote sensing methods used to estimate the mass balance. Finding the mass balance of the Skelton Glacier fills in one of the gaps of data needed to determine the current state of TAM glaciers and the EAIS. The current mass balance estimates of the EAIS contain large uncertainties which make it difficult to precisely estimate if the ice sheet is losing or gaining ice. This makes detailed studies of every outlet glacier and ice stream important, as this will lower uncertainties and allow for more precise estimates of the state of the EAIS.

SAR Interferometry was used in this research to produce an ice velocity field of the Skelton Glacier. This helped prove that ERS data from the 1990's can be successfully re-analysed with new auxiliary data. This was critical for the ERS InSAR data, for which in this area, no differential pairs are available. DInSAR is however, required to apply InSAR techniques over fast moving glaciers. Precise elevation data like TanDEM-X and ICESat data enable the correction of the baseline errors in the ERS data, if large stagnant areas are present in the study area. This offers opportunities for re-analysis of the catchment basins. This will extend high resolution velocity measurements back to the 1990's.

The ice velocity field of the Skelton Glacier that was created from the ERS SAR data gave a short term representation of the ice velocity of the Skelton Glacier but matched the GPS ground measurements and other satellite-based velocity fields mostly within $15ma^{-1}$. The lower part of the glacier matched closely, while the upper region of the glacier tended to have larger errors in terms of velocity magnitude and flow directions. This is due to this region having less surface gradient and lower velocities. The mass flux measurements at the ten flux gates along the glacier mostly followed the pattern of increasing down the glacier, as was the accumulation estimates. The mass balances at the flux gates showed a pattern which was mostly positive on the Northern Branch, while the Southern Branch had a mix of positive and negative mass balances at the different flux gates. The mass flux near the grounding line is 1.2165 Gt a^{-1} which is consistent with flux gates on the floating ice downstream from the grounding line. At this point, the combined mass balance is slightly negative. The second flux gate is thought to be more representative with a positive mass balance of 0.0441 Gt a^{-1} or approximately 4% more accumulating ice than discharge. Error analysis of the propagating errors from the accumulation data, ice thickness estimations and velocity field have an

estimated uncertainty of about 0.110 Gt a^{-1} or a relative mean error of 22%. This deviation was found to be representative for most flux gate measurements. This error is comparable or smaller to other studies in ice sheet mass balance (Shepherd *et al.*, 2012). This study shows that the Skelton Glacier is close to a state of balance, which is in accordance with other smaller catchments in the TAM, but contrary to catchments line Byrd Glacier (Stearns, 2011). Also, the analysis and field data indicate there was no change in ice dynamics over period of detailed satellite observations, or maybe longer.

There is still room for improvement, not only for the Skelton Glacier, but for other smaller outlet glaciers in the TAM and around the EAIS. Errors over small catchment basins can be large and require high quality and coverage of data to achieve confidence in results. For this research, some of the data lacked the quality and quantity required to minimise uncertainties, so future studies of the glacier can achieve more precise results with better data, especially accumulation and ice thickness. The TanDEM-X that was used for this study proved how important a high resolution DEM is for interferometric processing, but as it only covered the centre of the study area, the rest of the ice velocity field used the poorer quality RAMPv2 DEM. If a full coverage of the Skelton Glacier could use a high quality DEM such as the TanDEM-X, the velocity errors would be minimised. Also, thickness data on the glacier is vital for determining the shape when estimating the mass flux through cross-sections. This research was limited to one line of measurements along the centreline of the glacier, which then required broad assumptions to estimate the bedrock shape. If airborne surveys could acquire much more thickness data for the Skelton Glacier, the glacier shape could be determined more accurately. As well as airborne surveys, further ground surveys (especially ones that research basal conditions) could determine flow mechanisms of the glacier ice stream, which will then allow for the resisting shear stress levels to be known and included within the mass flux calculations. The two accumulation datasets gave a good estimate of the accumulation over the catchment area, but were still much poorer resolution than the rest of the data used for the mass balance studies. In the future, especially new accumulation and ice thickness datasets have the potential to further reduce the errors associated with the mass balance estimates.

8 – References

Arthern, R. J., Winebrenner, D. P., & Vaughan, D. G. (2006). Antarctic snow accumulation mapped using polarization of 4.3-cm wavelength microwave emission. *Journal of Geophysical Research: Atmospheres, 111*(D6), D06107. doi: 10.1029/2004jd005667

Bähr, H., & Hanssen, R. F. (2009). *Network Adjustment of Orbit Errors in SAR Interferometry.* Paper presented at the Proc. Fringe 2009 Workshop, Frascati, Italy.

Bamber, J., & Gomez-Dans, J. L. (2005). The accuracy of digital elevation models of the Antarctic continent. *Earth and Planetary Science Letters, 237*(3–4), 516-523. doi: 10.1016/j.epsl.2005.06.008

Bart, P. J., & Anderson, J. B. (2000). Relative temporal stability of the Antarctic ice sheets during the late Neogene based on the minimum frequency of outer shelf grounding events. *Earth and Planetary Science Letters, 182*(3–4), 259-272. doi: http://dx.doi.org/10.1016/S0012-821X(00)00257-0

Bartusch, M., Hajnsek, I., Janoth, J., Marschner, C., Moreira, A., Sparwasser, N., & Zink, M. (2010). TanDEM-X: The Earth in Three Dimensions (S. Blair, P. Clissold & A. Mehta, Trans.). In G. A. Centre (Ed.). Bonn: Deutsches Zentrum Fur Luft- und Raumfahrt e.V. DLR.

Bombrun, L., Gay, M., Trouve, E., Vasile, G., & Mars, J. (2009). DEM Error Retrieval by Analyzing Time Series of Differential Interferograms. *Geoscience and Remote Sensing Letters, IEEE, 6*(4), 830-834. doi: 10.1109/lgrs.2009.2026434

Breckenridge, C. J., Radok, U., Stearns, C. R., & Bromwich, D. H. (1993). Katabatic winds along the Transantarctic Mountains *Antarctic Meteorology and Climatology: Studies Based on Automatic Weather Stations* (Vol. 61, pp. 69-92). Washington, DC: AGU.

Brunt, K. M., Fricker, H. A., Padman, L., & O'Neel, S. (2010). ICESat-Derived Grounding Zone for Antarctic Ice Shelves. Boulder, Colorado, USA: National Snow and Ice Data Center.

Bürgmann, R., Rosen, P. A., & Fielding, E. J. (2000). Synthetic Aperture Radar Interferometry to Measure Earth's Surface Topography and Its Deformation. *Annual Review of Earth and Planetary Sciences, 28*(1), 169-209. doi: doi:10.1146/annurev.earth.28.1.169

Cameron, R. L., & Goldthwait, R. P. (1961). The US-IGY Contribution to Antarctic Glaciology. *Intern. Assoc. Sci. Hydrol. , 55*, 7-13.

Chan, Y. K., & Koo, V. C. (2008). An Introduction to Synthetic Aperture Radar (SAR). *Progress in Electromagnetics Research B, 2*, 27-60.

Chandler, D., Hubbard, B., Hubbard, A., Murray, T., & Rippin, D. (2008). Optimising ice flow law parameters using borehole deformation measurements and numerical modelling. *Geophysical Research Letters, 35*(Article), -. doi: 10.1029/2008gl033801

De Angelis, H., & Skvarca, P. (2003). Glacier Surge After Ice Shelf Collapse. *Science, 299*(5612), 1560-1562. doi: 10.1126/science.1077987

Drosg, M. (2009). Dealing with Uncertainties Retrieved from http://canterbury.eblib.com.au/patron/FullRecord.aspx?p=451190

Fletcher, K., European Space, R., & Technology, C. (2007a). *Insar Principles: Guidelines for Sar Interferometry Processing and Interpretation (Part A)*: ESA Publications Division.

Fletcher, K., European Space, R., & Technology, C. (2007b). *Insar Principles: Guidelines for Sar Interferometry Processing and Interpretation (Part B)*: ESA Publications Division.

Fricker, H. A., Warner, R. C., & Allison, I. (2000). Mass balance of the Lambert GlacierAmery Ice Shelf system, East Antarctica: a comparison of computed balance fluxes and measured fluxes. *Journal of Glaciology, 46*(155), 561-570. doi: 10.3189/172756500781832765

Goldstein, R. M., Engelhardt, H., Kamb, B., & Frolich, R. M. (1993). Satellite Radar Interferometry for Monitoring Ice Sheet Motion: Application to an Antarctic Ice Sheet. *Science, 262*(5139), 1525-1530.

Goldstein, R. M., Engelhardt, H., Kamb, B., & Frolich, R. M. (1993). Satellite radar interferometry for monitoring ice sheet motion: Application to an Antarctic ice stream. *Science, 262*, 1525-1530.

Goldstein, R. M., & Zebker, H. A. (1987). Interferometric radar measurement of ocean surface currents. . *Nature, 328*, 707-709.

Goldstein, R. M., Zebker, H. A., & Werner, C. L. (1988). Satellite radar interferometry: Two-dimensional phase unwrapping. *Radio Science, 23*(4), 713-720. doi: 10.1029/RS023i004p00713

Golledge, N. R., & Levy, R. H. (2011). Geometry and dynamics of an East Antarctic Ice Sheet outlet glacier, under past and present climates. *Journal of Geophysical Research: Earth Surface, 116*(F3), F03025. doi: 10.1029/2011jf002028

Gudmundsson, G. H. (2006). Fortnightly variations in the flow velocity of Rutford Ice Stream, West Antarctica. *Nature, 444*(7122), 1063-1064. doi: doi.org/10.1038/nature05430

Helsen, M. M., van den Broeke, M. R., van de Wal, R. S. W., van de Berg, W. J., van Meijgaard, E., Davis, C. H., Li, Y., & Goodwin, I. (2008). Elevation Changes in Antarctica Mainly Determined by Accumulation Variability. *Science, 320*(5883), 1626-1629. doi: 10.1126/science.1153894

Henry, E., Mayer, C., & Rott, H. (2004). Mapping mining-induced subsidence from space in a hard rock mine: example of SAR interferometry application at Kiruna mine. *CIM Bulletin, 97*(1083).

Holland, D. M., Thomas, R. H., de Young, B., Ribergaard, M. H., & Lyberth, B. (2008). Acceleration of Jakobshavn Isbrae triggered by warm subsurface ocean waters. *Nature Geoscience, 1*(10), 659. doi: doi.org/10.1038/ngeo316

Hooke, R. L. B. (2005). *Principles of Glacier Mechanics*: Cambridge University Press.

Hoonyol, L., & Jian Guo, L. (2001). Analysis of topographic decorrelation in SAR interferometry using ratio coherence imagery. *Geoscience and Remote Sensing, IEEE Transactions on, 39*(2), 223-232. doi: 10.1109/36.905230

Humbert, A., Greve, R., & Hutter, K. (2005). Parameter sensitivity studies for the ice flow of the Ross Ice Shelf, Antarctica. *Journal of Geophysical Research: Earth Surface, 110*(F4), F04022. doi: 10.1029/2004jf000170

IPCC. (2007). Contribution of Working Group I to the Fourth Assessment Report of the Intergovernmental Panel on Climate Change, 2007. In S. Solomon, D. Qin, M. Manning, Z. Chen, M. Marquis, K. B. Averyt, M. Tignor & H. L. Miller (Eds.). Cambridge, United Kingdom and New York, NY, USA.: Cambridge University.

Jackson, C. R., & Apel, J. R. (2004). Synthetic Aperture Radar Marine User's Manual. U.S. Department of Commerce: National Oceanic and Atmospheric Administration.

Jacobs, S. S., Jenkins, A., Giulivi, C. F., & Dutrieux, P. (2011). Stronger ocean circulation and increased melting under Pine Island Glacier ice shelf. *Nature Geoscience, 4*(8), 519-523. doi: doi.org/10.1038/ngeo1188

Joughin, I. R., Kwok, R., & Fahnestock, M. A. (1998). Interferometric estimation of three-dimensional ice-flow using ascending and descending passes. *Geoscience and Remote Sensing, IEEE Transactions on, 36*(1), 25-37. doi: 10.1109/36.655315

Ketelaar, V. B. H. (2009). *Satellite Radar Interferometry* (Vol. 14). New York: Springer.

Krieger, G., Fiedler, H., Hajnsek, I., Eineder, M., Werner, M., & Moreira, A. (2005, 25-29 July 2005). *TanDEM-X: mission concept and performance analysis.* Paper presented at the Geoscience and Remote Sensing Symposium, 2005. IGARSS '05. Proceedings. 2005 IEEE International.

Kwok, R., & Fahnestock, M. A. (1996). Ice sheet motion and topography from radar Interferometry. *IEEE Transactions on Geoscience and Remote Sensing, 34*(1), 189-200.

Lenaerts, J. T. M., van den Broeke, M. R., van de Berg, W. J., van Meijgaard, E., & Kuipers Munneke, P. (2012). A new, high-resolution surface mass balance map of Antarctica (1979–2010) based on regional atmospheric climate modeling. *Geophysical Research Letters, 39*(4), L04501. doi: 10.1029/2011gl050713

Liu, H., Jezek, K. C., Li, B., & Zhao, Z. (2001). Radarsat Antarctic Mapping Project Digital Elevation Model Version 2. Boulder, Colorado USA: National Snow and Ice Data Center.

Lopez-Dekker, P., Prats, P., De Zan, F., Schulze, D., Krieger, G., & Moreira, A. (2011). TanDEM-X First DEM Acquisition: A Crossing Orbit Experiment. *Geoscience and Remote Sensing Letters, IEEE, 8*(5), 943-947. doi: 10.1109/lgrs.2011.2127444

Mansourpour, M., Rajabi, M. A., & Rezaee, Z. (2008). Radiometric and Geometric Correction Methods for Active Radar and SAR Imageries. Tehran, Iran: University of Tehran.

Massonnet, D., Briole, P., & Arnaud, A. (1995). Deflation of Mount Etna monitored by spaceborne radar interferometry. *Nature, 375*, 567-570.

Massonnet, D., & Feigl, K. L. (1998). Radar interferometry and its application to changes in the Earth's surface. *Reviews of Geophysics, 36*(4), 441-500. doi: 10.1029/97rg03139

McCandless, S. W., & Jackson, C. R. (2004). *Chapter 1: Principles of Synthetic Aperture Radar*. Washington DC: U.S. Department of Commerce.

Neckel, N., Drews, R., Rack, W., & Steinhage, D. (2012). Basal melting at the Ekström Ice Shelf, Antarctica, estimated from mass flux divergence. *Annals of Glaciology, 53*(60), 294-302. doi: 10.3189/2012AoG60A167

Oliver, C., & Quegan, S. (1997). *Understanding Synthetic Aperture Radar Images*. Norwood, Ma: ARTECH HOUSE, INC.

Paterson, W. S. B., & Cuffey, K. M. (2010). *The Physics of Glaciers*. Oxford, UK: Elsevier.

Rack, W., & Rott, H. (2004). Pattern of retreat and disintegration of the Larsen B ice shelf, Antarctic Peninsula. [doi:10.3189/172756404781814005]. *Annals of Glaciology, 39*(1), 505-510.

Radzevicius, S. J., & Daniels, J. J. (2000). Ground penetrating radar polarization and scattering from cylinders. *Journal of Applied Geophysics, 45*(2), 111-125. doi: http://dx.doi.org/10.1016/S0926-9851(00)00023-9

Richards, J. A. (2009). *Remote Sensing with Imaging Radar*. New York: Springer.

Richards, M. A. (2005). *Fundamentals of Radar Signal Processing*. New York: McGraw-Hill.

Richards, M. A. (2007). A Beginners Guide to Interferometric SAR Concepts and Signal Processing. *IEEE A&E Systems Magazine, 22*(9).

Riger-Kusk, M. (2011). *Ice dynamics of the Darwin-Hatherton glacial system, Transantarctic Mountains, Antarctica.* Doctor of Philosophy in Geography, University of Canterbury.

Rignot, E. (2002). Mass balance of East Antarctic glaciers and ice shelves from satellite data. *Annals of Glaciology, 34*(1), 217-227. doi: 10.3189/172756402781817419

Rignot, E. (2006). Changes in ice dynamics and mass balance of the Antarctic ice sheet. *Philosophical Transactions of the Royal Society A: Mathematical, Physical and Engineering Sciences, 364*(1844), 1637-1655. doi: 10.1098/rsta.2006.1793

Rignot, E., Bamber, J. L., van den Broeke, M. R., Davis, C. H., Li, Y., van de Berg, W. J., & van Meijgaard, E. (2008). Recent Antarctic ice mass loss from radar interferometry and regional climate modelling. *Nature Geoscience, 1*(2), 106-110. doi: doi.org/10.1038/ngeo102

Rignot, E., Box, J., Burgess, E., & Hanna, E. (2008). Mass balance of the Greenland ice sheet from 1958 to 2007. *Geophysical Research Letters, 35*(20), L20502. doi: 10.1029/2008gl035417

Rignot, E., Echelmeyer, K., & Krabill, W. (2001). Penetration depth of interferometric synthetic-aperture radar signals in snow and ice. *Geophysical Research Letters, 28*(18), 3501-3504. doi: 10.1029/2000gl012484

Rignot, E., Mouginot, J., & Scheuchl, B. (2011). Ice Flow of the Antarctic Ice Sheet. *Science, 333*(6048), 1427-1430. doi: 10.1126/science.1208336

Rignot, E., & Thomas, R. H. (2002). Mass Balance of Polar Ice Sheets. *Science, 297*(5586), 1502-1506. doi: 10.1126/science.1073888

Rosen, P. A., Hensley, S., Zebker, H. A., Webb, F. H., & Fielding, E. J. (1996). Surface deformation and coherence measurements of Kilauea Volcano, Hawaii, from SIR-C radar interferometry. *Journal of Geophysical Research: Planets, 101*(E10), 23109-23125. doi: 10.1029/96je01459

Roth, A., Huber, M., & Kosmann, D. (2004). *Geocoding of TerraSAR-X data.* Paper presented at the Proc. of 20'th International Congress of the ISPRS.

Rotschky, G. (2007). Spatial distribution of snow accumulation and snowpack properties in Dronning Maud Land, Antarctica : observational techniques and methods for surface mass-balance assessments of polar ice sheets *Reports on Polar and Marine Research*. Bremerhaven: Alfred Wegener Institute for Polar and Marine Research.

Rott, H. (2009). Advances in interferometric synthetic aperture radar (InSAR) in earth system science. *Progress in Physical Geography, 33*(6), 769-791. doi: 10.1177/0309133309350263

Sanden, J. J. v. d. (1997). *Radar remote sensing to support tropical forest management*. Georgetown, Guyana: Tropenbos-Guyana Programme.

Sasgen, I., Konrad, H., Ivins, E. R., Broeke, M. R. v. d., Bamber, J. L., Martinec, Z., & Klemann, V. (2012). Antarctic ice-mass balance 2002 to 2011: regional re-analysis of GRACE satellite gravimetry measurements with improved estimate of glacial-isostatic adjustment. *The Cryosphere Discuss, 6*(5), 3703-3732.

Schoof, C. (2007). Ice sheet grounding line dynamics: Steady states, stability, and hysteresis. *Journal of Geophysical Research, 112*, 1 - 19.

Shepherd, A., Ivins, E. R., A, G., Barletta, V. R., Bentley, M. J., Bettadpur, S., Briggs, K. H., Bromwich, D. H., Forsberg, R., Galin, N., Horwath, M., Jacobs, S., Joughin, I., King, M. A., Lenaerts, J. T. M., Li, J., Ligtenberg, S. R. M., Luckman, A., Luthcke, S. B., McMillan, M., Meister, R., Milne, G., Mouginot, J., Muir, A., Nicolas, J. P., Paden, J., Payne, A. J., Pritchard, H., Rignot, E., Rott, H., Sørensen, L. S., Scambos, T. A., Scheuchl, B., Schrama, E. J. O., Smith, B., Sundal, A. V., van Angelen, J. H., van de Berg, W. J., van den Broeke, M. R., Vaughan, D. G., Velicogna, I., Wahr, J., Whitehouse, P. L., Wingham, D. J., Yi, D., Young, D., & Zwally, H. J. (2012). A Reconciled Estimate of Ice-Sheet Mass Balance. *Science, 338*(6111), 1183-1189. doi: 10.1126/science.1228102

Stearns, L. A. (2011). Dynamics and mass balance of four large East Antarctic outlet glaciers. *Annals of Glaciology, 52*(59), 116-126. doi: 10.3189/172756411799096187

van 't Klooster, K. (2011, 12-16 Sept. 2011). *ERS-1, European remote-sensing satellite was launched 20 years ago.* Paper presented at the Microwave and Telecommunication Technology (CriMiCo), 2011 21th International Crimean Conference.

Vaughan, D. G. (1993). Relating the occurrence of crevasses to surface strain rates. *Journal of Glaciology, 39*(132), 255-256.

Velicogna, I., & Wahr, J. (2006). Measurements of Time-Variable Gravity Show Mass Loss in Antarctica. *Science, 311*(5768), 1754-1756. doi: 10.1126/science.1123785

Wegmüller, U., Werner, C. L., Strozzi, T., & Wiesmann, A. (2002). Phase Unwrapping with GAMMA ISP Technical Report, 13-May-2002. Bern, Switzerland: Gamma Remote Sensing AG.

Wilson, C. R., & Crary, A. P. (1961). Ice Movement Studies on the Skelton Glacier. *Journal of Glaciology, 29*, 873-878.

Wright, T. J. (2002). Remote monitoring of the earthquake cycle using satellite radar interferometry. *Philosophical Transactions of the Royal Society A, 360*, 2873-2888.

Wright, T. J. (2002). Remote monitoring of the earthquake cycle using satellite radar interferometry. *Philosophical Transactions of the Royal Society of London. Series A: Mathematical, Physical and Engineering Sciences, 360*(1801), 2873-2888. doi: 10.1098/rsta.2002.1094

Zebker, H. A., Werner, C. L., Rosen, P. A., & Hensley, S. (1994). Accuracy of topographic maps derived from ERS-1 interferometric radar. *Geoscience and Remote Sensing, IEEE Transactions on, 32*(4), 823-836. doi: 10.1109/36.298010

Zhong, L., Eric, F., Patrick, M. R., & Trautwein, C. M. (2003). Estimating lava volume by precision combination of multiple baseline spaceborne and airborne interferometric synthetic aperture radar: the 1997 eruption of Okmok volcano, Alaska. *Geoscience and Remote Sensing, IEEE Transactions on, 41*(6), 1428-1436. doi: 10.1109/tgrs.2003.811553

Zink, M., Krieger, G., Fiedler, H., Hajnsek, I., & Moreira, A. (2008). The TanDEM-X Mission Concept. *Synthetic Aperture Radar (EUSAR), 2008 7th European Conference on*, 1-4.

Zumberge, J. F., Heflin, M. B., Jefferson, D. C., Watkins, M. M., & Webb, F. H. (1997). Precise point positioning for the efficient and robust analysis of GPS data from large networks. *Journal of Geophysical Research: Solid Earth, 102*(B3), 5005-5017. doi: 10.1029/96jb03860

Appendix

The following are three examples of parameter files that were used in processing, including a SLC parameter file for an acquired SLC image, an Interferogram and Image Offset Parameter File containing co-registration information and processing parameters, and a DEM parameter file containing information about the DEM and projection. These examples are from Track 455.

Gamma Interferometric SAR Processor (ISP) - Image Parameter File

```
title:     SAR
sensor:    ERS1
date:      1996  3 21
start_time:              61043.445410   s
center_time:             61051.797219   s
end_time:                61060.149028   s
azimuth_line_time:     6.0245322e-04  s
line_header_size:                0
range_samples:                4912
azimuth_lines:               27727
range_looks:                     1
azimuth_looks:                   1
image_format:               SCOMPLEX
image_geometry:             SLANT_RANGE
range_scale_factor:     1.0000000e+00
azimuth_scale_factor:   1.0000000e+00
center_latitude:         -78.4879270   degrees
center_longitude:        161.0717830   degrees
heading:                 -78.1598340   degrees
range_pixel_spacing:        7.904890   m
azimuth_pixel_spacing:      4.014240   m
near_range_slc:           856972.1019   m
center_range_slc:         876382.5593   m
far_range_slc:            895793.0167   m
first_slant_range_polynomial:        0.00000      0.00000  0.00000e+00
0.00000e+00  0.00000e+00  0.00000e+00  s m 1 m^-1 m^-2 m^-3
center_slant_range_polynomial:       0.00000      0.00000  0.00000e+00
0.00000e+00  0.00000e+00  0.00000e+00  s m 1 m^-1 m^-2 m^-3
last_slant_range_polynomial:         0.00000      0.00000  0.00000e+00
0.00000e+00  0.00000e+00  0.00000e+00  s m 1 m^-1 m^-2 m^-3
incidence_angle:            23.3970   degrees
azimuth_deskew:          ON
azimuth_angle:              90.0000   degrees
radar_frequency:        5.3000000e+09   Hz
adc_sampling_rate:      1.8962468e+07   Hz
chirp_bandwidth:        1.5550000e+07   Hz
prf:                     1659.879902   Hz
azimuth_proc_bandwidth:   1327.90392   Hz
doppler_polynomial:       -278.75800  0.00000e+00  0.00000e+00  0.00000e+00
Hz     Hz/m     Hz/m^2     Hz/m^3
doppler_poly_dot:        0.00000e+00  0.00000e+00  0.00000e+00  0.00000e+00
Hz/s   Hz/s/m   Hz/s/m^2   Hz/s/m^3
doppler_poly_ddot:       0.00000e+00  0.00000e+00  0.00000e+00  0.00000e+00
Hz/s^2 Hz/s^2/m Hz/s^2/m^2 Hz/s^2/m^3
receiver_gain:              -15.0000   dB
calibration_gain:            49.7000   dB
```

```
sar_to_earth_center:             7170383.7785   m
earth_radius_below_sensor:       6357610.9592   m
earth_semi_major_axis:           6378137.0000   m
earth_semi_minor_axis:           6356752.3141   m
number_of_state_vectors:                    7
time_of_first_state_vector:      61013.000000   s
state_vector_interval:              10.000000   s
state_vector_position_1:  -1057947.1526     136102.1080   -7090657.0354   m
m   m
state_vector_velocity_1:      878.48510      7471.68330        12.15600
m/s m/s m/s
state_vector_position_2:  -1049051.3515     210803.8790   -7090153.1026   m
m   m
state_vector_velocity_2:      900.65820      7468.52940        88.62960
m/s m/s m/s
state_vector_position_3:  -1039934.3234     285469.9545   -7088884.4738   m
m   m
state_vector_velocity_3:      922.72970      7464.54380       165.09370
m/s m/s m/s
state_vector_position_4:  -1030597.1010     360092.0280   -7086851.2842   m
m   m
state_vector_velocity_4:      944.69610      7459.72700       241.54020
m/s m/s m/s
state_vector_position_5:  -1021040.7300     434661.9618   -7084053.7443   m
m   m
state_vector_velocity_5:      966.55390      7454.07970       317.96120
m/s m/s m/s
state_vector_position_6:  -1011266.3643     509171.0990   -7080492.1657   m
m   m
state_vector_velocity_6:      988.29940      7447.60280       394.34810
m/s m/s m/s
state_vector_position_7:  -1001275.1214     583611.3084   -7076166.9216   m
m   m
state_vector_velocity_7:     1009.92910      7440.29700       470.69300
m/s m/s m/s
```

Interferogram and Image Offset Parameter File

```
title:     INTERF_SLC_1
initial_range_offset:                  -4
initial_azimuth_offset:             -5338
slc1_starting_range_pixel:              0
number_of_slc_range_pixels:          4912
offset_estimation_starting_range:      48
offset_estimation_ending_range:      4864
offset_estimation_range_samples:      100
offset_estimation_range_spacing:       48
offset_estimation_starting_azimuth:    48
offset_estimation_ending_azimuth:   27679
offset_estimation_azimuth_samples:    300
offset_estimation_azimuth_spacing:     92
offset_estimation_window_width:        64
offset_estimation_window_height:       64
offset_estimation_threshhold:        7.00
range_offset_polynomial:       -3.75685   1.0157e-04  -1.2191e-05  -
1.1137e-09   0.0000e+00   0.0000e+00
```

```
azimuth_offset_polynomial:   -5338.85264   2.6062e-04   5.0918e-07  -
1.5548e-09   0.0000e+00   0.0000e+00
slc1_starting_azimuth_line:              0
interferogram_azimuth_lines:          5545
interferogram_width:                  4912
first_nonzero_range_pixel:              15
number_of_nonzero_range_pixels:       4885
interferogram_range_looks:               1
interferogram_azimuth_looks:             5
interferogram_range_pixel_spacing:    7.904890   m
interferogram_azimuth_pixel_spacing:  20.071200   m
resampled_range_pixel_spacing:        0.000000   m
resampled_azimuth_pixel_spacing:      0.000000   m
resampled_starting_ground_range:      0.00000   m
resampled_pixels_per_line:            0
resampled_number_of_lines:            0
```

Gamma DIFF&GEO DEM/MAP parameter file

```
title: ramp200dem_wgs84_v2
DEM_projection:     PS
data_format:        REAL*4
DEM_hgt_offset:          0.00000
DEM_scale:               1.00000
width:                2504
nlines:               2292
corner_north: -1130000.000   m
corner_east:    344400.000   m
post_north:    -50.0000000   m
post_east:      50.0000000   m
PS_secant_lat:          -71.000000   decimal degrees
PS_central_meridian:      0.000000   decimal degrees

ellipsoid_name: WGS 84
ellipsoid_ra:        6378137.000   m
ellipsoid_reciprocal_flattening:  298.2572236

datum_name: WGS 1984
datum_shift_dx:              0.000   m
datum_shift_dy:              0.000   m
datum_shift_dz:              0.000   m
datum_scale_m:         0.00000e+00
datum_rotation_alpha:  0.00000e+00   arc-sec
datum_rotation_beta:   0.00000e+00   arc-sec
datum_rotation_gamma:  0.00000e+00   arc-sec
datum_country_list Global Definition, WGS84, World
```

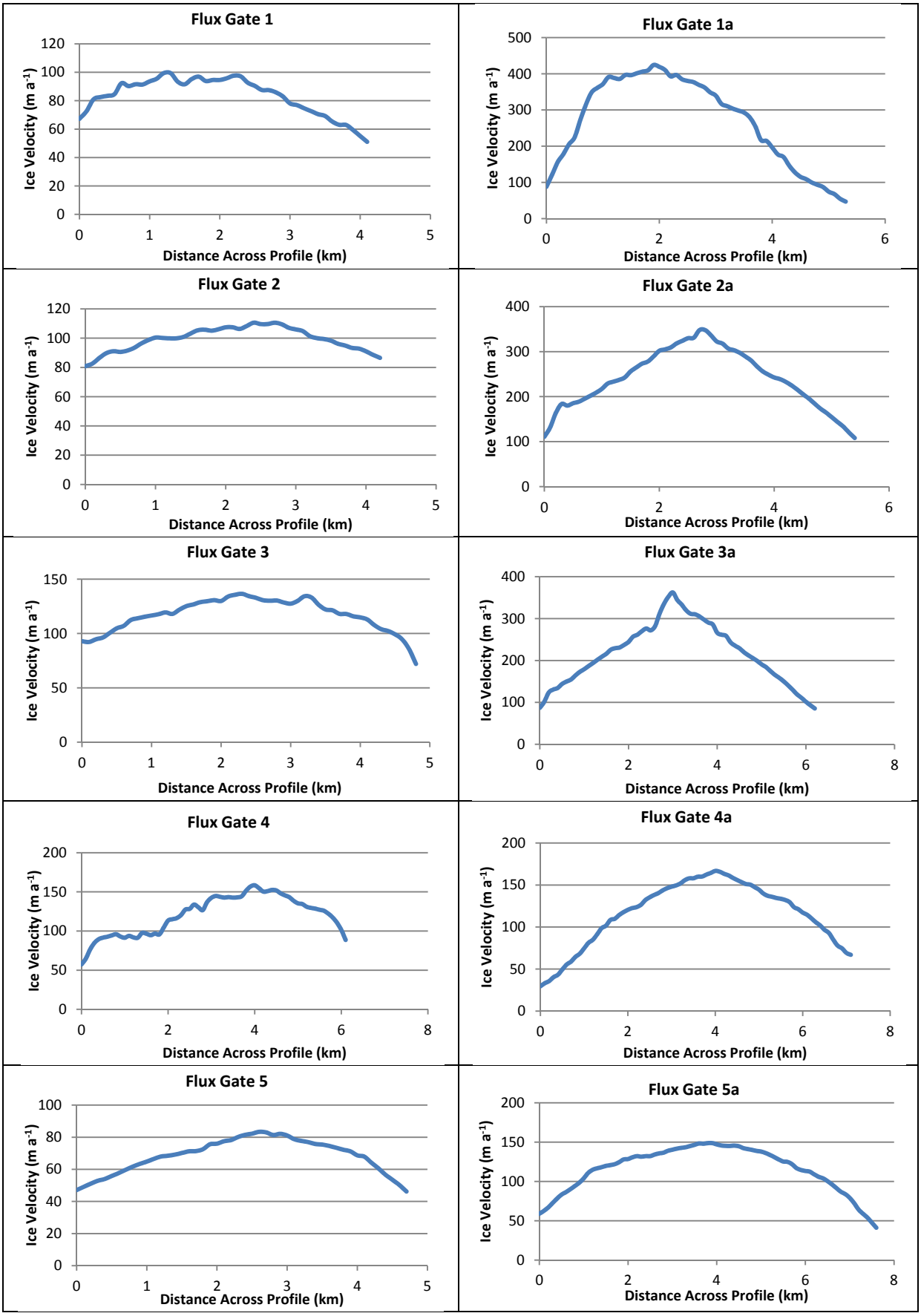

Figure A1: Velocity profiles of the ten flux gates situated on the Skelton Glacier

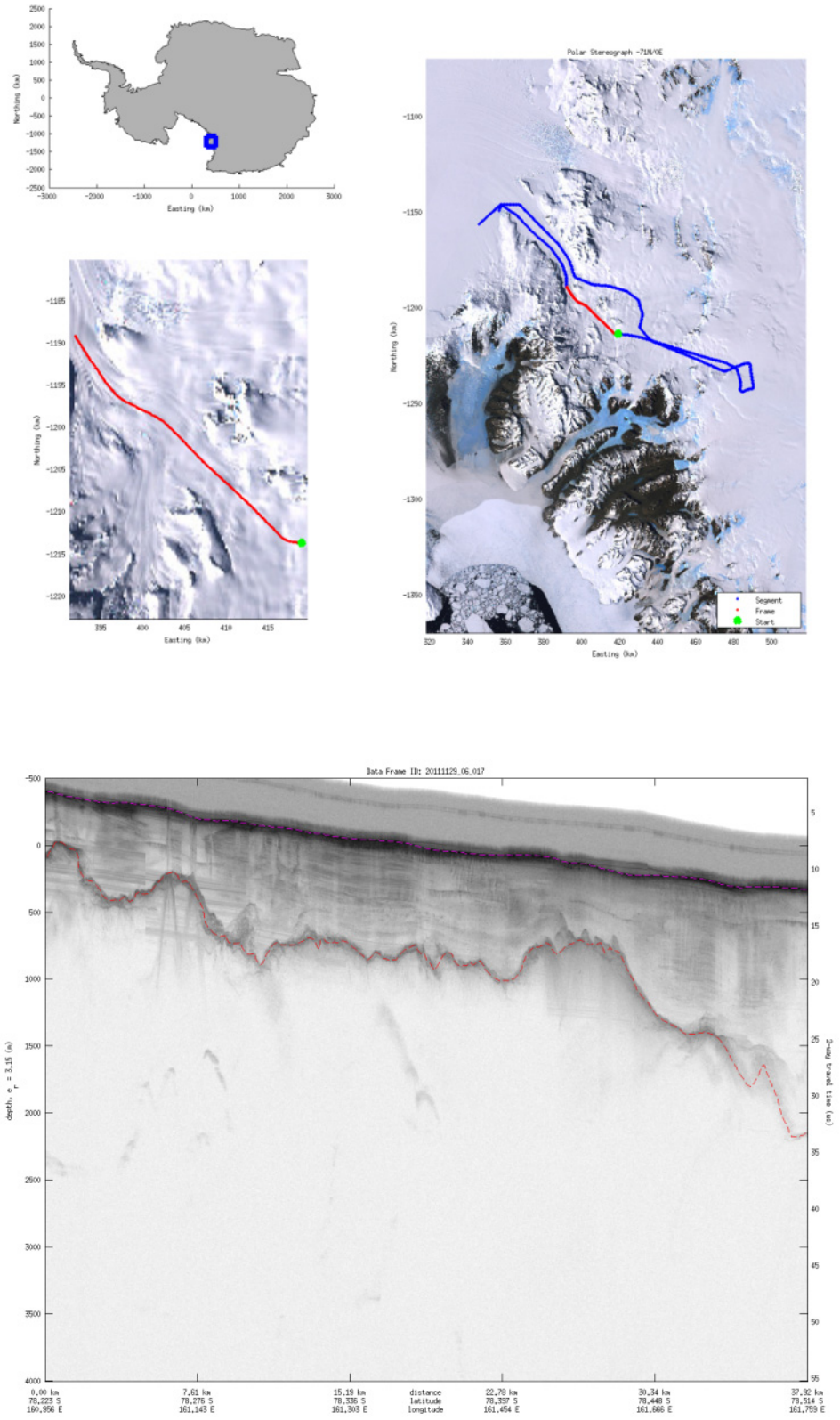

Figure A2: Thickness Profiles from CReSIS above the estimated grounding line area

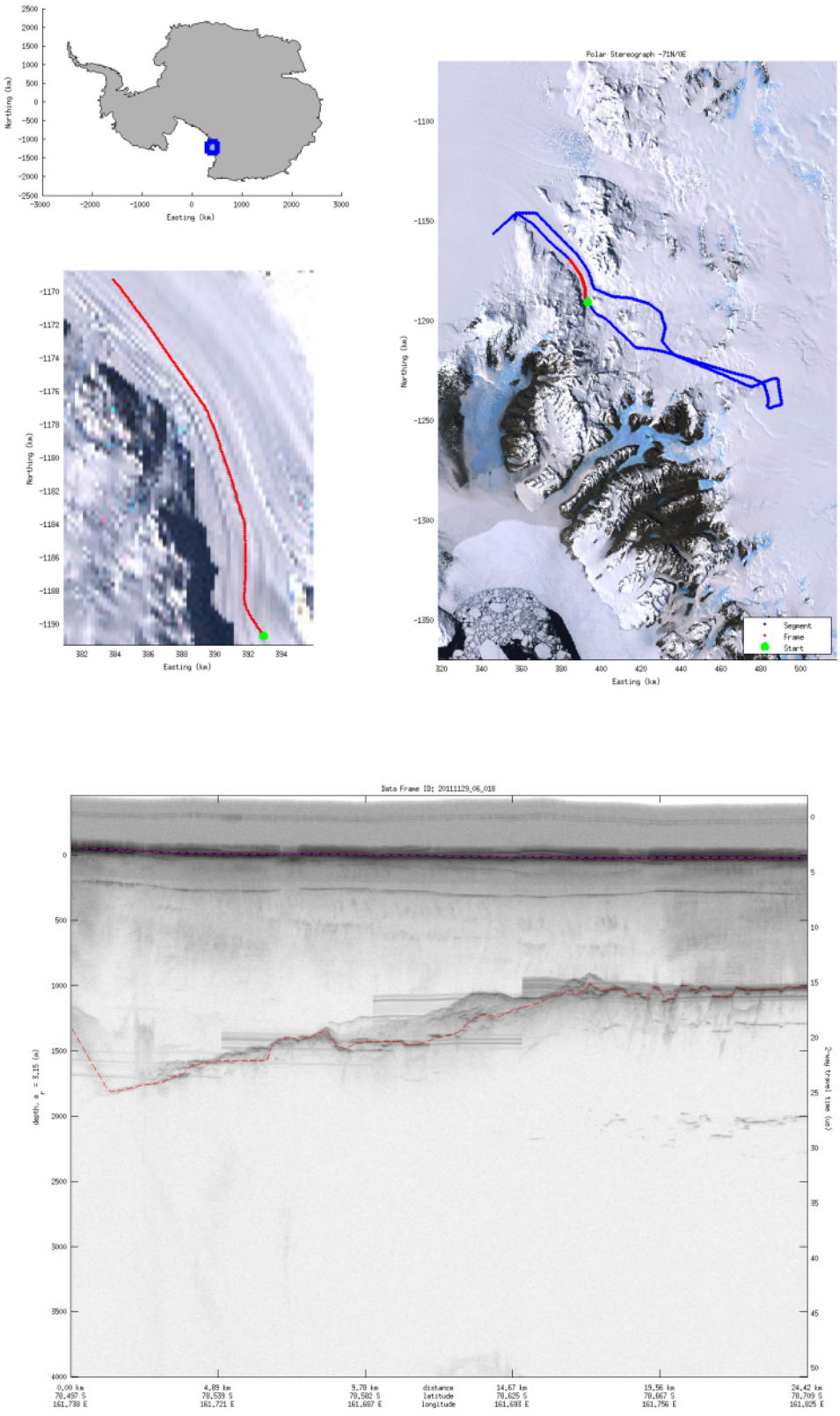

Figure A3: Thickness Profiles from CReSIS below the estimated grounding line which is near the point where ice is deepest.

Acknowledgements

I would like to thank everyone who has supported me during my master's thesis. None more so than my supervisors Wolfgang Rack, Heather Purdie and Oliver Marsh, who have helped guide me though each step taken to complete the research project. I could not have done it without the guidance from these three people. The regular meetings and feedback was very much appreciated.

I would also like to thank Gateway Antarctica and all the people in it for making me feel welcome! Also the fun times we had in the department and out around Christchurch.

A special thanks also goes to the MGIS coordinators who have established a wonderful course at the University of Canterbury which I was lucky to be part of. I have learned valuable skills to take with me into the future.

Lastly, I'd like to thank Christchurch for staying (relatively) stable during the duration of my thesis!!